https://doi.org/10.15388/vu.thesis.767
https://orcid.org/0009-0007-3449-7309

CENTER FOR PHYSICAL SCIENCES AND TECHNOLOGY
VILNIUS UNIVERSITY

Vytautas Žalandauskas

Application of the SCAN Density Functional for Modeling Electronic Excitations and Electron–Phonon Interactions of Point Defects in Semiconductors

DOCTORAL DISSERTATION

Natural Sciences,
Physics (N 002)

VILNIUS 2025

This dissertation was written between 2020 and 2024 at Center for Physical Sciences and Technology (FTMC).

Academic Supervisor:
Dr. Lukas Razinkovas (Center for Physical Sciences and Technology, Natural Sciences, Physics – N 002)

Former Academic Supervisor (in memoriam):
Dr. Audrius Alkauskas (supervised from 2020 to 2023)

Dissertation Defense Panel:

Chairman – Dr. Linas Vilčiauskas (Center for Physical Sciences and Technology, Natural Sciences, Chemistry – N 003)

Members:
Dr. Jevgenij Chmeliov (Vilnius University, Natural Sciences, Physics – N 002)
Dr. Rokas Kondrotas (Center for Physical Sciences and Technology, Natural Sciences, Physics – N 002)
Dr. Vytas Karpus (Center for Physical Sciences and Technology, Natural Sciences, Physics – N 002)
Dr. Christopher Linderälv (Chalmers University of Technology, Sweden, Natural Sciences, Physics – N 002)

The dissertation shall be defended at a public meeting of the Dissertation Defense Panel at 14:00 on 19 June 2025 in Room D401 of the Center for Physical Sciences and Technology.
Address: Saulėtekio av. 3, FTMC, Room D401, Vilnius, Lithuania.
Tel. +370 5 264 8884; email: office@ftmc.lt.

The text of this dissertation can be accessed at the Vilnius University Library, as well as on the website of Vilnius University: www.vu.lt/naujienos/ivykiu-kalendorius.

https://doi.org/10.15388/vu.thesis.767
https://orcid.org/0009-0007-3449-7309

FIZINIŲ IR TECHNOLOGIJOS MOKSLŲ CENTRAS
VILNIAUS UNIVERSITETAS

Vytautas Žalandauskas

SCAN tankio funkcionalo taikymas giliųjų taškinių defektų elektroninių sužadinimų ir elektron–fononinės sąveikos modeliavimui

DAKTARO DISERTACIJA

Gamtos mokslai,
Fizika (N 002)

VILNIUS 2025

Disertacija rengta 2020–2024 metais Fizinių ir technologijos mokslų centre (FTMC).

Mokslinis vadovas:
dr. Lukas Razinkovas (Fizinių ir technologijos mokslų centras, gamtos mokslai, fizika – N 002)

Buvęs mokslinis vadovas (in memoriam):
dr. Audrius Alkauskas (vadovavo nuo 2020 iki 2023)

Gynimo taryba:

Pirmininkas – dr. Linas Vilčiauskas (Fizinių ir technologijos mokslų centras, gamtos mokslai, chemija – N 003)

Nariai:
dr. Jevgenij Chmeliov (Vilniaus universitetas, gamtos mokslai, fizika – N 002)
dr. Rokas Kondrotas (Fizinių ir technologijos mokslų centras, gamtos mokslai, fizika – N 002)
dr. Vytas Karpus (Fizinių ir technologijos mokslų centras, gamtos mokslai, fizika – N 002)
dr. Christopher Linderälv (Čalmerso universitetas, Švedija, gamtos mokslai, fizika – N 002)

Disertacija ginama viešame Gynimo tarybos posėdyje 2025 m. birželio mėn. 19 d. 14:00 val. Fizinių ir technologijos mokslų centro D401 auditorijoje. Adresas: Saulėtekio al. 3, NFTMC, D401 aud., Vilnius, Lietuva.
Tel. +370 5 264 8884; el. paštas: office@ftmc.lt.

Disertaciją galima peržiūrėti Vilniaus universiteto bibliotekoje ir VU interneto svetainėje adresu: www.vu.lt/naujienos/ivykiu-kalendorius.

Contents

Contents 5

Acknowledgements 8

List of abbreviations 9

1 **Introduction** 10
- 1.1 Goals of the thesis . . . 12
- 1.2 Tasks of the thesis . . . 12
- 1.3 Statements presented for the defense . . . 12
- 1.4 Authors contribution and presentation of the results . . . 13

2 **Theoretical background** 15
- 2.1 Many-particle Schrödinger equation . . . 15
  - 2.1.1 Adiabatic approximation . . . 16
- 2.2 Density functional theory . . . 18
  - 2.2.1 The Hohenberg–Kohn theorems . . . 19
  - 2.2.2 Kohn–Sham formalism . . . 21
  - 2.2.3 Exchange–correlation functionals . . . 23
  - 2.2.4 DFT implementation . . . 27
- 2.3 Vibrational structure . . . 30
  - 2.3.1 Harmonic approximation . . . 30
  - 2.3.2 Crystal vibrations . . . 33
  - 2.3.3 Defect-related vibrations . . . 34
- 2.4 Jahn–Teller effect . . . 35
  - 2.4.1 $E \otimes (e \oplus e \oplus \cdots)$ Jahn–Teller Hamiltonian . . . 36
  - 2.4.2 Practical ab initio approach for solving the Jahn–Teller problem . . . 38
- 2.5 Vibrational broadening of optical spectra . . . 43
  - 2.5.1 Optical lineshapes for non-degenerate states . . . 43
  - 2.5.2 Optical lineshapes for A to E transitions . . . 45
- 2.6 Embedding methodology . . . 46

3 **Benchmarking of SCAN density functional for bulk properties and thermodynamic and electronic properties of point defects** 49

3.1 Introduction 49
3.2 Methodology 50
    3.2.1 Computational details 50
    3.2.2 Defect formation energies 51
    3.2.3 Zero-phonon line energy 52
    3.2.4 Zero-field splitting 54
    3.2.5 Vertical excitation energies 54
3.3 Results and discussion 55
    3.3.1 Bulk lattice parameters 55
    3.3.2 Bulk electronic structure 58
    3.3.3 Bulk phonons of diamond 59
    3.3.4 Defect geometries 60
    3.3.5 Electronic structure of defects 61
    3.3.6 Defect formation energies 65
    3.3.7 Charge-state transition levels 67
    3.3.8 Zero-phonon line energies 68
    3.3.9 Vertical excitation energies 70
    3.3.10 Zero-field splitting 72
3.4 Summary and conclusions 73

4 Electron–phonon coupling modelling 75
4.1 Introduction 75
4.2 Methodology 76
    4.2.1 Computational details 76
    4.2.2 Phonon calculations 76
    4.2.3 Spacial localization of phonon modes 77
    4.2.4 Optical lineshapes 78
4.3 Results and discussion 79
    4.3.1 NV^- center in diamond 79
    4.3.2 Neutral divacancies in 4H-SiC 88
    4.3.3 C-center in silicon 94
4.4 Summary and conclusions 98

5 Optical lineshape modeling in Jahn–Teller systems: NiV^- center in diamond and divacancies in 4H-SiC 101
5.1 Introduction 101
5.2 Methodology 102
    5.2.1 Computational details 102
    5.2.2 Calculation of adiabatic potential energy surfaces . 102

5.3 Results and discussion 104
5.3.1 Adiabatic potential energy surface 104
5.3.2 NiV^{-} center in diamond 106
5.3.3 Neutral axial divacancies in 4H-SiC 112
5.4 Summary and conclusions 116

Bibliography 118

Santrauka 132
1 Įžanga 132
1.1 Tyrimo tikslas 133
1.2 Tyrimo uždaviniai 133
1.3 Ginamieji teiginiai 134
1.4 Autoriaus indėlis ir rezultatų pristatymas mokslinei visuomenei 134
2 Disertacijos sandara 136
2.1 Teorijos ir metodologijos apžvalga 137
2.2 Idealaus kristalo savybių skaičiavimai 140
2.3 Defektų elektroninių sužadinimų skaičiavimai 142
2.4 Elektron–fononinės sąveikos modeliavimas 142
2.5 Jahn–Teller efekto tyrimas 146

Curriculum vitae 148

Acknowledgements

First, I would like to express my deepest gratitude to our late supervisor, dr. Audrius Alkauskas, without whom my scientific journey wouldn't even have started. We all deeply miss you.

I want to thank my supervisor, dr. Lukas Razinkovas, who took up this role and believed in me, Rokas Silkinis, dr. Marek Maciaszek, and the future of our still young Puntukas group, which one day can grow to match the grandeur of its name.

I would like to extend my sincere gratitude to dr. Marianne Etzelmüller Bathen, dr. Lasse Vines and dr. Christopher Linderälv for the insightful discussions and support during challenging times. The meetings made every Friday a blast.

Finally, I want to thank my family for believing in me, and especially Emilija, who was always there with her utmost support and encouragement, words can't express how much this meant to me.

List of abbreviations

APES	adiabatic potential energy surface
CBM	conduction-band minimum
CDFT	constrained density functional theory
DFT	density functional theory
DJT	dynamic Jahn–Teller
DWF	Debye–Waller factor
GGA	generalized gradient approximation
HF	Hartree–Fock
HK	Hohenberg–Kohn
HR	Huang–Rhys
HRF	Huang–Rhys factors
HSE	screened hybrid functional of Heyd, Scuseria and Ernzerhof
JT	Jahn–Teller
KS	Kohn–Sham
LDA	local density approximation
PAW	projector augmented wave method
PBE	generalized gradient approximation of Perdew, Burke and Ernzerhof
PJT	pseudo Jahn–Teller
PL	photoluminescence
PLE	photoluminescence excitation spectroscopy
RT	room-temperature
ΔSCF	delta self-consistent field approximation
SPE(s)	single-photon emitter(s)
QT	quantum technologies
VASP	Vienna ab initio simulation package
VBM	valence-band maximum
ZPL	zero phonon line

Chapter 1

Introduction

The advent of quantum technologies has opened new avenues in quantum computing, quantum communication, and quantum sensing [1–10]. A key requirement for these applications is the ability to generate, manipulate, and read out quantum states with high fidelity. Solid-state platforms, particularly semiconductors, provide a scalable and robust environment for implementing quantum systems, with point defects emerging as promising candidates for quantum bits (qubits) and single-photon emitters (SPEs) [11].

Point defects are atomic-scale imperfections in a crystal lattice that introduce localized electronic states within the band gap. While historically considered detrimental to semiconductor performance, certain deep-level defects (often referred to as color centers) exhibit stable optical and spin properties suitable for quantum technological applications [11]. The nitrogen-vacancy (NV) center in diamond, for example, has demonstrated coherence times exceeding milliseconds even at room temperature, making it a leading candidate for quantum sensing and quantum communication [12–15]. Similarly, defects in silicon carbide and silicon operate in the near-infrared range, facilitating integration with fiber-optic networks [16–27].

Given the vast configurational space of possible defect systems, identifying and optimizing defects for quantum technologies necessitates a theoretical framework capable of accurately predicting their electronic and optical properties. First-principles simulations, particularly those based on density functional theory (DFT), have proven to be indispensable tools for this task. DFT has become the dominant method for investigating the electronic and atomic structure of solids, including defect systems. While DFT is, in principle, exact within the Kohn–Sham formalism [28], practical implementations rely on approximations to the exchange-correlation functional, which governs electron interactions. The most commonly used functionals for solid-state systems include generalized-gradient approximation (GGA) functionals, such as the Perdew-Burke-Ernzerhof (PBE) functional [29], and hybrid functionals, such as the Heyd-Scuseria-Ernzerhof (HSE) functional [30]. Each class of functionals presents trade-offs. GGA functionals, despite their computational efficiency, systematically underestimate semiconductor band gaps [31]. Hybrid functionals improve band-gap predictions but come at a significantly higher computational cost [32]. Moreover, high-throughput defect discovery and modeling of electron–phonon interactions require a balance between accuracy and computational efficiency [33, 34].

A promising alternative to both GGA and hybrid functionals is the Strongly Constrained and Appropriately Normed (SCAN) functional, a meta-GGA class functional introduced in 2015 [35]. Unlike traditional GGA functionals, SCAN incorporates additional information about the kinetic energy density, significantly improving its treatment of exchange and correlation effects. It has been shown to yield more accurate lattice parameters, cohesive energies, and band gaps in semiconductors compared to conventional GGA functionals [36, 37].

The SCAN functional presents distinct advantages for modeling point defects in solids. These systems are typically examined using the supercell approach, which demands computational efficiency due to the large number of atoms involved [38]. SCAN enhances the description of electronic localization and defect states within the band gap while avoiding the high computational expense of hybrid functionals. Although SCAN has been widely applied to bulk materials [39], its use in defect studies remains relatively unexplored [40–43]. Further studies are required to systematically evaluate its accuracy in modeling excited states and electron–phonon interactions across a broader range of defect systems.

The focus of this thesis is to benchmark the SCAN functional and its variants, rSCAN [44] and r^{2}SCAN [45], against GGA and hybrid functionals to evaluate their accuracy and computational efficiency in modeling the electronic and vibrational properties of color centers. Specifically, we aim to demonstrate that the SCAN family can reliably predict optical excitation energies, luminescence, and absorption lineshapes for key semiconductor defects in materials such as diamond, silicon, and silicon carbide.

Beyond assessing the performance of SCAN, this research seeks to enhance the theoretical framework for describing the optical and vibronic behavior of point defects. A more accurate modeling of electron–phonon interactions and the influence of lattice vibrations will provide better understanding of the fundamental properties of defects and their suitability for quantum technology applications. By conducting comprehensive computational analyses and rigorous benchmarking, this study aims to establish SCAN functional as a practical and reliable tool for defect modeling, enabling accurate, cost-effective investigations that allow for extensive screening of potential quantum defects.

1.1. Goals of the thesis

The main goal of this thesis is to benchmark the SCAN and its family of density functionals for point defects in semiconductors by modeling their electronic and vibrational properties.

1.2. Tasks of the thesis

In order to achieve the goal of this thesis, the following tasks were set:

1. Using the SCAN family of functionals calculate optical excitation energies for various point defects in diamond, silicon, and 4H-SiC.

2. Model theoretical luminescence and absorption lineshapes of various point defects in diamond, silicon, and 4H-SiC using the SCAN family of functionals.

3. Compare the results calculated using the SCAN family of functionals with results obtained using standard GGA and hybrid functionals and experimental results.

1.3. Statements presented for the defense

1. The SCAN family of functionals provides accuracy comparable to or better than the more computationally expensive hybrid HSE06 functional for optical excitation energies for defects in diamond and 4H silicon carbide.

2. Regarding electron–phonon coupling during optical transitions, our findings show that SCAN family of functionals yields optical lineshapes that are in great agreement with the experiments while being computationally cost-effective.

3. Employing a novel multi-mode Jahn–Teller computational methodology together with the r^2SCAN functional, we accurately captured the optical features arising from Jahn–Teller interactions in the photoluminescence spectra of split nickel-vacancy center in diamond, thereby demonstrating the functional's performance in determining vibronic-coupling constants.

1.4. Authors contribution and presentation of the results

During the doctoral years the author contributed to five scientific papers:

(T1) Marek Maciaszek, Vytautas Žalandauskas, Rokas Silkinis, Audrius Alkauskas, and Lukas Razinkovas, *The application of the SCAN density functional to color centers in diamond*, J. Chem. Phys. **159**, 084708 (2023).

(T2) Rokas Silkinis, Vytautas Žalandauskas, Gergő Thiering, Adam Gali, Chris G. Van de Walle , Audrius Alkauskas, Lukas Razinkovas, *Optical lineshapes for orbital singlet to doublet transitions in a dynamical Jahn-Teller system: the NiV$^-$ center in diamond*, Phys. Rev. B **110**, 075303 (2024).

(T3) Rokas Silkinis, Marek Maciaszek, Vytautas Žalandauskas, Marianne Etzelmüller Bathen, Audrius Alkauskas, Lukas Razinkovas, *Optical lineshapes of the C center in silicon from ab initio calculations: Interplay of localized modes and bulk phonons*, Phys. Rev. B **111**, 125136 (2025).

(T4) Vytautas Žalandauskas, Rokas Silkinis, Lasse Vines, Lukas Razinkovas, and Marianne Etzelmüller Bathen, *Theory of the divacancy in 4H-SiC: Impact of Jahn–Teller effect on optical properties*, npj Computational Materials, accepted (2025).

(T5) Meysam Mohseni, Lukas Razinkovas, Vytautas Žalandauskas, Gergő Thiering, Adam Gali, *Magneto-optical properties of*

Group-IV–vacancy centers in diamond upon hydrostatic pressure, https://arxiv.org/abs/2408.10407 (2024).

The author of this thesis is the main contributor to papers 1 and 4. The results of the thesis were presented at the following conferences:

I. V. Žalandauskas, M. Maciaszek, L. Razinkovas, A. Alkauskas, *The application of the SCAN density functional to colour centres in diamond*, Open Readings 2022, 2022-03-15, Vilnius, Lithuania. Oral presentation.

II. V. Žalandauskas, M. Maciaszek, L. Razinkovas, R. Silkinis, A. Alkauskas, *The application of the SCAN density functional to colour centres in diamond*, DSQT2022, 2022-06-15, Stokholm, Sweden. Poster presentation.

III. V. Žalandauskas, M. Maciaszek, L. Razinkovas, R. Silkinis, A. Alkauskas, *The application of the SCAN density functional to colour centres in diamond*, 24-th International Conference–School ADVANCED MATERIALS AND TECHNOLOGIES, 2022-08-24, Palanga, Lithuania. Poster presentation.

IV. V. Žalandauskas, M. E. Bathen, L. Razinkovas, *Ab Initio Investigation of Vibrational Properties of Divacancy Defects in Silicon Carbide*, Humboldt Kolleg on Synthetic Quantum Matter, 2023-07-03, Vilnius, Lithuania. Poster presentation.

V. V. Žalandauskas, L. Razinkovas, M. E. Bathen, *Ab initio study of vibrational properties of divacancy defects in 4H-SiC*, The 32nd International Conference on Defects in Semiconductors, 2023-09-12, Rehoboth Beach, Delaware, USA. Poster presentation.

VI. V. Žalandauskas, R. Silkinis, L. Vines, L. Razinkovas, M. E. Bathen, *Ab initio study of vibrational properties of divacancy defects in 4H-SiC*, Open Readings 2024, 2024-04-23, Vilnius, Lithuania. Poster presentation.

VII. V. Žalandauskas, R. Silkinis, L. Vines, L. Razinkovas, M. E. Bathen, *Impact of the Jahn-Teller effect on optical properties of divacancies in 4H-SiC*, DSQT2024, 2024-06-11, Budapest, Hungary. Poster presentation.

Chapter 2

Theoretical background

2.1. Many-particle Schrödinger equation

The fundamental behavior of matter, particularly in the context of defects in solids, is governed by the principles of quantum mechanics. At the microscopic level, a defect system consists of interacting nuclei and electrons, whose dynamics and interactions are described by the many-particle Schrödinger equation. This equation serves as the cornerstone for predicting observable physical properties of the system.

In the absence of external perturbations, the quantum state of a system comprising electrons and nuclei is described by the time-independent Schrödinger equation:

$$\hat{\mathcal{H}}(\mathbf{r},\mathbf{R})\Psi(\mathbf{r},\mathbf{R}) = E\Psi(\mathbf{r},\mathbf{R}), \tag{2.1}$$

where $\mathbf{r} = \{\mathbf{r}_1, \mathbf{r}_2, \ldots, \mathbf{r}_{N_\mathrm{e}}\}$ represents the coordinates of the electrons, and $\mathbf{R} = \{\mathbf{R}_1, \mathbf{R}_2, \ldots, \mathbf{R}_{N_\mathrm{n}}\}$ corresponds to the coordinates of the nuclei (N_e and N_n label the number of electrons and ions). The Hamiltonian operator $\hat{\mathcal{H}}$ encapsulates the kinetic and potential energy contributions within the system:

$$\hat{\mathcal{H}} = \hat{T}_\mathrm{e}(\mathbf{r}) + \hat{T}_\mathrm{n}(\mathbf{R}) + \hat{V}_\mathrm{ee}(\mathbf{r}) + \hat{V}_\mathrm{en}(\mathbf{r},\mathbf{R}) + \hat{V}_\mathrm{nn}(\mathbf{R}), \tag{2.2}$$

where the terms represent the following physical contributions:

- $\hat{T}_\mathrm{e}$: electronic kinetic energy,
- $\hat{T}_\mathrm{n}$: nuclear kinetic energy,
- $\hat{V}_\mathrm{ee}$: electron-electron interaction potential,
- $\hat{V}_\mathrm{en}$: electron-nucleus interaction potential,
- $\hat{V}_\mathrm{nn}$: nucleus-nucleus interaction potential.

Throughout the thesis, we use Hartree atomic units (i.e., $\hbar = m_e = e = 4\pi\varepsilon_0 = 1$). Under these units, the kinetic energy operators take the form:

$$\hat{T}_{\mathrm{e}} = -\frac{1}{2}\sum_{i=1}^{N_{\mathrm{e}}} \nabla^2_{\mathbf{r}_i}, \tag{2.3}$$

$$\hat{T}_{\mathrm{n}} = -\frac{1}{2}\sum_{j=1}^{N_{\mathrm{n}}} \frac{1}{M_j}\nabla^2_{\mathbf{R}_j}. \tag{2.4}$$

The potential energy terms describing Coulomb interactions among particles are given by:

$$\hat{V}_{\mathrm{ee}} = \sum_{i<j}^{N_{\mathrm{e}}} \frac{1}{|\mathbf{r}_i - \mathbf{r}_j|}, \tag{2.5}$$

$$\hat{V}_{\mathrm{en}} = \sum_{i}^{N_{\mathrm{e}}}\sum_{j}^{N_{\mathrm{n}}} \frac{Z_j}{|\mathbf{r}_i - \mathbf{R}_j|}, \tag{2.6}$$

$$\hat{V}_{\mathrm{nn}} = \sum_{i<j}^{N_{\mathrm{n}}} \frac{Z_i Z_j}{|\mathbf{R}_i - \mathbf{R}_j|}, \tag{2.7}$$

where Z_j denotes the nuclear charge of ion j.

Due to the complexity of the many-particle Schrödinger equation, its direct solution for realistic systems is computationally infeasible, as the computational resources required scale exponentially with the number of particles. Thus, various approximations are employed to make the problem tractable.

2.1.1. Adiabatic approximation

In quantum chemistry calculations, the most widely used approximation is the adiabatic approximation, which relies on the large mass difference between nuclei and electrons. This approximation simplifies the many-particle problem by assuming that the nuclei move much more slowly compared to the electrons. Such separation of time scales allows the total wavefunction to be factorized into electronic and nuclear components. In the formal analysis presented in this thesis, we use the simplest form of the adiabatic approximation, often referred to as the static adiabatic approximation [46] (not to be confused with the Born–Oppenheimer approximation). In this framework, the nuclear kinetic energy term is initially neglected, leading to the electronic Hamiltonian:

$$\hat{\mathcal{H}}_{\mathrm{e}} = \hat{T}_{\mathrm{e}} + \hat{V}_{\mathrm{ee}} + \hat{V}_{\mathrm{en}}. \tag{2.8}$$

The electronic Schrödinger equation is then solved for a fixed nuclear configuration, $\mathbf{R}_0$, yielding a set of electronic states $\psi_i(\mathbf{r}, \mathbf{R}_0)$ with corresponding energies ε_i. The exact solution to the full molecular Hamiltonian (2.2) can then be expressed as a linear combination of these electronic wave functions:

$$\Psi(\mathbf{r}, \mathbf{R}) = \sum_i \chi_i(\mathbf{R})\, \psi_i(\mathbf{r}, \mathbf{R_0}), \tag{2.9}$$

where the coefficients $\chi_i(\mathbf{R})$ are unknown functions of the nuclear coordinates. Substituting the expansion (2.9) into Eq. (2.1) yields a set of coupled equations for the nuclear coefficients:

$$\hat{T}_n \chi_j(\mathbf{R}) + \sum_i \langle \psi_j | \hat{V} | \psi_i \rangle \chi_i(\mathbf{R}) = (E - \varepsilon_j)\, \chi_j(\mathbf{R}), \tag{2.10}$$

where the potential operator is defined as $\hat{V} = \hat{V}_{ee} + \hat{V}_{en} + \hat{V}_{nn}$, and the matrix elements $\langle \psi_j | \hat{V} | \psi_i \rangle$ are evaluated over the electronic coordinates $\mathbf{r}$. The static adiabatic approximation is derived by neglecting the off-diagonal matrix elements of the nuclear potential, i.e.,

$$\langle \psi_j | \hat{V} | \psi_i \rangle = 0, \quad \text{for } j \neq i. \tag{2.11}$$

This assumption implies that the nuclear potential and motion do not couple different electronic states. As a result, Eq. (2.10) decouples into a set of independent nuclear Schrödinger equations:

$$\left(\hat{T}_n + \hat{V}_i\right) \chi_i(\mathbf{R}) = (E - \varepsilon_i)\, \chi_i(\mathbf{R}), \tag{2.12}$$

where

$$\hat{V}_i = \langle \psi_i | \hat{V} | \psi_i \rangle,$$

defines the adiabatic potential energy surface (APES) for electronic state ψ_i. The solutions of Eq. (2.12) yield the adiabatic form of the total wave function:

$$\Psi_i(\mathbf{r}, \mathbf{R}) = \chi_i(\mathbf{R})\, \psi_i(\mathbf{r}, \mathbf{R}_0). \tag{2.13}$$

In summary, we first solve the electronic Schrödinger equation, then determine the adiabatic potential energy surfaces (APES) for the selected electronic states of interest. Once these surfaces have been established, we solve the nuclear Schrödinger equation (2.12) to obtain the corresponding vibrational wave functions, $\chi_i(\mathbf{R})$.

The approximation (2.11) is valid when the electronic states of interest are separated by relatively large energy gaps; however, it fails when these separations are on the order of phonon excitation quanta [47]. This limitation is addressed in detail in Section 2.4.

Even with the adiabatic approximation, solving the many-particle electronic Schrödinger equation is a formidable challenge due to the intricate interactions among electrons. These interactions introduce strong many-body correlations that scale exponentially with system size, making direct numerical solutions impractical for all but the smallest systems. As the number of electrons increases, the dimensionality of the problem grows rapidly, and in systems like solids with defects, the vast number of interacting particles far exceeds computational capabilities. This necessitates the development of advanced computational strategies and further approximations to accurately approximate the system's behavior within practical means.

2.2. Density functional theory

In this thesis, the chosen computational approach is density functional theory (DFT), originally formulated by Hohenberg and Kohn [48, 49]. DFT has become the most widely used *ab initio* (meaning from first principles) method for electronic structure calculations of solid-state systems due to its capability to efficiently handle systems containing up to several thousand atoms. Unlike traditional methods that rely on the many-electron wave function, DFT simplifies the problem by utilizing the electron density $n(\mathbf{r})$, which depends only on three spatial coordinates. The electron density represents the probability of finding an electron within an infinitesimal volume element and is mathematically defined as:

$$n(\mathbf{r}) = \langle\psi|\hat{n}(\mathbf{r})|\psi\rangle = \langle\psi|\sum_i^{N_\mathrm{e}} \delta(\mathbf{r}-\mathbf{r}_i)|\psi\rangle \tag{2.14}$$

$$= N_\mathrm{e} \int |\psi(\mathbf{r}, s_1, \mathbf{x}_2, \ldots, \mathbf{x}_{N_\mathrm{e}})|^2 \,\mathrm{d}s_1 \,\mathrm{d}\mathbf{x}_2 \cdots \,\mathrm{d}\mathbf{x}_{N_\mathrm{e}}, \tag{2.15}$$

where $\mathbf{x}_i = (\mathbf{r}_i, \sigma_i)$ includes both spatial and spin coordinates. Conventional wavefunction-based methods determine the ground state energy by minimizing the energy expectation value with respect to the total wave function ψ:

$$E_0 = \min_\psi \langle\psi|\, \hat{T}_\mathrm{e} + \hat{V}_\mathrm{ee} + \sum_i^{N_\mathrm{e}} \hat{v}_\mathrm{ext}(\mathbf{r}_i) \,|\psi\rangle\,, \tag{2.16}$$

where $\hat{v}_\mathrm{ext}(\mathbf{r})$ is the external potential. Although this wavefunction-based approach provides an exact solution in principle, it becomes computationally unfeasible for large systems due to the exponential scaling with the number of electrons.

An alternative approach is provided by density functional theory, which circumvents the explicit dependence on the wave function by instead considering the electron density as the fundamental variable. This transformation is formally justified by the Hohenberg–Kohn (HK) theorems [48], which form the theoretical foundation of DFT.

2.2.1. The Hohenberg–Kohn theorems

The foundation of density functional theory (DFT) is established by the Hohenberg–Kohn theorems, which form a fundamental link between the electron density and the many-electron wave function $\psi(\mathbf{r}_1, \ldots, \mathbf{r}_{N_\mathrm{e}})$.

The first Hohenberg–Kohn theorem states that: The ground state electron density $n_0(\mathbf{r})$ of a multi-electron system uniquely determines the external potential $\hat{v}_\mathrm{ext}(\mathbf{r})$.

This implies that if two electronic systems with external potentials $\hat{v}_{\mathrm{ext},1}(\mathbf{r})$ and $\hat{v}_{\mathrm{ext},2}(\mathbf{r})$ share the same ground-state electron density, then the potentials must be identical up to an additive constant. This result is fundamental to DFT, as it proves that the ground-state density fully characterizes the electronic properties of a system, containing the same information as the ground-state wave function ψ_0. Consequently, both the ground-state wave function ψ_0 and energy E_0 can be expressed as functionals of the electron density:

$$E_0[n] = \langle \psi_0[n] | \, \hat{T} + \hat{V}_{\mathrm{ee}} + \sum_i^{N_\mathrm{e}} \hat{v}_{\mathrm{ext}}(\mathbf{r}_i) \, | \psi_0[n] \rangle \, . \tag{2.17}$$

By decomposing the functional into its components, the total energy can be rewritten as:

$$E_0[n] = \int n(\mathbf{r}) \hat{v}_{\mathrm{ext}}(\mathbf{r}) \, \mathrm{d}\mathbf{r} + \hat{F}_{\mathrm{HK}}[n], \tag{2.18}$$

where the first term accounts for the interaction of electrons with the external potential, and the remaining term,

$$\hat{F}_{\mathrm{HK}}[n] = \langle \psi_0[n] | \, \hat{T}_\mathrm{e} + \hat{V}_{\mathrm{ee}} \, | \psi_0[n] \rangle \, , \tag{2.19}$$

represents the sum of the kinetic energy and electron-electron interactions. The functional $\hat{F}_{\mathrm{HK}}[n]$ is independent of the external potential and is commonly referred to as the universal functional, which applies to any electronic system.

The second Hohenberg–Kohn theorem states that: The functional $E_0[n]$ attains its minimum value if and only if the provided density corresponds to the true ground-state density of the system.

This theorem establishes the variational principle, which allows the ground-state energy and electron density to be determined by minimizing the total energy functional:

$$E_0 = \min_n E[n], \tag{2.20}$$

Once the exact ground-state density $n_0(\mathbf{r})$ is determined, it serves as a foundation for obtaining all other ground-state properties of the system. In principle, if the precise form of the universal functional $\hat{F}_{\mathrm{HK}}[n]$ were available, the complexity of solving the many-electron problem would be reduced to simply minimizing the energy functional with respect to the electron density $n(\mathbf{r})$ under the influence of an external potential $\hat{v}_{\mathrm{ext}}(\mathbf{r})$.

However, a major challenge in practical applications of the Hohenberg–Kohn theorems lies in the fact that the explicit analytical form of the functional $\hat{F}_{\mathrm{HK}}[n]$ is not known. As a result, while the theorems provide a rigorous theoretical framework, they do not offer a direct method to obtain the ground-state density $n_0(\mathbf{r})$.

2.2.2. Kohn–Sham formalism

For practical implementation of density functional theory, Kohn and Sham introduced an approach that maps the interacting many-electron system onto a fictitious system of non-interacting electrons, known as the Kohn–Sham (KS) formalism [49]. In the KS formalism, the ground-state density of the interacting system is reproduced by a set of fictious single-particle orbitals ϕ_i^{KS}, referred to as Kohn–Sham orbitals. These orbitals form an antisymmetric Slater determinant:

$$\psi_{\mathrm{KS}} = \frac{1}{\sqrt{N_{\mathrm{e}!}}} \left| \phi_1^{\mathrm{KS}} \phi_2^{\mathrm{KS}} \cdots \phi_{N_{\mathrm{e}}}^{\mathrm{KS}} \right|, \tag{2.21}$$

where the determinant is constructed from the one-electron wavefunctions:

$$\left| \phi_1^{\mathrm{KS}} \phi_2^{\mathrm{KS}} \cdots \phi_N^{\mathrm{KS}} \right| \equiv \det \begin{pmatrix} \phi_1^{\mathrm{KS}}(\mathbf{r}_1) & \phi_2^{\mathrm{KS}}(\mathbf{r}_1) & \cdots & \phi_N^{\mathrm{KS}}(\mathbf{r}_1) \\ \phi_1^{\mathrm{KS}}(\mathbf{r}_2) & \phi_2^{\mathrm{KS}}(\mathbf{r}_2) & \cdots & \phi_N^{\mathrm{KS}}(\mathbf{r}_2) \\ \vdots & \vdots & \ddots & \vdots \\ \phi_1^{\mathrm{KS}}(\mathbf{r}_{N_{\mathrm{e}}}) & \phi_2^{\mathrm{KS}}(\mathbf{r}_{N_{\mathrm{e}}}) & \cdots & \phi_N^{\mathrm{KS}}(\mathbf{r}_{N_{\mathrm{e}}}) \end{pmatrix}. \tag{2.22}$$

The Kohn-Sham wavefunction ψ_{KS} is designed to yield the exact electron density of the interacting system:

$$n(\mathbf{r}) = \sum_{i=1}^{N_{\mathrm{e}}} |\phi_i^{\mathrm{KS}}(\mathbf{r})|^2. \tag{2.23}$$

It is important to note that ψ_{KS} does not represent the true wavefunction of the interacting system but serves as a mathematical tool to compute the exact ground-state density.

The central idea of the KS formalism is to partition the universal functional $\hat{F}_{\mathrm{HK}}[n]$ into three components:

$$\hat{F}_{\mathrm{HK}}[n] = \hat{T}_s^{\mathrm{KS}}[n] + \hat{J}[n] + \hat{E}_{\mathrm{xc}}[n], \tag{2.24}$$

where $\hat{T}_s^{\mathrm{KS}}[n]$ is the kinetic energy of the non-interacting Kohn–Sham electrons, $\hat{J}[n]$ is the classical Coulomb interaction (Hartree term), and $\hat{E}_{\mathrm{xc}}[n]$ is the exchange-correlation functional, which encapsulates all non-classical electron-electron interactions and the residual kinetic energy difference between the interacting and non-interacting systems.

The term for kinetic energy of non-interacting electrons is given by:

$$\hat{T}_s^{\mathrm{KS}}[n] = \sum_i^{N_\mathrm{e}} \langle \phi_i^{\mathrm{KS}} | \hat{T} | \phi_i^{\mathrm{KS}} \rangle, \tag{2.25}$$

The Hartree term, or the classical Coulomb repulsion of an electron density with itself is given by:

$$\hat{J}[n] = \iint \frac{n(\mathbf{r}_1) n(\mathbf{r}_2)}{|\mathbf{r}_2 - \mathbf{r}_1|} \, \mathrm{d}\mathbf{r}_1 \, \mathrm{d}\mathbf{r}_2. \tag{2.26}$$

The final term of Eq.(2.24) is the exchange-correlation energy functional $\hat{E}_{\mathrm{xc}}[n]$ which is formally defined as:

$$\hat{E}_{\mathrm{xc}}[n] = \hat{T}[n] - \hat{T}_s^{\mathrm{KS}}[n] + \hat{V}_{\mathrm{ee}}[n] - \hat{J}[n], \tag{2.27}$$

where $\hat{T}[n]$ is the true kinetic energy of the interacting system, and $\left[\hat{V}_{\mathrm{ee}}[n] - \hat{J}[n]\right]$ represents the non-classical part of electron-electron interaction. The Kohn–Sham equations are derived by minimizing the total energy functional with respect to the density, leading to a set of single-particle Schrödinger-like equations:

$$\left[\hat{T}_i + \hat{v}_{\mathrm{KS}}(\mathbf{r})\right] \phi_i^{\mathrm{KS}} = \varepsilon_i^{\mathrm{KS}} \phi_i^{\mathrm{KS}}, \tag{2.28}$$

where $\hat{v}_{\mathrm{KS}}(\mathbf{r})$ is the effective Kohn–Sham potential, defined as:

$$\hat{v}_{\mathrm{KS}}(\mathbf{r}) = \hat{v}(\mathbf{r}) + \int \frac{n(\mathbf{r})}{|\mathbf{r} - \mathbf{r}'|} \, \mathrm{d}\mathbf{r}' + \hat{v}_{\mathrm{xc}}(\mathbf{r}). \tag{2.29}$$

Here, $\hat{v}(\mathbf{r})$ is the external potential due to the nuclei, and $\hat{v}_{\mathrm{xc}}(\mathbf{r}) = \delta E_{\mathrm{xc}}[n]/\delta n(\mathbf{r})$ is the exchange-correlation potential. The KS equations must be solved self-consistently, as the potential $\hat{v}_{\mathrm{KS}}(\mathbf{r})$ depends on the density $n(\mathbf{r})$, which in turn is constructed from the KS orbitals.

In principle, the KS formalism provides an exact framework for iteratively calculating the ground-state energy and density of a many-electron

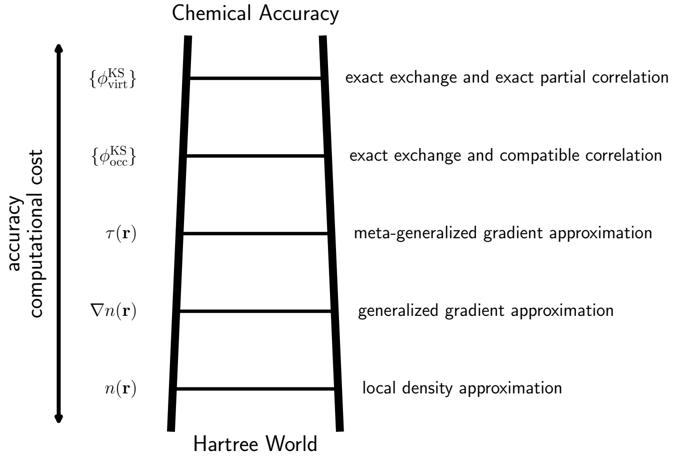
Chemical Accuracy
accuracy
computational cost
$\{\phi^{\mathrm{KS}}_{\mathrm{virt}}\}$
$\{\phi^{\mathrm{KS}}_{\mathrm{occ}}\}$
$\tau(\mathbf{r})$
$\nabla n(\mathbf{r})$
$n(\mathbf{r})$
exact exchange and exact partial correlation
exact exchange and compatible correlation
meta-generalized gradient approximation
generalized gradient approximation
local density approximation
Hartree World

Figure 2.1: The "Jacob's ladder" of density functional approximations, illustrating the hierarchy of increasingly sophisticated functionals [50].

system. However, the accuracy of the results hinges on the quality of the approximation used for the exchange-correlation functional $\hat{E}_{\mathrm{xc}}[n]$. This functional remains the only unknown in the theory and is the subject of ongoing research. In the following subsection, we will discuss the various approximations for $\hat{E}_{\mathrm{xc}}[n]$ and their implications for DFT calculations.

2.2.3. Exchange–correlation functionals

The exact form of the exchange-correlation functional, $\hat{E}_{\mathrm{xc}}[n]$, remains one of the most significant unresolved challenges in quantum chemistry. While relatively small compared to the kinetic and Coulomb energy contributions, $\hat{E}_{\mathrm{xc}}[n]$ plays a crucial role in determining the accuracy of chemical and physical predictions. To organize the progression of functional approximations, Perdew introduced the concept of "Jacob's ladder" [50], depicted in Fig. 2.1, where each rung corresponds to a more advanced and accurate functional form.

2.2.3.1 Local density approximation

The local density approximation (LDA), introduced by Kohn and Sham [49], forms the first rung of Jacob's ladder. It assumes that the exchange-correlation energy at any point depends solely on the local electron density, based on the uniform electron gas model. The LDA functional is given by:

$$\hat{E}_{\mathrm{xc}}^{\mathrm{LDA}}[n_\uparrow, n_\downarrow] = \int \varepsilon_{\mathrm{xc}}^{\mathrm{unif}}(n_\uparrow, n_\downarrow) n(\mathbf{r})\, d\mathbf{r}. \tag{2.30}$$

Here, $n_\sigma(\mathbf{r})$ are electron spin densities with $n(\mathbf{r}) = n_\uparrow(\mathbf{r}) + n_\downarrow(\mathbf{r})$ being the total electron density. $\varepsilon_{\mathrm{xc}}^{\mathrm{unif}}$ represents the exchange-correlation energy per electron in a uniform gas. The exchange term follows Dirac's analytical result [51] for uniform electron gas, while correlation energies are usually obtained from quantum Monte Carlo calculations [52]. Despite its simplicity, LDA performs well for structural and vibrational properties in solids but overestimates binding energies and poorly describes reaction barriers [53].

2.2.3.2 Generalized gradient approximation

The second rung of Jacob's ladder introduces the generalized gradient approximation (GGA) [54–56], which enhances the accuracy of the exchange-correlation functional by incorporating the gradient of the electron density, $\nabla n(\mathbf{r})$. This accounts for the inhomogeneity of the electron distribution, leading to the following functional form:

$$\hat{E}_{\mathrm{xc}}^{\mathrm{GGA}}[n_\uparrow, n_\downarrow] = \int \varepsilon_{\mathrm{xc}}^{\mathrm{GGA}}(n_\uparrow, n_\downarrow, \nabla n_\uparrow, \nabla n_\downarrow) n(\mathbf{r})\, \mathrm{d}\mathbf{r}. \tag{2.31}$$

Here, ∇n_σ are gradients of electron spin densities. GGA functionals improve upon LDA by partially addressing its overbinding issue, resulting in better predictions for bond energies and molecular interactions. The most widely used GGA functional is the non-empirical PBE (Perdew-Burke-Ernzerhof) [56] functional, which is a standard in solid-state physics. However, both LDA and GGA suffer from the well-known underestimation of electronic band gaps.

2.2.3.3 Meta-GGA functionals

The third rung of Jacob's ladder is occupied by meta-GGA functionals, which extend the flexibility of exchange-correlation approximations by incorporating the kinetic energy density, τ_σ:

$$\tau_\sigma = \sum_i \frac{1}{2} \left| \nabla \psi_{i,\sigma}^{\mathrm{KS}} \right|^2, \tag{2.32}$$

where $\psi_{i,\sigma}^{\mathrm{KS}}$ represents the Kohn–Sham orbitals. The exchange-correlation energy for meta-GGA functionals is expressed as [28, 35]:

$$\hat{E}_{\mathrm{xc}}^{\mathrm{MGGA}}[n_\uparrow, n_\downarrow] = \int \varepsilon_{\mathrm{xc}}^{\mathrm{MGGA}}\left(n_\uparrow, n_\downarrow, \nabla n_\uparrow, \nabla n_\downarrow, \tau_\uparrow, \tau_\downarrow\right) n(\mathbf{r})\,\mathrm{d}\mathbf{r}. \tag{2.33}$$

This formulation allows meta-GGA functionals to capture non-local interactions while avoiding the computational complexity of fully non-local integral terms. As a result, they satisfy more exact physical constraints and achieve higher accuracy for diverse systems compared to LDA and GGA.

Among meta-GGA functionals, the SCAN (Strongly Constrained and Appropriately Normed) functional [35] is particularly notable. SCAN was specifically designed to satisfy all possible exact constraints applicable to meta-GGAs. Its developers demonstrated that SCAN outperforms other semi-local functionals in describing lattice properties of solids, such as those included in the LC20 benchmark set [35]. Furthermore, SCAN has proven to be superior in predicting ground-state structural properties, making it an important tool for solid-state systems.

However, despite its advantages, SCAN suffers from numerical instabilities that manifest in certain self-consistent all-electron calculations, particularly for atomic systems [44]. To address these issues, Bartók and Yates proposed a revised functional, rSCAN [44], which retains the accuracy of SCAN for many properties while offering significantly improved numerical stability. This modification made rSCAN more suitable for calculations prone to numerical issues, such as those involving small or highly localized systems.

Nevertheless, rSCAN was found to exhibit reduced transferability in some cases, leading to less accurate predictions of atomization energies [57, 58]. To overcome these limitations, the r^{2}SCAN functional was developed [45]. By combining the numerical stability of rSCAN with the transferable accuracy of SCAN, r^{2}SCAN satisfies all the exact constraints of SCAN while achieving consistent performance across a wide range of systems and properties.

2.2.3.4 Hybrid functionals

The fourth rung of Jacob's ladder is occupied by hybrid functionals, which blend a portion of exact exchange from Hartree–Fock (HF) theory with exchange-correlation approximations from DFT [59]. Becke's three-parameter functional (B3LYP) [60] is a well-known example of a hybrid functional and remains highly popular in molecular quantum chemistry. However, applying hybrid functionals to periodic systems initially faced significant computational challenges due to the high cost of evaluating the exact exchange integrals over delocalized states. To address these issues, the HSE (Heyd-Scuseria-Ernzerhof) functional [61] introduced a range-separated approach that divides the Coulomb operator into short-range (SR) and long-range (LR) components:

$$\frac{1}{r} = \underbrace{\frac{\mathrm{erfc}(\omega r)}{r}}_{\text{short-range}} + \underbrace{\frac{\mathrm{erf}(\omega r)}{r}}_{\text{long-range}}, \tag{2.34}$$

where erf and erfc are the error function and complementary error function, respectively. The parameter ω determines the separation between the short-range and long-range interactions. In the HSE functional, exact HF exchange is included only in the short-range component, while the PBE exchange-correlation functional is applied to both short- and long-range terms. The overall exchange-correlation energy takes the following form:

$$E_{\mathrm{xc}}(\alpha, \omega) = aE_x^{\mathrm{HF,SR}}(\omega) + (1-a)E_x^{\mathrm{PBE,SR}}(\omega) + E_x^{\mathrm{PBE,LR}}(\omega) + E_c^{\mathrm{PBE}}. \tag{2.35}$$

Here, the mixing parameter a determines the fraction of HF exchange included in the short range. For the standard HSE functional, $a = 0.25$ and $\omega = 0.2$. One of the key strengths of the HSE functional is its ability to accurately predict semiconductor band gaps by approximately accounting for the derivative discontinuity of the exchange-correlation energy [62].

The HSE functional has become a ”golden standard” for studying deep-level defects, as it provides accurate predictions of thermodynamic properties and excitation energies. However, it remains computationally expensive, especially for high-throughput calculations or systems with a large number of ions. This computational cost arises from the non-local nature of HF exchange, which scales unfavorably with system size.

2.2.4. DFT implementation

All calculations in this thesis were performed using the Vienna Ab initio Simulation Package (VASP) [63]. VASP employs a plane-wave basis for representing single-particle wavefunctions and uses the projector-augmented wave (PAW) method to effectively separate core and valence electrons. The plane-wave approach is naturally suited for periodic systems such as solids.

2.2.4.1 Plane-wave basis

Crystalline materials exhibit periodicity, allowing the electronic structure to be efficiently described using Bloch's theorem [64]. According to this theorem, the wavefunctions of single-electron states can be expressed as:

$$\phi_{\mathbf{k}}^{\mathrm{KS}}(\mathbf{r}) = e^{i\mathbf{k}\cdot\mathbf{r}} u_{\mathbf{k}}(\mathbf{r}), \tag{2.36}$$

where $\mathbf{k}$ is a wave vector within the first Brillouin zone, and $u_{\mathbf{k}}(\mathbf{r})$ is a function that shares the periodicity of the lattice potential. The periodic component $u_{\mathbf{k}}(\mathbf{r})$ can be expanded in a Fourier series:

$$u_{\mathbf{k}}(\mathbf{r}) = \sum_{\mathbf{G}} C_{\mathbf{G}}(\mathbf{k}) e^{i\mathbf{G}\cdot\mathbf{r}}, \tag{2.37}$$

where the summation runs over all reciprocal lattice vectors $\mathbf{G}$. In practical calculations, the expansion is truncated by imposing a kinetic energy cutoff:

$$\frac{|\mathbf{k}+\mathbf{G}|^2}{2} \leqslant E_{\mathrm{cutoff}}. \tag{2.38}$$

The cutoff energy is chosen based on convergence tests, ensuring that total energy and other properties are adequately described.

To compute observables, integrations over the Brillouin zone are required. These integrals are approximated by a discrete summation over a set of $\mathbf{k}$-points with appropriate weights:

$$\frac{1}{\Omega_{\mathrm{BZ}}} \int_{\mathrm{BZ}} f(\varepsilon)\delta(\varepsilon_{n,\mathbf{k}} - \varepsilon) d\mathbf{k} \quad \approx \quad \sum_{\mathbf{k}} w_{\mathbf{k}} f(\varepsilon_{n,\mathbf{k}}). \tag{2.39}$$

Here, $w_{\mathbf{k}}$ are the weight factors assigned to each $\mathbf{k}$-point. The

Monkhorst–Pack scheme [65] is widely used to generate uniform **k**-point grids, with the optimal grid density determined through convergence tests. However, for point defect calculations, where the translational symmetry of the crystal is disrupted, the Brillouin zone is typically sampled only at the Γ point and employing a large supercell (see Section 2.2.4.3) containing several hundred atoms, which minimizes artificial defect-defect interactions.

2.2.4.2 Pseudopotentials

Although plane waves are well suited for periodic systems, they pose computational challenges in describing core electrons, which exhibit rapid oscillations near the nuclei due to orthogonality constraints with valence states. A direct representation of these core states in a plane-wave basis would require an impractically large number of basis functions. The pseudopotential approach circumvents this problem by leveraging two key observations:

- chemical bonding is primarily governed by valence electrons,
- wavefunctions in the bonding region, away from the core, are smoother than near the nucleus.

The pseudopotential method replaces the all-electron wavefunction with a smooth pseudo-wavefunction that is identical to the true wavefunction outside a defined core region, while eliminating the need to explicitly treat core states.

In this work, we use the PAW method [66], which offers superior transferability compared to traditional norm-conserving or ultrasoft pseudopotentials. PAW reconstructs the all-electron wavefunction ψ_{AE} from the pseudo-wavefunction ψ_{PS} using a linear transformation:

$$\psi_{\mathrm{PS}} = \hat{\mathrm{T}}\psi_{\mathrm{AE}}. \tag{2.40}$$

The transformation operator $\hat{\mathrm{T}}$ is chosen such that the pseudo-wavefunction smoothly transitions into the all-electron wavefunction inside the augmentation sphere around each atom. This formalism ensures that calculations remain computationally efficient while retaining accuracy in electronic structure calculations.

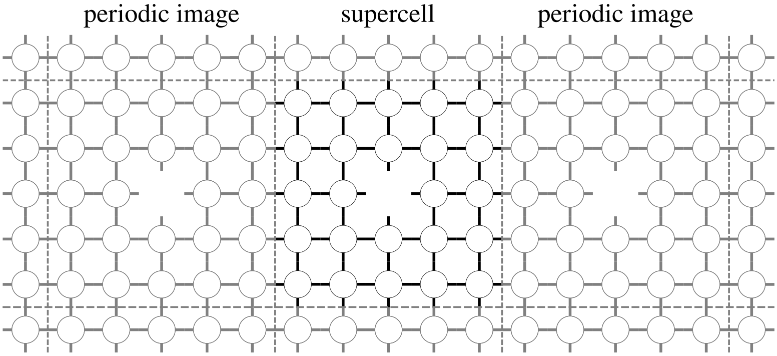

Figure 2.2: Schematic representation of the supercell method for a point defect in a solid (specifically a vacancy in this example). The supercell is delineated by dashed lines, while its periodic images are shown in gray.

The PAW method is particularly advantageous for computing matrix elements and derived properties, as it allows for the reconstruction of all-electron wavefunctions without significantly increasing computational cost. Given its accuracy and efficiency, PAW has become the standard approach for many electronic structure calculations, including those performed in this thesis.

2.2.4.3 Supercell approach

From a theoretical perspective, an ideal crystal is an infinitely periodic structure that can be effectively described using a repeating unit cell, which encapsulates the fundamental structural and symmetry properties of the lattice. However, the introduction of a defect breaks this periodicity, necessitating alternative theoretical frameworks to accurately model the system.

A widely adopted approach in practical calculations is the supercell method [38], wherein a large, periodically repeated unit cell containing the defect (see Fig. 2.2) is used to approximate its behavior within an extended solid. Although supercell models are inherently finite, they can yield meaningful insights when carefully converged with respect to system size.

Modern computational capabilities enable us to model supercells containing up to a few thousand atoms, which is typically sufficient for capturing the electronic structure of deep-level defects. However, these system sizes are often too limited to accurately reproduce the vibrational structure and interactions with bulk-like, long-wavelength phonons. This limitation will be addressed in Section 2.6.

2.3. Vibrational structure

2.3.1. Harmonic approximation

The electronic Schrödinger equation can be formally solved for any nuclear configuration $\mathbf{R}_0$. However, in practical applications, we are primarily interested in nuclear motion around the equilibrium geometry, which corresponds to a minimum of the APES. The process of locating this minimum is referred to as ionic relaxation.

Ionic relaxation involves computing atomic forces, which can then be used in optimization algorithms such as quasi-Newton or conjugate gradient methods [28] to identify local minima. The nuclear forces are obtained from the Hellmann–Feynman theorem:

$$\mathbf{F}_{\mathbf{R}_{0,n}} = -\frac{\partial \varepsilon_i}{\partial \mathbf{R}_{0,n}} = \langle \psi_i | \frac{\partial \hat{V}(\mathbf{r}, \mathbf{R}_0)}{\partial \mathbf{R}_{0,n}} | \psi_i \rangle \, . \tag{2.41}$$

Here, $\mathbf{R}_{0,n}$ represents the coordinate of the n-th nucleus, ε_i is the electronic energy, and $\hat{V}(\mathbf{r}, \mathbf{R}_0)$ is the potential energy in the electronic Schrödinger equation. This energy consists of two terms: the electron–nucleus interaction potential $\hat{V}_{\mathrm{en}}(\mathbf{r}, \mathbf{R}_0)$ and the nucleus–nucleus interaction potential $\hat{V}_{\mathrm{nn}}(\mathbf{R}_0)$ [Eqs. (2.6) and (2.7)]. Consequently, the force depends explicitly on the electron density:

$$\mathbf{F}_{\mathbf{R}_{0,n}} = \int n(\mathbf{r}) \frac{\partial \hat{V}_{\mathrm{en}}(\mathbf{r}, \mathbf{R}_0)}{\partial \mathbf{R}_{0,n}} \mathrm{d}\mathbf{r} + \frac{\partial \hat{V}_{\mathrm{nn}}(\mathbf{R}_0)}{\partial \mathbf{R}_{0,n}}, \tag{2.42}$$

which can be directly computed using DFT. For further analysis, we assume the system is in equilibrium. At equilibrium ($\mathbf{u} = 0$), the total potential energy can be expanded around $\mathbf{R}_0$:

$$\begin{aligned} \hat{V}_i = \langle \psi_i | \hat{V}(\mathbf{r}, \mathbf{R}) | \psi_i \rangle &= \langle \psi_i | \hat{V}(\mathbf{r}, \mathbf{R}_0) | \psi_i \rangle \\ &+ \sum_n \langle \psi_i | \frac{\partial \hat{V}}{\partial \mathbf{u}_n} | \psi_i \rangle \, \mathbf{u}_n + \frac{1}{2} \sum_{n,m} \langle \psi_i | \frac{\partial^2 \hat{V}}{\partial \mathbf{u}_n \partial \mathbf{u}_m} | \psi_i \rangle \, \mathbf{u}_n \mathbf{u}_m + O(\mathbf{u}^3), \end{aligned} \tag{2.43}$$

where $\mathbf{u}_n$ denotes the atomic displacement from equilibrium $\mathbf{R}_0$. At equilibrium, the first-order term vanishes and the zero-order term, being merely an energy offset, can be ignored. Therefore, the harmonic approximation focuses only on the quadratic terms:

$$\hat{V}_i^{\mathrm{har}}(\mathbf{u}) = \frac{1}{2}\sum_{n,m} \mathbf{\Phi}_{nm}\mathbf{u}_n\mathbf{u}_m. \tag{2.44}$$

The coefficients form the force constant matrix $\mathbf{\Phi}_{nm}$ (or Hessian matrix), which characterizes interatomic interactions and is defined as:

$$\mathbf{\Phi}_{nm} = \langle\psi_i|\frac{\partial^2\hat{V}}{\partial\mathbf{u}_n\partial\mathbf{u}_m}|\psi_i\rangle = \frac{\partial^2 V_i}{\partial\mathbf{u}_n\partial\mathbf{u}_m} \tag{2.45}$$

Within this approximation, the vibrational Hamiltonian takes the form:

$$\hat{H}_v = \sum_n \frac{\mathbf{p}_n^2}{2M_n} + \frac{1}{2}\sum_{n,m} \mathbf{\Phi}_{nm}\mathbf{u}_n\mathbf{u}_m. \tag{2.46}$$

Solving the eigenvalue problem for this Hamiltonian remains computationally challenging due to nuclear coupling through $\mathbf{\Phi}_{nm}$. However, a transformation to normal coordinates, where kinetic and potential energy terms become diagonal, simplifies the problem. This transformation is achieved by solving the classical equations of harmonic motion.

2.3.1.1 Classical solution

The equations of motion for the nuclear degrees of freedom in the harmonic approximation follow from the Hamiltonian:

$$M_n\ddot{\mathbf{u}}_n = -\sum_m \mathbf{\Phi}_{nm}\mathbf{u}_m. \tag{2.47}$$

This system of coupled second-order differential equations describes the vibrational dynamics of the nuclei. Assuming a stationary solution of the form:

$$\mathbf{u}_n(t) = \mathbf{w}_n \exp(-i\omega t), \tag{2.48}$$

where $\mathbf{w}_n$ is a three-dimensional amplitude vector characterizing the mode shape, we obtain the generalized eigenvalue equation:

$$\mathbf{\Phi}\mathbf{w} = \omega^2\hat{\mathbf{M}}\mathbf{w}. \tag{2.49}$$

Here, $\hat{\mathbf{M}}$ is the mass matrix, defined as $||\hat{\mathbf{M}}||_{mn} = M_n \delta_{mn}$. To simplify the problem, we introduce mass-weighted coordinates $\boldsymbol{\eta}_n$:

$$\boldsymbol{\eta}_n = \sqrt{M_n}\mathbf{w}_n. \tag{2.50}$$

In this representation, Eq. (2.49) transforms into the standard eigenvalue problem:

$$\hat{D}\boldsymbol{\eta} = \omega^2 \boldsymbol{\eta}, \tag{2.51}$$

where $\hat{D}$ is the dynamical matrix, defined as:

$$\hat{\mathbf{D}} = \hat{\mathbf{M}}^{-1/2} \boldsymbol{\Phi} \hat{\mathbf{M}}^{-1/2}, \quad \text{or equivalently,} \quad \hat{\mathbf{D}}_{nm} = \frac{\boldsymbol{\Phi}_{nm}}{\sqrt{M_n M_m}}. \tag{2.52}$$

The solutions of Eq. (2.51) provide the eigenfrequencies ω_k and the corresponding orthonormal eigenvectors $\boldsymbol{\eta}_k$, which describe the stationary vibrational modes of the system.

2.3.1.2 Quantum-mechanical solution

After obtaining the classical vibrational solution, we introduce normal coordinates Q_k, which describe the collective nuclear motion:

$$Q_k = \sum_n \sqrt{M_n}(\mathbf{R}_n - \mathbf{R}_{0,n})\boldsymbol{\eta}_{k;n}, \tag{2.53}$$

where $\mathbf{R}_n$ is the position of atom n, while $\mathbf{R}_{0,n}$ is its equilibrium position, and $\boldsymbol{\eta}_{k;n}$ represents the eigenvectors of the dynamical matrix $\hat{\mathbf{D}}$, characterizing the displacement components for mode k at atom n. Transforming into normal coordinates diagonalizes the kinetic and potential energy terms:

$$\sum_n \frac{\mathbf{p}_n^2}{2M_n} = \frac{1}{2}\sum_k \frac{\partial^2}{\partial Q_k^2}, \quad \frac{1}{2}\sum_{nm} \hat{\mathbf{D}}_{nm}\boldsymbol{\eta}_n\boldsymbol{\eta}_m = \frac{1}{2}\sum_k \omega_k^2 Q_k^2. \tag{2.54}$$

Thus, in this basis of normal coordinates, the vibrational Hamiltonian simplifies to a sum of independent harmonic oscillators:

$$\hat{H}_v = \sum_k \hat{H}_v^k, \quad \text{where} \quad \hat{H}_v^k = \frac{1}{2}\frac{\partial^2}{\partial Q_k^2} + \frac{1}{2}\omega_k^2 Q_k^2. \tag{2.55}$$

Since for every k, the $[\hat{H}_v^k, \hat{H}_v^{k'}] = 0$, the eigenfunctions can be expressed as a product of one-dimensional harmonic oscillator wavefunctions:

$$\chi(\mathbf{Q}) = \chi_1(Q_1)\chi_2(Q_2)\cdots\chi_{3N_n}(Q_{3N_n}), \tag{2.56}$$

where each function $\chi_k(Q_k)$ is obtained by solving the Schrödinger equation:

$$\hat{H}_v^k \chi_k(Q_k) = \epsilon_k \chi_k(Q_k). \tag{2.57}$$

Each mode follows the quantum harmonic oscillator energy spectrum:

$$\epsilon_k = \omega_k \left(n_k + \frac{1}{2}\right), \tag{2.58}$$

where $n_k = 0, 1, 2, \ldots$ is the vibrational quantum number. The total vibrational energy is the sum of individual mode contributions:

$$E_v = \sum_k \epsilon_{n_k}. \tag{2.59}$$

In summary, solving the vibrational problem requires diagonalizing the dynamical matrix [Eq. (2.52)]. This yields quantum-mechanical vibrational states, represented as independent harmonic oscillators. However, direct diagonalization is infeasible for solids due to the effectively infinite number of degrees of freedom. The next section explores how translational symmetry simplifies the vibrational problem in periodic systems.

2.3.2. Crystal vibrations

Translational symmetry in periodic crystals simplifies vibrational analysis. Each atomic position is given by:

$$\mathbf{R}_n^\alpha = \mathbf{R}^\alpha + \mathbf{R}_n, \tag{2.60}$$

where $\mathbf{R}^\alpha$ is the position of unit cell α and $\mathbf{R}_n$ is the atomic position within the unit cell. The dynamical matrix satisfies:

$$\hat{\mathbf{D}}_{mn}(\mathbf{R}^\alpha + \mathbf{L}, \mathbf{R}^\beta + \mathbf{L}) = \hat{\mathbf{D}}_{mn}(\mathbf{R}^\alpha, \mathbf{R}^\beta), \tag{2.61}$$

where $\mathbf{L}$ is a lattice vector. By Bloch's theorem, the eigenvectors take the form:

$$\boldsymbol{\eta}_n(\mathbf{R}^\alpha) = e^{i\mathbf{q}\mathbf{R}^\alpha}\tilde{\boldsymbol{\eta}}_{\mathbf{q}n}, \tag{2.62}$$

where $\mathbf{q}$ is any vector and $\tilde{\boldsymbol{\eta}}_{\mathbf{q}n}$ is a lattice-periodic part. Substituting this into the equations of motion with $\mathbf{R}^\alpha = 0$ gives:

$$\hat{\mathbf{D}}(\mathbf{q})\tilde{\boldsymbol{\eta}}(\mathbf{q}) = \omega(\mathbf{q})^2\tilde{\boldsymbol{\eta}}(\mathbf{q}), \tag{2.63}$$

where the reduced dynamical matrix is:

$$\hat{\mathbf{D}}_{nm}(\mathbf{q}) = \sum_\beta \hat{\mathbf{D}}_{mn}(0, \mathbf{R}^\beta)e^{i\mathbf{q}\mathbf{R}^\beta}. \tag{2.64}$$

Phonon dispersion relations are computed within the first Brillouin zone (FBZ), using the equivalence:

$$e^{i(\mathbf{q}+\mathbf{G})\mathbf{R}^\beta} = e^{i\mathbf{q}\mathbf{R}^\beta}, \tag{2.65}$$

for any reciprocal lattice vector $\mathbf{G}$. In practice, phonon calculations are performed along paths inside FBZ.

2.3.3. Defect-related vibrations

A point defect in a crystal disrupts periodic symmetry, altering the vibrational structure compared to the perfect lattice. As a result, the normal mode analysis used for periodic systems is no longer directly applicable. However, since the defect is localized within a small region, its perturbations to the vibrational structure of bulk remain spatially confined.

The Green's function approach has historically been used to study defect-induced vibrational modes [67, 68], providing insights into their qualitative properties. However, its practical application is challenging, particularly when determining precise vibrational mode shapes. Instead, the supercell approach is commonly employed for a quantitative analysis of defect vibrations [38].

2.3.3.1 Localized and quasi-localized modes

Defects can introduce vibrational modes either within a phonon bandgap or as modifications to bulk modes. Modes confined near the defect with large amplitudes are called localized modes, which decay rapidly with distance and are independent of system size. Strong electron–lattice interactions can make these modes detectable in luminescence, infrared, or Raman spectra.

In contrast, if the frequency of defect-induced mode lies within the bulk phonon spectrum, the vibrational mode is less localized. In this region, the vibrational perturbation is typically characterized by collections of quasi-localized modes. These resonance modes (or quasi-local modes) manifest as peaks in the vibrational spectrum, typically associated with a sharp increase in impurity vibration amplitude at specific frequencies. They commonly occur when defects reduce local force constants. Unlike localized modes, their amplitude at the defect site scales as $N_n^{-1/2}$, where N_n is the number of atoms. As the system size increases, more modes contribute to the resonance.

Resonances play a crucial role in electron–phonon interactions, as the collective increase in vibrational amplitude near the defect enhances coupling between the lattice and electronic states.

2.4. Jahn–Teller effect

In our previous discussion of the electronic and vibrational structure of crystal defects, an adiabatic framework was employed to separate the nuclear and electronic degrees of freedom. This approximation holds when the electronic states of interest are separated by energy gaps that exceed typical phonon energies. However, in the case of paramagnetic point defects, high-symmetry atomic arrangements often lead to electronic degeneracies. With a zero energy gap between these degenerate states, complex non-adiabatic interactions arise between the electronic and vibrational degrees of freedom. This phenomenon is known as the Jahn–Teller (JT) effect [47, 69–71].

In their seminal work, Jahn and Teller [69] demonstrated that in a nonlinear molecule with a degenerate electronic state, forces will emerge on the nuclei along a symmetry-breaking direction, leading to a distortion of the molecular geometry that lifts the degeneracy. However, when addressing the dynamical problem of a coupled electron–phonon system of a degenerate electronic state, Longuet-Higgins et al. [71] demonstrated that for moderate electron–phonon interactions, the local symmetry and overall degeneracy remain intact. Instead, the Jahn–Teller interactions lead to modifications of the vibronic states relative to the adiabatic picture discussed above. This behavior is known as the dynamical Jahn–Teller (DJT) effect [71, 72]. Notably, static symmetry breaking of the nuclear configuration is only observed when the non-adiabatic Jahn–Teller interactions are sufficiently strong.

Among the various types of degeneracies encountered in crystal point defects, the most common is an orbital doublet (two electronic states share the same energy), typically denoted as E, which arises in trigonal symmetry systems. In this thesis, we focus exclusively on such degeneracies. The dynamical Jahn–Teller (DJT) effect associated with an E doublet modifies the effective Hamiltonians governing measurable electronic properties, such as spin–orbit splitting and the system's response to external perturbations [72, 73]. Moreover, the DJT interactions influence the optical features in emission or absorption spectra, leading to spectral characteristics that deviate from those expected in a purely adiabatic system, which is the focus of this thesis.

2.4.1. $E \otimes (e \oplus e \oplus \cdots)$ Jahn–Teller Hamiltonian

Using group theory analysis [47], for orbital doublet E systems non-adiabatic coupling occurs via degenerate, symmetry-breaking vibrational modes that share the same symmetry as the orbital states (typically denoted by lowercase e). Systems with such interaction are commonly referred to as $E \otimes (e \oplus e \oplus \cdots)$ systems, reflecting the coupling between the electronic E state and a set of e vibrational modes. In contrast, symmetry-preserving modes (usually denoted by a or a_1) do not participate in this electron–phonon interaction, and their degrees of freedom can be separated from the electronic subsystem, as in the adiabatic description.

In a formal analysis of doubly degenerate electronic and vibrational states, one has the freedom to choose any pair of orthogonal states that share the same energy or frequency. A common and particularly convenient choice is the Cartesian representation. In this basis, the states (or vibrational modes) are chosen to transform under point-group symmetry operations in the same manner as the Cartesian x and y vectors, with the symmetry axis aligned along the z direction. For instance, under a $2\pi/3$ rotation, the state $|E_x\rangle$ is chosen such that it transforms as $|E_x\rangle \to -\frac{1}{2}\,|E_x\rangle + \frac{\sqrt{3}}{2}\,|E_y\rangle$.

For the derivation of the Hamiltonian describing JT interactions, it is necessary to relax the adiabatic assumption that vibrational motion does not couple to degenerate electronic states (i.e., $\langle E_j|\hat{V}|E_i\rangle = 0$ for states E_i and E_j that share the same energy). Under these conditions, the overall wave function can no longer be expressed in the adiabatic form given by Eq. (2.13). For JT-active systems, it is instead represented in the vibronic form:

$$\Psi(\mathbf{r}, \mathbf{Q}) = \chi_n^a(\mathbf{Q}_a)\,\Phi_m(\mathbf{Q}_e, \mathbf{r}), \tag{2.66}$$

where $\chi_n^a(\mathbf{Q}_a)$ represents the vibrational wave function corresponding to the symmetry-preserving (JT inactive) degrees of freedom, described by the set of normal coordinates $\mathbf{Q}_a$. The JT-active part is encapsulated in the wave function

$$\Phi_m(\mathbf{Q}_e, \mathbf{r}) = \chi_m^{e;x}(\mathbf{Q}_e)\,|E_x\rangle + \chi_m^{e;y}(\mathbf{Q}_e)\,|E_y\rangle\,, \tag{2.67}$$

which reflects the entanglement between the two degenerate electronic states, E_x and E_y, and their associated vibrational states, $\chi_m^{e;x}(\mathbf{Q}_e)$ and $\chi_m^{e;y}(\mathbf{Q}_e)$, pertaining to JT-active degrees of freedom.

The JT Hamiltonian describing the states defined in Eq. (2.67) is derived by expanding the matrix elements $\langle E_j|\hat{V}|E_i\rangle$ in terms of the normal coordinates associated with the e symmetry vibrational modes [47]. Retaining only the linear terms in this expansion yields a vibronic Hamiltonian of the form

$$\mathcal{H} = \mathcal{H}_0 + \mathcal{H}_{\mathrm{JT}},$$

where $\mathcal{H}_0$ represents the vibrational motion within a harmonic potential, and $\mathcal{H}_{\mathrm{JT}}$ encompasses all linear interactions arising from non-adiabatic effects. In the electronic basis of E_x and E_y orbitals, the zero-order Hamiltonian is given by:

$$\mathcal{H}_0 = \sum_{k;\,\gamma\in\{x,y\}} \left(-\frac{\hbar^2}{2}\frac{\partial^2}{\partial Q_{k,\gamma}^2} + \frac{1}{2}\omega_k^2\,Q_{k,\gamma}^2 \right)\hat{\mathbb{I}}. \tag{2.68}$$

Here, the index $k = 1, \dots, N$ enumerates all pairs of degenerate e-symmetry vibrations, $\gamma \in \{x, y\}$ distinguishes the two components of these degenerate vibrations, ω_k denotes the angular frequency of the k-th mode. $\hat{\mathbb{I}}$ is the two-dimensional identity matrix acting on the orbital subspace spanned by the states $|E_x\rangle$ and $|E_y\rangle$. $\mathcal{H}_0$ is identical to Eq. (2.55), meaning that it describes a system of uncoupled harmonic oscillators. This Hamiltonian is used to determine both the vibrational frequencies ω_k and the corresponding zero-order harmonic vibrational solutions.

The JT interaction part of the Hamiltonian is given by [47, 73]:

$$\mathcal{H}_{\mathrm{JT}} = \sum_k \sqrt{2\hbar\omega_k^3}\, K_k \left[\hat{C}_{E_x}\, Q_{k,x} + \hat{C}_{E_y}\, Q_{k,y}\right] \tag{2.69}$$

where K_k are the dimensionless vibronic coupling constants [74], and $\hat{C}_{E_\gamma}$ represents the Clebsch–Gordan (CG) coefficient matrices, as determined by group-theoretical analysis [47]. For the chosen Cartesian x, y representation of the degenerate states, the CG matrices take the form:

$$\hat{C}_{E_x} = \frac{1}{\sqrt{2}} \begin{pmatrix} 0 & 1 \\ 1 & 0 \end{pmatrix}, \quad \hat{C}_{E_y} = \frac{1}{\sqrt{2}} \begin{pmatrix} 1 & 0 \\ 0 & -1 \end{pmatrix}. \tag{2.70}$$

2.4.2. Practical ab initio approach for solving the Jahn–Teller problem

In this section, we outline a practical ab initio approach to address the Jahn–Teller problem, with the primary objective of obtaining solutions of the form (2.67).

The procedure begins with solving the Schrödinger equation for the zero-order Hamiltonian [Eq. (2.68)], which, by design, excludes non-adiabatic contributions. To effectively suppress the Jahn–Teller interactions in DFT calculations, we adopt the strategy described in Refs. [34, 75]. This method employs an electronic configuration with fractional occupations, where the Kohn–Sham wave function is constructed by assigning a fractional occupation of 0.5 electrons to each of the two degenerate orbitals. Such a configuration simulates an ensemble of two degenerate electronic states with equal probability, thereby quenching the JT interactions and preserving the high symmetry of the system [76]. With this configuration, the potential energy surface for e

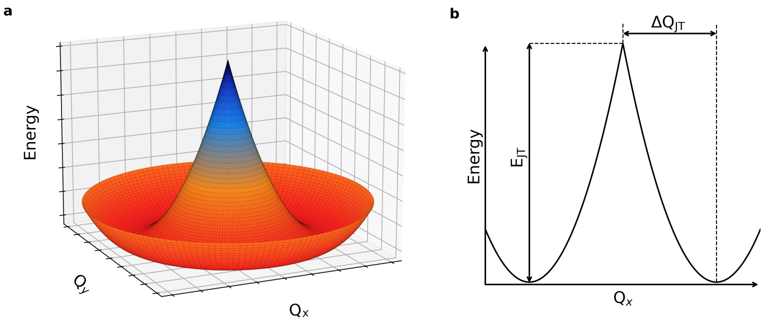

Figure 2.3: **a** The characteristic ”sombrero-hat” shape of the APES arising from the linear JT effect in an $E \otimes e$ system. **b** The one-dimensional cross-section of the APES, illustrating the JT stabilization energy, E_{JT}, and the corresponding distortion amplitude, $\Delta \mathrm{Q}_{\mathrm{JT}}$.

modes is harmonic and vibrational modes can be computed using standard computational techniques and subsequently classified according to the irreducible representations of the corresponding point group.

Once the vibrational modes are determined, the next step involves estimating the vibronic coupling constants, K_k [see Eq. (2.69)], associated with each vibrational doublet k. These constants can be extracted by analyzing the potential energy surface of the $E \otimes (e \oplus e \oplus \cdots)$ system [34]. In particular, for the normal coordinates corresponding to the symmetry-breaking degenerate e modes, the potential of a linear JT system typically exhibits the characteristic ”sombrero-hat” profile (see Fig. 2.3) [47].

The practical analysis of the potential energy surface begins with the high-symmetry configuration obtained via partial occupation. By subsequently removing the fractional occupation and reassigning the electrons to represent a single degenerate state, the system relaxes further along the symmetry-breaking e directions, thereby reaching the minimum of the energy surface. The displacement associated with this relaxation, denoted as $\Delta \mathbf{Q}_{\mathrm{JT}}$, is then projected onto each pair k of e-symmetry normal modes. This projection yields the vibronic coupling constants through the relation [34]:

$$K_k^2 = \frac{\omega_k \, \Delta Q_k^2}{2\hbar}, \tag{2.71}$$

where $\Delta Q_k^2 = \Delta Q_{kx}^2 + \Delta Q_{ky}^2$ represents the squared displacement of the k-th vibrational doublet along its two Cartesian components.

The final step involves the construction and diagonalization of the Hamiltonian describing the Jahn–Teller system. The JT Hamiltonian, $\mathcal{H}_{\mathrm{JT}}$, is constructed in the basis of zero-order vibrational states obtained by solving $\mathcal{H}_0$. To make practical calculations feasible, this basis is truncated to a finite number of total phonon excitations, N_{tot}. However, even with a truncated basis limited to a few phonon excitations, the diagonalization of the full Hamiltonian, $\mathcal{H} = \mathcal{H}_0 + \mathcal{H}_{\mathrm{JT}}$, remains computationally prohibitive for systems with a large number of vibrational modes. To address this challenge, we adopt strategies proposed in Ref. [34], which involve identifying aditional symmetry of the linear JT system and method of few effective modes.

Following symmetry arguments from Refs. [34, 71, 77], both the JT Hamiltonian $\hat{\mathcal{H}}_{\mathrm{JT}}$ and the zero-order Hamiltonian $\mathcal{H}_0$ commute with the quasi-angular momentum operator,

$$\hat{J} = \hat{J}_{\mathrm{el}} + \hat{J}_{\mathrm{ph}}, \tag{2.72}$$

$$\hat{J}_{\mathrm{el}} = \frac{1}{2}\hat{\sigma}_y, \tag{2.73}$$

$$\hat{J}_{\mathrm{ph}} = \mathcal{C}_z \sum_k \mathcal{L}_k, \tag{2.74}$$

where $\hat{J}_{\mathrm{el}}$ acts on the orbital component of the wave function, with $\hat{\sigma}_y$ being the Pauli matrix in the Cartesian representation. The operator $\hat{J}_{\mathrm{ph}}$ quantifies the total angular momentum of the e-symmetry harmonic modes, and $\mathcal{L}_k$ is the angular momentum operator for the k-th vibrational doublet, defined as

$$\mathcal{L}_k = i\left(Q_{kx}\frac{\partial}{\partial Q_{ky}} - Q_{ky}\frac{\partial}{\partial Q_{kx}}\right). \tag{2.75}$$

This commutation implies that, before diagonalization, one can select a basis of $\mathcal{H}_0$ that is also composed of eigenstates of Eq. (2.72) with well-defined quantum numbers $j = j_{el} + \sum_k l_k$. By symmetry, these states are not coupled by $\mathcal{H}_{\mathrm{JT}}$, allowing the JT problem to be solved separately for each j, thereby reducing the computational complexity.

To achieve this separation, we perform a canonical transformation of variables so that, in the zero-order basis, the electronic states are eigenstates of Eq. (2.73) while the phonon states diagonalize Eq. (2.74). In the new basis, the electronic states transform as spherical harmonics:

$$|E_\pm\rangle = \frac{1}{\sqrt{2}}\left(|E_x\rangle \pm i\,|E_y\rangle\right), \tag{2.76}$$

which correspond to electronic quantum numbers $j_{\text{el}} = \pm\frac{1}{2}$. The symmetric phonon states are defined by introducing creation and annihilation operators that generate circular phonon modes:

$$\hat{a}_{k\pm} = \frac{1}{\sqrt{2}}\left(\hat{a}_{kx} \mp i\,\hat{a}_{ky}\right), \tag{2.77}$$

where $\hat{a}_{kx}$ and $\hat{a}_{ky}$ denote the second quantization operators associated with the Cartesian Q_{kx} and Q_{ky} degrees of freedom, respectively. In this representation, the total number operators for left- and right-handed phonons are defined as

$$\hat{n}_{k\pm} = \hat{a}^\dagger_{k\pm}\hat{a}_{k\pm}, \tag{2.78}$$

while the operator

$$\hat{n}_k = \hat{n}_{k+} + \hat{n}_{k-} \tag{2.79}$$

accounts for the total number of phonon excitations in the kth vibrational mode. Accordingly, the phonon angular momentum operator in Eq. (2.74) becomes

$$\mathcal{L}_k = \hbar\left(\hat{n}_{k+} - \hat{n}_{k-}\right). \tag{2.80}$$

The matrix elements of the Hamiltonians $\mathcal{H}_0$ and $\mathcal{H}_{\text{JT}}$ can be derived following the treatment in Ref. [34]. For the zero-order Hamiltonian, one obtains:

$$\langle n_1 l_1, \ldots, n_N l_N; E_\pm|\hat{\mathcal{H}}_0|n_1 l_1, \ldots, n_N l_N; E_\pm\rangle = \sum_k \hbar\omega_k\left(n_k + 1\right), \tag{2.81}$$

where n_k denotes the total number of excited phonons for the k vibrational doublet and l_k is the respective angular momentum. For the Jahn–Teller interaction Hamiltonian, the relevant off-diagonal matrix elements are:

$$\langle n_1' l_1', \ldots, n_N' l_N'; E_- | \hat{\mathcal{H}}_{\mathrm{JT}} | n_1 l_1, \ldots, n_N l_N; E_+ \rangle \tag{2.82}$$

$$= \sqrt{2} \sum_k K_k \, \hbar\omega_k \, \delta_{l_k', l_k+1} \left[\prod_{j \neq k} \delta_{n_j', n_j} \, \delta_{l_j', l_j} \right] \tag{2.83}$$

$$\times \left[\sqrt{\frac{n_k - l_k}{2}} \, \delta_{n_k', n_k - 1} + \sqrt{\frac{n_k + l_k + 2}{2}} \, \delta_{n_k', n_k + 1} \right]. \tag{2.84}$$

Because the total quasi-angular momentum operator $\hat{J}$ commutes with $\hat{\mathcal{H}}_{\mathrm{JT}}$, the complete Hamiltonian can be diagonalized independently in each subspace characterized by a fixed total quantum number

$$j = j_{\mathrm{el}} + \sum_k l_k.$$

The eigenstates of the full Hamiltonian can be expressed as

$$\begin{aligned} |\Phi_{f;m}\rangle &= \chi^{e;+}_{f;m}(\mathbf{Q}_e) \, |E_+\rangle + \chi^{e;-}_{f;m}(\mathbf{Q}_e) \, |E_-\rangle \\ &= \sum_{s=\{+,-\}} \sum_{\mathbf{nl}} C^s_{f;m,\mathbf{nl}} \, |n_1 l_1 \cdots n_N l_N; E_s\rangle \,, \end{aligned} \tag{2.85}$$

where $C^{\pm}_{f;m,\mathbf{nl}}$ are the expansion coefficients determined through diagonalization. This approach leverages symmetry to simplify the solution of the Jahn–Teller problem, significantly reducing the computational complexity.

To further reduce the computational burden, we adopt an approach based on a reduced set of effective modes [34, 75]. In this framework, the spectral density of the Jahn–Teller coupling is defined as

$$K^2(\hbar\omega) = \sum_k K_k^2 \delta(\hbar\omega - \hbar\omega_k). \tag{2.86}$$

This density is then approximated by a density stemming from a smaller number of effective modes

$$K^2_{\mathrm{eff}}(\hbar\omega) = \sum_{n=1}^{N_{\mathrm{eff}}} K_n^2 g_\sigma(\hbar\omega_n - \hbar\omega), \tag{2.87}$$

where g_σ is a Gaussian function with width σ. The approximation uses

N_{eff} effective vibrations, each characterized by a frequency ω_n and an associated vibronic coupling strength K_n^2. The parameters K_n^2, ω_n, and σ are optimized to ensure that $K_{\text{eff}}^2(\hbar\omega)$ accurately reproduces $K^2(\hbar\omega)$. By systematically increasing the number of effective modes, we can monitor the convergence of the computed observable, which in this thesis, is the optical lineshape of the transition involving a JT-active electronic state. In practice, convergence is typically achieved with only a few effective modes, thereby significantly reducing the computational burden.

2.5. Vibrational broadening of optical spectra

2.5.1. Optical lineshapes for non-degenerate states

In the Franck–Condon approximation, the normalized lineshape $L(\hbar\omega)$ for luminescence and absorption at zero temperature ($T = 0$ K) is given by [34]:

$$L(\hbar\omega) = C\omega^{\kappa} A(\hbar\omega), \tag{2.88}$$

where C is a normalization constant, $A(\hbar\omega)$ represents the phonon spectral function, and the exponent κ takes value of 3 for luminescence and 1 for absorption. The spectral function is expressed as

$$A(\hbar\omega) = \sum_m \left|\langle \chi_{i;0} | \chi_{f;m} \rangle\right|^2 \delta\left(E_{\text{ZPL}} \mp (\varepsilon_{fm} - \varepsilon_{f0}) - \hbar\omega\right), \tag{2.89}$$

where E_{ZPL} is the zero-phonon line (ZPL) energy, and $\chi_{i;0}$ and $\chi_{f;m}$ denote the vibrational wave functions of the initial and final electronic states, respectively. Here, ε_{fm} is the energy of the m-th vibrational state in the final electronic manifold with respect to the potential energy minima. The minus and plus signs in the argument of the δ-function correspond to luminescence and absorption, respectively. The optical spectral function $A(\hbar\omega)$ quantifies the transition amplitudes between vibrational states and is central in determining the lineshape.

Since the vibrational structures of the ground and excited states typically differ, the overlap integrals $\langle \chi_{i;0} | \chi_{f;m} \rangle$ in Eq. (2.89) are inherently multidimensional. Given the large number of vibrational modes present in defect systems, the direct evaluation of these integrals becomes computationally infeasible. In a practical approach, to simplify the calculation of the overlap integrals, we adopt the equal-mode approximation from Ref. [34, 78], which assumes that the shapes and frequencies of vibrational modes of the initial and final states are identical. To address the limitations of this assumption, we follow Ref. [34] and for lineshape calculations consistently employ the vibrational modes of the final state.

The spectral function $A(\hbar\omega)$ can be can be efficiently obtained by computing it in the time domain through the generating function method of Kubo and Lax [79, 80]. In this approach, the spectral function is obtained from the generating function $G(t)$ via the relation

$$A(\hbar\omega) = \frac{1}{2\pi} \int_{-\infty}^{\infty} G(t) e^{-\gamma|t|} e^{-i(E_{\mathrm{ZPL}}/\hbar - \omega)t} \mathrm{d}t, \tag{2.90}$$

The term $e^{-\gamma|t|}$ is introduced as a phenomenological correction to account for the homogeneous Lorentzian broadening of the ZPL not captured by the theory, as well as to address inhomogeneous broadening. In practice, parameter γ is adjusted to match the experimental linewidth of the ZPL.

In the equal mode approximation, the generating function $G(t)$ can be expressed as:

$$G(t) = \exp\left[-S_{\mathrm{tot}} + \sum_k S_k e^{\pm i\omega_k t} \right], \tag{2.91}$$

where the plus sign in the exponent is used for luminescence and the minus sign for absorption, S_k represents the partial Huang–Rhys (HR) factor, and the summation runs over all vibrational modes of the system. Their sum gives the total coupling strength $S_{\mathrm{tot}} = \sum_k S_k$. The factor S_k quantifies the average number of excited phonons during an optical transition [81]. It is defined as

$$S_k = \frac{\omega_k \Delta Q_k^2}{2\hbar}, \tag{2.92}$$

where ΔQ_k represents the ionic displacement along the normal mode k induced by an optical transition. Specifically, ΔQ_k is the projection of the mass-weighted displacement between the ground and excited states onto the normalized phonon mode $\boldsymbol{\eta}_k$:

$$\Delta Q_k = \sum_{m\alpha} \sqrt{M_m} \Delta R_{m\alpha} \eta_{k;m\alpha}. \tag{2.93}$$

Here, $\Delta R_{m\alpha}$ is the displacement of the atom m along the α coordinate, and M_m is its mass.

To effectively describe the generating function (2.91) in extended systems, where a continuum of vibrational frequencies is expected, we introduce the spectral density of electron–phonon coupling (also known as the spectral function of electron–phonon coupling):

$$S(\hbar\omega) \equiv \sum_k S_k \delta(\hbar\omega_k - \hbar\omega), \tag{2.94}$$

which allows us to rewrite the generating function as follows:

$$G(t) = \exp\left[-S_{\text{tot}} + \int S(\hbar\omega) e^{\pm i\omega t}\,\mathrm{d}\omega\right]. \tag{2.95}$$

Here, $S_{\text{tot}} = \sum_k S_k$ is the total HR factor, where the sum is evaluated over all vibrational modes of the defect system. We employ smoothing functions tailored to different mode types to approximate the δ-functions in Eq. (2.94). For bulk-like and quasi-localized modes, δ-functions are replaced with Gaussians of specified width, which allows controlled spectral broadening.

2.5.2. Optical lineshapes for A to E transitions

The phonon spectral function $A(\hbar\omega)$ in Eq. (2.88), which describes transitions of $A \to E$ (from a singlet initial state to a doublet final state), can be formulated as a convolution of the spectral contributions arising from symmetry-preserving and symmetry-breaking vibrational modes [34]:

$$A(\hbar\omega) = \int A_a(\hbar\omega - \hbar\omega') A_e(\hbar\omega') \mathrm{d}(\hbar\omega'). \tag{2.96}$$

Here, $A_a(\hbar\omega)$ and $A_e(\hbar\omega)$ denote the spectral functions associated with the symmetry-preserving and symmetry-breaking vibrational modes, respectively. The function $A_a(\hbar\omega)$ encompasses vibrational modes of a_1 (or a_{1g}) symmetry, which are collectively denoted as a for consistency across systems sharing similar symmetry. This spectral function is obtained using the formalism developed for the adiabatic case, as presented in Eqs. (2.89)–(2.95).

$A_e(\hbar\omega)$ characterizes the vibrational modes associated with JT-active e-symmetry motions. For a transition in which the initial electronic state (i) is non-degenerate and the final state (f) forms a degenerate orbital doublet, the spectral function for the JT-active e vibrational modes is given by [34]:

$$A_e(\hbar\omega) = \sum_m \left[\left| \left\langle \chi^e_{i;0} \middle| \chi^{e;x}_{f;m} \right\rangle \right|^2 + \left| \left\langle \chi^e_{i;0} \middle| \chi^{e;y}_{f;m} \right\rangle \right|^2 \right] \delta(\varepsilon^e_{fm} - \varepsilon^e_{f0} - \hbar\omega). \tag{2.97}$$

Here, $\chi^e_{i;0}$ denotes the harmonic vibrational wavefunction corresponding to the e-symmetry motion of the initial state, while $\chi^{e;x}_{f;m}$ and $\chi^{e;y}_{f;m}$ represent the ionic prefactors of the vibronic wavefunction for the final degenerate state, as introduced in Eq. (2.67). Evaluating this spectral function requires computing the overlap between the harmonic wavefunctions and the ionic components of the vibronic solution, which, in turn, necessitates an explicit solution of the Jahn–Teller Hamiltonian as detailed in Sec. 2.4.

In the circular basis, the bracketed term in Eq. (2.97) can be expressed as

$$|\langle \chi^{e;+}_{f;m} | \chi^e_{i;0} \rangle|^2 + |\langle \chi^{e;-}_{f;m} | \chi^e_{i;0} \rangle|^2. \tag{2.98}$$

To calculate these overlap integrals for e-symmetry vibrational modes, similarly to a modes, we use the equal-mode approximation, which assumes that the vibrational shapes and frequencies of the A orbital manifold are well-represented by the zero-order Hamiltonian of the final state [Eq. (2.68)]. Furthermore, in the zero-temperature limit, these overlaps are calculated between the zero-phonon state of the initial state manifold, denoted as $\chi^e_{i;0} = |00\cdots 0\rangle$, and all vibronic states of the E manifold. Given that $\sum_k l_k$ is conserved, only vibronic solutions where $j = \pm 1/2$ (with $j_{\text{el}} = \pm 1/2$ and $\sum_k l_k = 0$) are relevant for this analysis.

2.6. Embedding methodology

The evaluation of the geometry relaxation profile following an optical transition is a critical aspect of supercell-based calculations. While modern DFT calculations can handle supercells with more than 1000 atoms, these sizes, although sufficient for total energy convergence, are insufficient to fully capture the influence of low-energy acoustic phonons. This limitation arises due to the constraints imposed by periodic boundary conditions and the finite number of vibrational degrees of freedom available in such supercells. Consequently, the supercell dimensions are

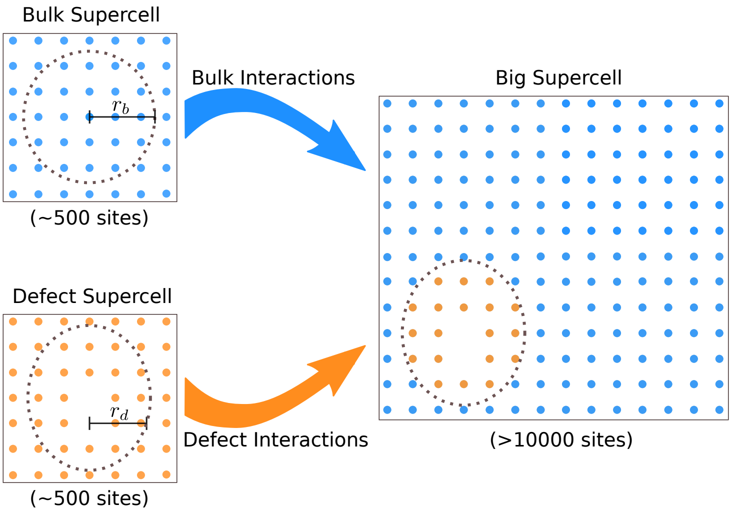

Figure 2.4: Illustration of the force constant matrix embedding methodology for defect vibrational structure calculations.

inadequate for accurately accounting for contributions from the long-wavelength components of $\Delta R_{m\alpha}$ in Eq. (2.93).

To address the limitations imposed by finite supercell sizes, we employ the force constant embedding methodology outlined in Refs. [34,82]. The embedding methodology leverages the short-range nature of interatomic interactions in semiconductors. When an atom is displaced from its equilibrium position, as performed in the finite-difference approach, the resulting force exerted on neighboring atoms diminishes rapidly with increasing distance from the displaced atom. This rapid decay facilitates allows for the efficient construction of the Hessian matrix for large supercells.

The construction of the Hessian matrix follows the criteria below:

- If two atoms lie within a specified cutoff radius r_b, the corresponding elements from the bulk supercell Hessian matrix are utilized.
- For atom pairs within a cutoff radius r_d from the defect, matrix elements from the defect-containing supercell are applied.
- In all other cases, the matrix elements are set to zero.

This force constant embedding scheme is illustrated in Fig. 2.4.

Using the force constant embedding methodology we calculate ΔQ_k for each vibrational mode of a large supercell by using forces and the harmonic relation to displacements. The relaxation component ΔQ_k is then evaluated as

$$\Delta Q_k = \frac{1}{\omega_k^2} \sum_{m\alpha} \frac{F_{m\alpha}}{\sqrt{M_m}} \eta_{k;m\alpha}, \tag{2.99}$$

where $F_{m\alpha}$ represents the force on atom m along direction α when the system is in the final electronic state but remains in the equilibrium geometry of the initial state calculated in the directly accessible supercell.

Although the embedding procedure is relatively simple, it necessitates additional corrections to account for the symmetry properties of the Hessian matrix. Specifically, truncating matrix elements beyond a predefined cutoff radius violates Newton's third law:

$$\Phi_{ni;nj} = -\sum_{m \neq n} \Phi_{mi;nj}. \tag{2.100}$$

This violation of the "acoustic sum rule" can result in a small net force acting on the entire system, potentially influencing the accuracy of low-frequency acoustic modes. To enforce Newton's third law, one approach is to redefine each matrix element $\Phi_{ni;nj}$ (for diagonal atomic indices n) using the right-hand side of Eq. (2.100). However, applying this correction when $i \neq j$ may disrupt the intrinsic symmetry of the Hessian matrix, particularly when $n = m$. To preserve the symmetry properties of the Hessian matrix and ensure that the acoustic mode frequencies at the Γ point remain zero, the correction is applied to $\Phi_{ni;nj}$ only when the Cartesian components coincide, i.e., when $i = j$.

The embedding methodology is employed to analyze the convergence of the optical lineshape with respect to supercell size. As the supercell size increases, the relaxation profile approaches the dilute limit, capturing contributions from low-frequency phonon modes and potential quasi-localized defect vibrations in resonance with bulk vibrational modes. In most cases, convergence is achieved for supercells containing more than 10 000 atoms.

Chapter 3

Benchmarking of SCAN density functional for bulk properties and thermodynamic and electronic properties of point defects

3.1. Introduction

Over recent decades, Kohn–Sham density functional theory (DFT) [28] has emerged as the principal tool for exploring atomic and electronic structures in solids. While theoretically exact, DFT relies on approximations for the exchange-correlation energy due to the unknown precise form of this contribution. Commonly used approximations include semilocal functionals like the generalized-gradient approximation (GGA), most notably the Perdew-Burke-Ernzerhof (PBE) functional [29], and hybrid functionals incorporating fractions of Fock exchange, such as PBE0 [83, 84] and screened Heyd-Scuseria-Ernzerhof (HSE) [30,85]. However, GGA functionals typically underestimate semiconductor and insulator band gaps [28,31], while hybrid functionals improve electronic structure descriptions but are computationally demanding [32–34, 86–88].

In 2015, the SCAN (Strongly-Constrained and Appropriately-Normed) functional was introduced [35] as part of the meta-GGA class functionals, offering notable improvements in the calculation of lattice parameters and energetics for solids [36]. SCAN also partially improves the common underestimation of band gaps observed with GGA functionals [37]. Its computational efficiency makes it particularly advantageous for supercell calculations of point defects [38], which are essential for accurately modeling defects in semiconductors and insulators. While SCAN has been widely applied to study bulk materials [39], its use in defect modeling has been more limited [40–42].

In this chapter, we benchmark the SCAN functional along with its two variants, rSCAN [44] and r^{2}SCAN [45], for diamond, silicon carbide, and silicon, as well as for color centers in these materials, to evaluate the performance of these functionals in predicting both bulk and defect properties. The primary focus is to assess their accuracy in comparison with the standard PBE and hybrid HSE06 functionals, considering both computational cost and predictive capabilities.

The chapter is structured as follows. In Section 3.3.1, we present the calculated bulk lattice parameters for diamond, silicon carbide polytypes, and silicon using the SCAN family of functionals. We discuss the accuracy of these functionals in predicting lattice constants, bulk moduli, and band gaps. Section 3.3.4 details the atomic structures of the studied point defects, including the NV$^-$ and split-vacancy centers in diamond, as well as neutral divacancies in 4H-SiC. Section 3.3.6 reports the calculated defect formation energies, highlighting differences across functionals. Section 3.3.7 covers the computed charge-state transition levels (CTLs) for selected defects, aligned to a common reference for comparison. In Section 3.3.8, we compare the calculated zero-phonon line (ZPL) energies with available experimental values, demonstrating the accuracy of the SCAN family in predicting defect excitation energies. Section 3.3.10 discusses the zero-field splitting (ZFS) calculations for divacancy defects in 4H-SiC, comparing theoretical predictions with experimental measurements to evaluate the performance of different functionals. Finally, in Section 3.4, we summarize the key findings of this chapter and present the main statements supporting the thesis defense.

3.2. Methodology

3.2.1. Computational details

Calculations were performed using spin-polarized density functional theory (DFT) with a plane-wave energy cutoff of 600 eV for diamond and silicon carbide polytypes, and 500 eV for silicon, as implemented in the Vienna Ab Initio Simulation Package (VASP) [63]. The functionals employed were PBE, SCAN, rSCAN, r^{2}SCAN, and HSE06, with a screened Fock exchange fraction of $a = 0.25$ [30]. All defects were modeled using the supercell approach [89]. Brillouin zone sampling was carried out using a single $\mathbf{k}$-point at Γ. The convergence criterion for the electronic self-consistent loop was set to 10^{-6} eV for the HSE06 functional, whereas a criterion of 10^{-8} eV was applied for all other functionals. The ionic relaxation was terminated when the forces on atoms fell below 10^{-4} eV Å^{-1}.

3.2.2. Defect formation energies

The thermodynamic stability and concentration of defects can be assessed by calculating the defect formation energies which represent the energy required to create a defect in a solid. The formation energies of defects in a charge state q were calculated using the expression [89]:

$$\Delta H_{\mathrm{f}}(q) = E_{\mathrm{tot}}(q) - E_{\mathrm{bulk}} - \sum_i n_i \mu_i + q(E_{\mathrm{VBM}} + E_{\mathrm{F}}) + E_{\mathrm{corr}}. \quad (3.1)$$

In this equation, $E_{\mathrm{tot}}(q)$ denotes the total energy of the supercell containing the defect in charge state q, while E_{bulk} is the total energy of the pristine, defect-free supercell. The term μ_i represents the chemical potential of atom type i, with n_i indicating the number of atoms of type i that are added to ($n_i > 0$) or removed from ($n_i < 0$) the supercell to form the defect. For defects in diamond μ_{C} is equal to the energy of diamond per one carbon atom. μ_{Si}, μ_{Ge}, and μ_{Sn} are equal to the energy of Si, Ge, and Sn elemental solids per one atom, and μ_{N} is equal to $1/2E_{\mathrm{tot}}(\mathrm{N}_2)$. For calculating the formation energy of the C-center in silicon, μ_{C} is derived from bulk diamond, while μ_{O} corresponds to the energy per oxygen atom in quartz (SiO_2).

The Fermi energy, E_{F}, is referenced relative to the valence band maximum (VBM) E_{VBM} as determined for each functional. An additional term, E_{corr}, is included to correct for spurious electrostatic interactions between charged defects in the periodically repeated supercell, as described in Ref. [90]. The Fermi energy at which the formation energies of charge states q and q' are equal is known as the charge-state transition level (CTL), denoted as $\varepsilon(q/q')$ [89]. The CTL is a parameter for identifying the stability regions of different charge states concerning the electron chemical potential. Its position relative to the band edges is an important characteristic of a defect, as it largely dictates the defect's impact on the electronic and optical properties of the system. The CTL is given by:

$$\varepsilon(q/q') = \frac{\Delta H_{\mathrm{f}}(q; E_{\mathrm{F}} = 0) - \Delta H_{\mathrm{f}}(q'; E_{\mathrm{F}} = 0)}{q' - q}. \tag{3.2}$$

This transition level, $\varepsilon(q/q')$, is also referenced to the VBM. To facilitate comparison across different functionals, charge-state transition levels are typically referenced to a common benchmark, such as the average electrostatic potential or the vacuum level [91–93]. As a benchmark for band structure alignment across functionals, we determined the position of VBMs relative to the vacuum level using surface calculations in diamond. These calculations used (001) surfaces, modeled as 20-layer slabs, and included the (2×1) reconstruction of the (001) surface, calculated at the PBE level. For calculations with the SCAN family and HSE06 functionals, the bulk lattice constant was adjusted to the equilibrium value specific to each functional.

3.2.3. Zero-phonon line energy

Zero-phonon line (ZPL) energies were calculated using the ΔSCF (delta-self-consistent-field) approximation, a widely used method for determining defect excitation energies in solids [94–102]. In the ΔSCF approach, excited states are modeled by modifying the occupancies of defect-localized Kohn–Sham orbitals, whereby an electron is promoted from an occupied localized orbital to a selected unoccupied orbital, yielding a wavefunction that represents the excited state. Although ΔSCF relies on constrained orbital occupations based on chemical intuition, it has a theoretical basis: Gunnarsson and Lundqvist [103] demonstrated that DFT can extend to excited states by imposing symmetry constraints on the exchange-correlation functional. However, because a general prescription for achieving this at the functional level is unavailable, the same functional is typically applied to both ground and excited states. The ΔSCF approach thus serves as a practical method, enforcing symmetry in defect wavefunctions and capturing ZPL energies.

For the NV^- center in diamond and neutral axial divacancies (hh-VV^0 and kk-VV^0) in 4H-SiC, the ZPL energy was calculated as an energy difference between the ground triplet state $^3A_2$ with an electronic configuration of $a_1^2e^2$ and the excited triplet state ^3E with a_1e^3 electronic configuration in distorted C_{1h} symmetry due to the Jahn–Teller

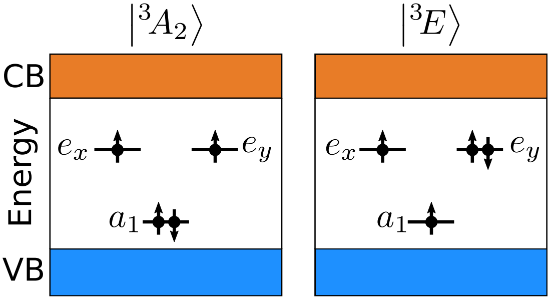

Figure 3.1: Defect-level diagrams of the NV$^-$ center in diamond. Diagrams show Kohn–Sham single-particle configurations showing the occupancy of these levels for the ground state $^3A_2$ on the left and excited state ^3E on the right. Shaded areas correspond to the valence band (VB) and the conduction band (CB).

effect present in the excited triplet state (see Figs. 3.1 and 3.5). This was achieved by promoting the a_1 electron in the spin-minority channel to the e level and allowing the symmetry to break (from C_{3v} to C_{1h}) during the calculation. Similarly, the excited doublet states ^2E_u of SiV$^-$, GeV$^-$, and SnV$^-$ centers were modeled by promoting an e_u electron in the spin-minority channel to an empty e_g orbital (see Fig. 3.7a). For these negatively charged group-IV vacancies, the Jahn–Teller effect is present in both ground and excited states, so ZPL energies were calculated as the energy difference between the ^2E_g and ^2E_u states with broken symmetry (from D_{3d} to C_{2h}).

For the basal divacancy hk-VV^0, the ZPL energy was determined as the energy difference between the ground triplet state $^3A''$ with a single-determinant wavefunction $|a'(1)\bar{a}'(1)a''a'(2)|$ and the excited triplet state $^3A'$, with a single-determinant wavefunction $|a'(1)a''\bar{a}''a'(2)|$ (see Fig. 3.6a). In this case, there is no symmetry breaking, and the defect remains in C_{1h} symmetry in both ground and excited states. For the kh-VV^0 divacancy, the ZPL energy was calculated as the energy difference between the ground triplet state $^3A''$ and the excited triplet state ^3A in distorted C_1 symmetry due to the pseudo Jahn–Teller effect (see Fig. 3.6b).

3.2.4. Zero-field splitting

If a point defect possesses two or more unpaired electrons, its electronic spin levels experience splitting even in the absence of an external magnetic field. This effect, known as zero-field splitting, arises predominantly due to the dipole-dipole interaction between electron spins, expressed as [104]:

$$\hat{\mathbf{S}}^T \mathbf{D} \hat{\mathbf{S}} = \frac{\mu_0}{4\pi} g_e^2 \mu_B^2 \left(\frac{3(\hat{\mathbf{S}}_i \cdot \mathbf{r})(\hat{\mathbf{S}}_j \cdot \mathbf{r}) - r^2 (\hat{\mathbf{S}}_i \cdot \hat{\mathbf{S}}_j)}{r^5} \right). \tag{3.3}$$

Here, $\mathbf{r}$ represents the displacement vector between the two spins, while $\hat{\mathbf{S}}_i$ and $\hat{\mathbf{S}}_j$ denote the spin operators. In DFT, the dipole-dipole interaction tensor $\mathbf{D}$ is commonly approximated using the square of the Slater determinant formed by KS orbitals (see Section 2.2.2), such that the wavefunction for a pairwise spin interaction is given by:

$$|\zeta_{i,j}(\mathbf{r}_1, \mathbf{r}_2)|^2 = \frac{1}{2} |\phi_i^{\mathrm{KS}}(\mathbf{r}_1) \phi_j^{\mathrm{KS}}(\mathbf{r}_2) - \phi_i^{\mathrm{KS}}(\mathbf{r}_2) \phi_j^{\mathrm{KS}}(\mathbf{r}_1)|^2. \tag{3.4}$$

The matrix elements of the zero-field splitting tensor are then computed as:

$$D_{ab} = \frac{1}{2} \frac{\mu_0}{4\pi} \frac{g_e^2 \mu_B^2}{S(2S-1)} \sum_{i<j} \chi_{ij} \int\int |\zeta_{i,j}(\mathbf{r}_1, \mathbf{r}_2)|^2 \left(\frac{3r_a r_b - r^2 \delta_{ab}}{r^5} \right) \mathrm{d}\mathbf{r}_1 \, \mathrm{d}\mathbf{r}_2. \tag{3.5}$$

Here, χ_{ij} takes values of ±1, depending on whether the interacting spins are parallel or antiparallel. The authors of Ref. [105] initially implemented this equation in a stand-alone code using the pseudo part of the KS orbitals, which accounts for 95% of the total contribution. Later, the full calculation, including the core regions, was incorporated into VASP code.

3.2.5. Vertical excitation energies

The vertical excitation energies for negatively charged group-IV vacancy centers were computed using distorted ground-state configurations with C_{2h} symmetry. For the NV$^-$ center, direct convergence of the excited degenerate ^{3}E state posed challenges due to the degeneracy inherent in the high-symmetry geometric configuration, so vertical excitation energies were estimated indirectly, as follows. The vibrational structure of the excited state was calculated by using equal (half-half) occupations with an electronic configuration of $a_1 e_x^{1.5} e_y^{1.5}$ for the two degenerate orbitals [34]. Partial Huang-Rhys factors S_k were determined for modes with a_1 symmetry, and dimensionless vibronic constants K_k were calculated for degenerate e symmetry modes [34]. Assuming a harmonic approximation for a_1 modes and a linear $E \otimes e$ Jahn–Teller interaction, the vertical excitation energy is given by:

$$E_{\mathrm{VE}} = E_{\mathrm{ZPL}} + E_{\mathrm{rel}} = E_{\mathrm{ZPL}} + \sum_{k \in a_1} S_k \hbar \omega_k + \sum_{k \in e} K_k^2 \hbar \omega_k. \tag{3.6}$$

In this expression, E_{ZPL} denotes the zero-phonon line energy, E_{rel} is the ionic relaxation energy, and ω_k represents the vibrational frequencies of the defect. The summation $k \in e$ spans the doublets of degenerate modes. The relaxation energy contribution from e symmetry vibrational modes corresponds to the Jahn–Teller relaxation energy [106].

3.3. Results and discussion

3.3.1. Bulk lattice parameters

First, we evaluate the performance of various exchange-correlation functionals in predicting the bulk parameters of diamond, with the results summarized in Table 3.1. Regarding the lattice constant a, PBE provides a value that is 0.14% larger than the experimental value of $a = 3.567$ Å, which initially might suggest strong correspondance. However, HSE06 and SCAN slightly underestimate a by 0.59% and 0.36%, respectively. It is worth noting, as pointed out in Ref. [107], that experimental equilibrium lattice constants include contributions from the anharmonicity of zero-point vibrations. This effect should be considered for accurate comparison with theoretical results. The corrected experimental value is $a = 3.555$ Å [107], as also given in Table 3.1. With this correction, both SCAN and rSCAN show excellent agreement with the experimental value, deviating by only 0.03%. By contrast, PBE overestimates a by 0.48%, while HSE06 underestimates it by 0.25%.

To determine the bulk modulus, pressures as a function of the lattice constant were fitted to the universal equation of state [108]. Regarding the bulk modulus B, the rSCAN and r^{2}SCAN functionals yield the closest agreement with experiment, overestimating B by 2.24% and 1.35%,

Table 3.1: Lattice constants a (Å), bulk moduli B (GPa), derivatives α, and band gaps E_g (eV) for diamond. ΔE_{VBM} and ΔE_{CBM} are shifts in the absolute positions of bulk band edges with respect to HSE06 values.

	a	B	α	E_g	ΔE_{VBM}	ΔE_{CBM}
PBE	3.572	435	3.7	4.120	0.59	-0.63
SCAN	3.554	460	3.7	4.558	0.37	-0.41
rSCAN	3.556	456	3.7	4.375	0.40	-0.56
$\mathrm{r^2SCAN}$	3.561	452	3.7	4.331	0.47	-0.54
HSE06	3.546	473	3.6	5.343	0	0
Expt.	3.567[a] (3.555[b])	446[c]	3.7	5.48[a]	–	–

[a] Ref. [109] [b] Ref. [107] [c] Ref. [110]

respectively. In contrast, PBE underestimates B by 2.47%, while HSE06 overestimates it by 6.05%. For the derivative α, all functionals match the experimental value closely, as shown in Table 3.1.

Next, we investigate the bulk parameters of several polytypes of silicon carbide. For silicon carbide, lattice constants for the 3C, 4H, and 6H polytypes are summarized in Table 3.2. For 3C-SiC, PBE overestimates the lattice constant a by 0.44% relative to the experimental value of $a = 4.360$ Å, while HSE06 slightly underestimates it by 0.34%. The SCAN and rSCAN functionals yield deviations of 0.21% and 0.28%, respectively, showing close agreement with experimental data. Notably, $\mathrm{r^2SCAN}$ provides the smallest deviation, underestimating a by only 0.14%, making it the most accurate functional for 3C-SiC.

For the 4H-SiC polytype, the a and c lattice parameters are well-predicted by the SCAN family of functionals. SCAN and $\mathrm{r^2SCAN}$ show very small deviations from experiment, at just 0.19% and 0.13% for a, and 0.17% and 0.11% for c, respectively. The rSCAN functional performs slightly less accurately with deviations of 0.26% for a and 0.26% for c, but still closely aligns with experimental values. PBE overestimates both a and c, resulting in deviations of 0.42% and 0.44%, respectively. HSE06 provides a relatively accurate result for a, with a small deviation of 0.32%, but underestimates c with a deviation of 0.34%.

For the 6H-SiC polytype, $\mathrm{r^2SCAN}$ again shows strong performance, deviating by only 0.13% for a and 0.11% for c, closely matching the experimental values. SCAN follows with deviations of 0.19% for a and 0.17% for c, providing a slightly less accurate but still reliable prediction.

Table 3.2: Lattice constants a and c (Å) and band gaps E_g (eV) for various SiC polytypes.

	3C-SiC		4H-SiC			6H-SiC		
	a	E_g	a	c	E_g	a	c	E_g
PBE	4.379	1.370	3.093	10.126	2.223	3.094	15.182	2.029
SCAN	4.351	1.708	3.074	10.065	2.596	3.075	15.089	2.385
rSCAN	4.348	1.744	3.072	10.056	2.632	3.072	15.076	2.419
r^{2}SCAN	4.354	1.724	3.076	10.071	2.611	3.077	15.099	2.399
HSE06	4.345	2.247	3.070	10.048	3.172	3.071	15.066	2.941
Expt.	4.360[a]	2.390[b]	3.080[a]	10.082[a]	3.265[b]	3.081[a]	15.115[a]	3.023[b]

[a] Ref. [111] [b] Ref. [112]

Table 3.3: Lattice constants a (Å) and band gaps E_g (eV) for silicon.

	a	E_g
PBE	5.469	0.611
SCAN	5.428	0.825
rSCAN	5.435	0.776
r^{2}SCAN	5.440	0.782
HSE06	5.433	1.153
Expt.	5.419[a]	1.170[b]

[a] Ref. [113] [b] Ref. [114]

The rSCAN functional produces deviations of 0.29% for a and 0.26% for c, which are slightly larger. PBE overestimates both parameters, resulting in deviations of 0.42% for a and 0.44% for c. HSE06 slightly underestimates both parameters, especially c, with deviations of 0.32% for a and 0.32% for c.

Finally, we investigated the bulk parameters of silicon, with the results summarized in Table 3.3. For silicon, PBE overestimates the lattice constant a by 0.92% relative to the experimental value of $a = 5.419$ Å, while HSE06 slightly overestimates it by 0.26%. The SCAN functional provides the closest agreement, underestimating a by only 0.17%, making it the most accurate functional for predicting the lattice constant of silicon. The rSCAN and r^{2}SCAN functionals also show good agreement, with deviations of 0.30% and 0.39%, respectively, showing improved accuracy over PBE.

3.3.2. Bulk electronic structure

For diamond, the electronic band gap E_g shows significant variation across the different functionals used, as displayed in Table 3.1. Consistent with expectations for semilocal functionals, the PBE band gap of 4.12 eV underestimates the experimental value of 5.48 eV. In contrast, the SCAN functional improves upon PBE by increasing the band gap by 0.44 eV, while rSCAN and r^{2}SCAN provide smaller increases of 0.26 eV and 0.21 eV, respectively. HSE06 achieves a band gap of 5.34 eV, aligning most closely with the experimental result.

Beyond band gap values, the absolute positions of the valence band maximum (VBM) and conduction band minimum (CBM), are also impacted by the choice of functional. These band edge positions are important for aligning charge-state transition levels (CTLs) of defects as obtained by different methods [91–93]. The shifts in the VBM and CBM (ΔE_{VBM} and ΔE_{CBM}) relative to the HSE06 band edge positions are listed in Table 3.1. Compared with HSE06, semilocal functionals generally show a near-symmetrical band gap reduction. Prior studies on PBE and HSE06 alignment, such as Refs. [115, 116], support these findings. For ΔE_{VBM}, our calculated value of 0.59 eV aligns closely with the previously reported values of 0.59 eV [115] and 0.63 eV [116].

The calculated electronic band gaps E_g for various SiC polytypes are summarized in Table 3.2. For the 3C-SiC polytype, the PBE functional underestimates the band gap, yielding 1.370 eV compared to the experimental value of 2.390 eV. The SCAN, rSCAN, and r^{2}SCAN functionals improve upon PBE, with values of 1.708 eV, 1.744 eV, and 1.724 eV, respectively. However, the HSE06 functional offers the most accurate prediction, yielding a band gap of 2.247 eV, which is closer to the experimental value but still slightly underestimated.

For the 4H-SiC polytype, a similar trend is observed. The PBE functional predicts a band gap of 2.223 eV, significantly lower than the experimental value of 3.265 eV. The SCAN, rSCAN, and r^{2}SCAN functionals show gradual improvement, with values of 2.596 eV, 2.632 eV, and 2.611 eV, respectively. HSE06 again provides the closest agreement with experiment, predicting a band gap of 3.172 eV, which is slightly below the experimental value.

In the case of the 6H-SiC polytype, the trend remains consistent. The PBE functional underestimates the band gap at 2.029 eV compared

Table 3.4: LO phonon frequencies (meV) at high-symmetry points for diamond. Experimental data from Ref. [118].

	Γ	X	L
PBE	160.7	148.1	154.6
SCAN	167.0	153.2	160.4
rSCAN	165.0	152.5	159.6
r^2SCAN	164.7	152.0	159.0
HSE06	171.0	154.7	160.8
Expt. INS	164.0	151.3	157.0

to the experimental value of 3.023 eV. The SCAN functional yields an improved value of 2.385 eV, followed by rSCAN and r^2SCAN with band gaps of 2.419 eV and 2.399 eV, respectively. HSE06 again provides the most accurate result, predicting a band gap of 2.941 eV, which closely matches the experimental value.

For bulk silicon, the electronic band gap E_g varies significantly depending on the functional, as shown in Table 3.3. Similar to trends observed in bulk diamond, the PBE functional significantly underestimates the band gap, yielding 0.611 eV compared to the experimental value of 1.170 eV. The SCAN functional provides a better estimate with an increased band gap of 0.825 eV, improving upon PBE's result. Both rSCAN and r^2SCAN give band gap values closer to SCAN, at 0.776 eV and 0.782 eV, respectively. However, HSE06 offers the closest agreement with experiment, producing a band gap of 1.153 eV, which is only slightly below the experimental value.

3.3.3. Bulk phonons of diamond

Phonon dispersion curves for bulk diamond were computed using the finite displacement method, as implemented in the `PHONOPY` software package [117]. Calculations of interatomic force constants were performed in $4 \times 4 \times 4$ supercells (containing 512 atoms) with Brillouin zone sampling restricted to the Γ-point, and atomic displacements set to 0.01 Å. Table 3.4 presents the calculated longitudinal-optical (LO) phonon frequencies (in meV) at key high-symmetry points, along with experimental values obtained from inelastic neutron scattering (INS) [118].

Although all tested functionals yield frequencies close to the exper-

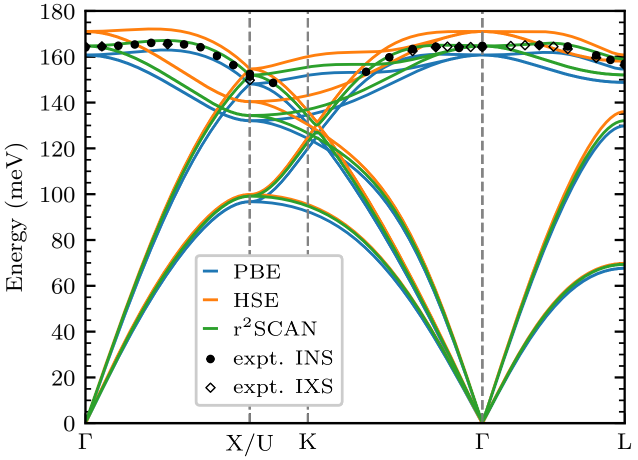

Figure 3.2: Phonon dispersion curves of diamond calculated using PBE, HSE06, and r^{2}SCAN. Experimental data from Ref. [118].

imental values, the SCAN family, especially r^{2}SCAN, shows the best agreement. Figure 3.2 illustrates the phonon dispersion curves obtained with PBE, HSE06, and r^{2}SCAN and compares them to experimental data from Ref. [118]. Consistent with Ref. [119], both PBE and HSE06 exhibit some deviation: HSE06 tends to overestimate, while PBE tends to underestimate LO phonon frequencies. The r^{2}SCAN functional, however, provides values that fall between those of PBE and HSE06, closely matching the experimental data.

3.3.4. Defect geometries

For diamond defects, a $4 \times 4 \times 4$ supercell of 512 atoms was used, where two carbon atoms were removed and replaced by an impurity atom. All neutral divacancy centers ($V_{Si}V_C^0$ or VV^0) in silicon carbide were created by removing one Si atom and one C atom from a $6 \times 6 \times 2$ supercell containing 576 atomic sites. The C-center in silicon was created within a $4 \times 4 \times 4$ supercell with 512 atoms. This C-center defect forms a square-like ring structure within the (110) crystallographic plane, consisting of two silicon atoms and two interstitial atoms positioned symmetrically. The atomic structures of selected defects are shown in Figures 3.3 and 3.4.

In diamond, the NV center (Fig. 3.3**a**) consists of a nitrogen atom adjacent to a vacancy, exhibiting C_{3v} symmetry. The SiV center

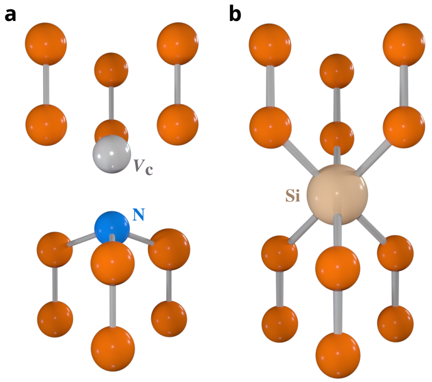

Figure 3.3: Ball-and-stick representations of atomic structures of **a** nitrogen-vacancy and **b** silicon-vacancy centers in diamond.

(Fig. 3.3**b**) features an interstitial silicon atom positioned midway between two vacancies, resulting in a split-vacancy configuration with D_{3d} symmetry. The GeV, SnV, and NiV centers in diamond have structures analogous to the SiV center.

The atomic structures of divacancy defects in 4H-SiC are illustrated in Fig. 3.4a, where carbon and silicon atoms are represented by brown and blue spheres, respectively, and vacancy pairs are depicted as hollow spheres. Four nonequivalent divacancy configurations (*hh*, *kk*, *hk*, *kh*) are shown, corresponding to the local symmetry of lattice sites by *h* (hexagonal) and *k* (cubic) planes. All axial divacancies (*hh*-VV^0 and *kk*-VV^0) are aligned along the *c*-axis of 4H-SiC, while basal divacancies (*hk*-VV^0 and *kh*-VV^0) can occur in three equivalent orientations. The ground state of neutral axial divacancies exhibits C_{3v} symmetry, whereas neutral basal divacancies exhibit C_{1h} symmetry.

The atomic structure of the C-center in silicon is shown in Fig. 3.4b. This defect exhibits C_{1h} symmetry, with its mirror plane aligning with the (110) crystallographic plane and intersecting the square-like ring formed by two silicon atoms (blue), one interstitial carbon atom (brown), and one interstitial oxygen atom (red).

3.3.5. Electronic structure of defects

The Kohn–Sham defect level diagrams of ground and excited states of NV$^-$ center in diamond is shown in Fig. 3.5a. The electronic structure arises from molecular orbitals formed by three dangling bonds of

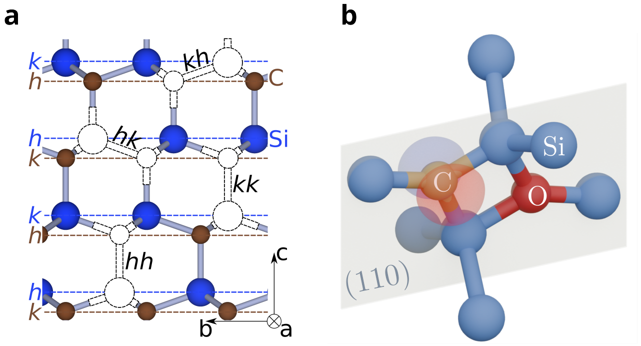
a
b
k
h
kh
C
h
k
hk
Si
kk
k
h
hh
c
h
k
b
a
Si
C
O
(110)

Figure 3.4: Ball-and-stick representations of atomic structures of **a** divacancy defects in 4H-SiC and **b** C_iO_i defect in silicon (also known as the C-center) with the (110) crystallographic plane shown.

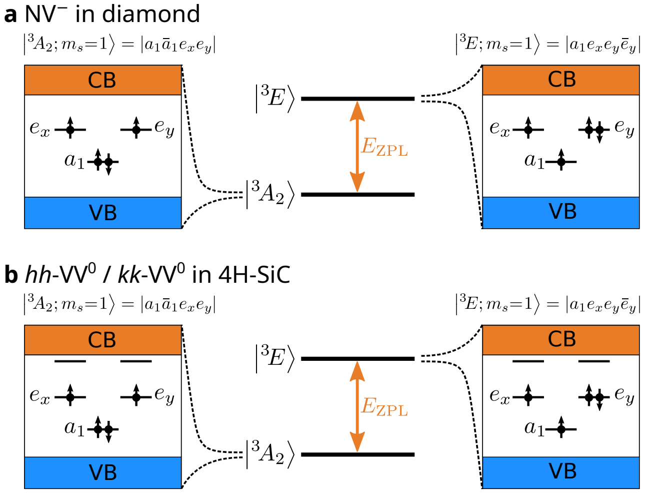
a NV⁻ in diamond
$|^3A_2; m_s{=}1\rangle = |a_1\bar{a}_1e_xe_y|$
$|^3E; m_s{=}1\rangle = |a_1e_xe_y\bar{e}_y|$
CB
e_x
e_y
a_1
VB
$|^3E\rangle$
E_{ZPL}
$|^3A_2\rangle$
CB
e_x
e_y
a_1
VB
b hh-VV⁰ / kk-VV⁰ in 4H-SiC
$|^3A_2; m_s{=}1\rangle = |a_1\bar{a}_1e_xe_y|$
$|^3E; m_s{=}1\rangle = |a_1e_xe_y\bar{e}_y|$
CB
e_x
e_y
a_1
VB
$|^3E\rangle$
E_{ZPL}
$|^3A_2\rangle$
CB
e_x
e_y
a_1
VB

Figure 3.5: Defect-level diagrams of **a** NV^- center in diamond and **b** neutral axial divacancies (hh-VV^0 and kk-VV^0) in 4H-SiC. Diagrams show Kohn–Sham single-particle configurations showing the occupancy of these levels for the ground states on the left and excited states on the right. Shaded areas correspond to the valence band (VB) and the conduction band (CB).

three carbon atoms surrounding a nearby vacancy and a dangling bond from a substitutional nitrogen atom. These molecular orbitals consist of a non-degenerate a_1 orbital and a doubly-degenerate set of e orbitals. The ground state of the NV$^-$ center is a spin-triplet, denoted as $^3A_2$, with an electronic configuration of $a_1^2e^2$. For the spin projection $m_s = 1$, the wavefunction is represented as single determinant wave function $|a_1\bar{a}_1e_xe_y|$. Optical excitation promotes a spin-down electron from the a_1 orbital to an e orbital, resulting in the spin-triplet orbitally degenerate ^3E excited state with the configuration a_1e^3. For $m_s = 1$, the degenerate wave functions of this excited state corresponds to two Slater determinants: $|a_1e_xe_y\bar{e}_y|$ and $|a_1\bar{e}_xe_xe_y|$.

Figure 3.5b illustrates the defect-level diagrams for the ground and excited states of axial divacancies in 4H-SiC (hh-VV^0 and kk-VV^0), which closely resemble those of the NV$^-$ center. The electronic configurations originate from the molecular orbitals formed by carbon dangling bonds, resulting in three principal orbitals: a non-degenerate a_1 orbital and a pair of degenerate e orbitals. DFT calculations also predict the presence of an additional e-symmetric doublet derived from silicon dangling bonds near the conduction band edge, though these states are not optically active under standard excitation conditions. In their neutral charge state, axial divacancies have a spin-triplet ground state, designated as $^3A_2$, with an orbital occupation of $a_1^2e^2$ and the corresponding wavefunction can be written as $|a_1\bar{a}_1e_xe_y|$. Optical excitation transfers a spin-down electron from the a_1 orbital to an e orbital, creating the spin-triplet ^3E excited state with the orbital configuration a_1e^3. This excited state is represented by two distinct Slater determinants: $|a_1e_xe_y\bar{e}_y|$ and $|a_1\bar{e}_xe_xe_y|$.

The electronic structure of ground and excited states of neutral basal divacancies (hk-VV^0 and kh-VV^0) are illustrated in Fig. 3.6. In their ground states, these basal divacancies exhibit C_{1h} symmetry, with the molecular orbitals classified into either a' or a'' irreducible representations. For the hk divacancy, the three orbitals within the band gap are, in order of increasing energy, $a'(1)$, a'', and $a'(2)$ (see Fig. 3.6a). The ground state of the hk divacancy is a triplet state, labeled $^3A''$, characterized by the electronic configuration $|a'(1)\bar{a}'(1)a''a'(2)|$. Optical excitation results in the $^3A'$ excited state, with the electronic configuration $|a'(1)a''\bar{a}''a'(2)|$, where now the a'' orbital is singly occupied. In

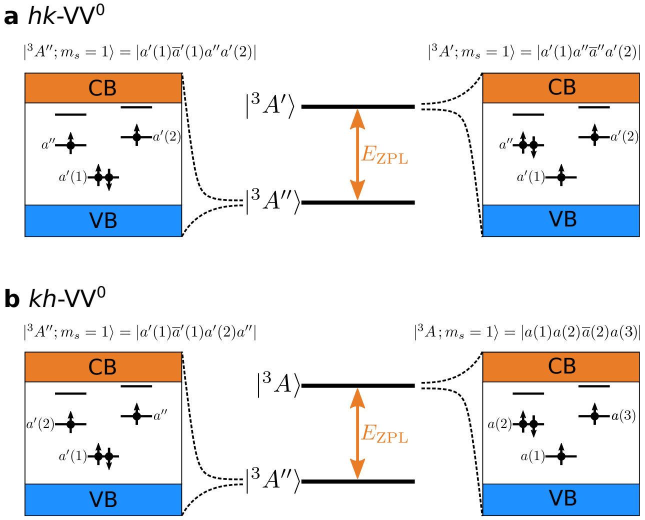
a hk-VV^0
$|^3A''; m_s=1\rangle = |a'(1)\bar{a}'(1)a''a'(2)|$
$|^3A'; m_s=1\rangle = |a'(1)a''\bar{a}''a'(2)|$
CB
VB
a''
$a'(1)$
$a'(2)$
$|^3A'\rangle$
$|^3A''\rangle$
E_{ZPL}
b kh-VV^0
$|^3A''; m_s=1\rangle = |a'(1)\bar{a}'(1)a'(2)a''|$
$|^3A; m_s=1\rangle = |a(1)a(2)\bar{a}(2)a(3)|$
$a'(2)$
a''
$a'(1)$
$a(2)$
$a(3)$
$a(1)$
$|^3A\rangle$
$|^3A''\rangle$
E_{ZPL}

Figure 3.6: Defect-level diagrams of **a** *hk*-VV^0 and **b** *kh*-VV^0 defects in 4H-SiC. Diagrams show Kohn–Sham single-particle configurations showing the occupancy of these levels for the ground states on the left and excited states on the right. Shaded areas correspond to the valence band (VB) and the conduction band (CB).

contrast, the *kh* divacancy ground state orbitals, from lowest to highest energy, are $a'(1)$, $a'(2)$, and a'' respectively (see Fig. 3.6b). The ground state of the *kh* divacancy is $^3A''$ and is represented by the electronic configuration $|a'(1)\bar{a}'(1)a'(2)a''|$. The excited state of the *kh* divacancy has C_1 symmetry, with all molecular orbitals possessing a-symmetry.

The defect-level diagrams for the ground and excited states of the negatively charged group-IV (G4V$^-$) centers in diamond are depicted in Fig. 3.7a. The ground state of the G4V$^-$ center corresponds to a spin-doublet single-determinant configuration, ^2E_g represented by the electronic configuration $|e_{ux}\bar{e}_{ux}e_{uy}\bar{e}_{uy}e_{gx}\bar{e}_{gx}e_{gy}|$. Optical excitation promotes a spin-minority electron from the e_u orbital to an unoccupied e_g orbital, resulting in an excited state ^2E_u with an electronic configuration $|e_{ux}\bar{e}_{ux}e_{uy}e_{gx}\bar{e}_{gx}e_{gy}\bar{e}_{gy}|$. For the negatively charged nickel-vacancy (NiV$^-$) center in diamond, the electronic configuration arises from the interaction of six carbon dangling bonds with the five $3d$ orbitals of the nickel atom. The electronic structures of the ground and excited states of the NiV$^-$ center are illustrated in Fig. 3.7b. The ground state is a spin-doublet with E_u symmetry, corresponding to a configuration of

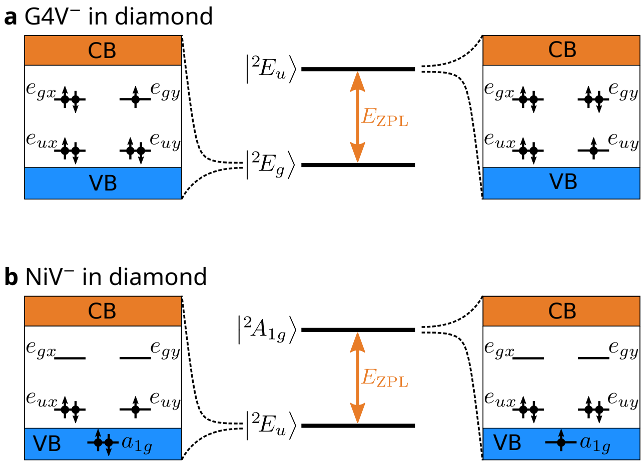
a G4V⁻ in diamond
CB
e_{gx}
e_{gy}
e_{ux}
e_{uy}
VB
$|^2E_u\rangle$
E_{ZPL}
$|^2E_g\rangle$
CB
e_{gx}
e_{gy}
e_{ux}
e_{uy}
VB
b NiV⁻ in diamond
CB
e_{gx}
e_{gy}
e_{ux}
e_{uy}
VB
a_{1g}
$|^2A_{1g}\rangle$
E_{ZPL}
$|^2E_u\rangle$
CB
e_{gx}
e_{gy}
e_{ux}
e_{uy}
VB
a_{1g}

Figure 3.7: Defect-level diagrams of **a** negatively charged group-IV vacancy (SiV^-, GeV^-, SnV^-) and **b** NiV^- centers in diamond. Diagrams show Kohn–Sham single-particle configurations showing the occupancy of these levels for the ground states on the left and excited states on the right. Shaded areas correspond to the valence band (VB) and the conduction band (CB).

^2E_u with electronic configuration $|a_{1g}\bar{a}_{1g}e_{ux}\bar{e}_{ux}e_{uy}|$. Optical excitation transfers a spin-minority electron from the a_{1g} orbital to the e_u orbital, leading to an excited state with A_{1g} symmetry and $|a_{1g}e_{ux}\bar{e}_{ux}e_{uy}\bar{e}_{uy}|$ electronic configuration.

3.3.6. Defect formation energies

Table 3.5 provides the formation energies for various charge states of NV, SiV, GeV, and SnV defects in diamond at a Fermi energy level of $E_{\mathrm{F}} = 0$. The formation energies for neutral ($q = 0$) charge states are highlighted (in bold) in Table 3.5, as these values are unaffected by the Fermi level, allowing for direct comparison across different functionals. For the NV center, the SCAN family of functionals yields formation energies in the range of 5.60–5.73 eV, lower than the PBE result of 5.89 eV and the HSE06 result of 6.22 eV.

In the case of group-IV vacancy centers, such as SiV, the SCAN family produces values between those of PBE and HSE06: PBE predicts a formation energy of 5.53 eV, SCAN variants range from 5.66 to 5.75 eV, and HSE06 gives a higher value of 6.27 eV. For certain defect types, formation energies from PBE and HSE06 have been previously reported

Table 3.5: Calculated diamond defect formation energies (in eV) at $E_{\mathrm{F}} = 0$. Neutral charge states are highlighted.

	NV				SiV				GeV				SnV				
	+	0	−	2−	+	0	−	2−	+	0	−	2−	2+	+	0	−	2−
PBE	5.13	**5.89**	7.95	12.06	5.31	**5.53**	6.70	8.71	6.95	**7.34**	8.91	11.37	9.77	9.81	**10.41**	12.31	15.09
SCAN	5.12	**5.60**	7.88	12.41	5.60	**5.75**	7.00	9.07	7.26	**7.57**	9.32	11.92	10.33	10.33	**10.84**	12.98	15.91
rSCAN	5.25	**5.73**	7.91	12.26	5.54	**5.71**	6.87	8.86	7.17	**7.49**	9.10	11.55	10.11	10.13	**10.66**	12.62	15.41
r^2SCAN	5.25	**5.69**	7.87	12.20	5.50	**5.66**	6.81	8.76	7.11	**7.43**	9.02	11.45	10.03	10.04	**10.55**	12.49	15.26
HSE06	5.39	**6.22**	8.89	13.89	6.03	**6.27**	7.77	10.14	7.54	**8.02**	10.03	12.91	10.32	10.47	**11.21**	13.60	16.82

in the literature, with our results showing close alignment (e.g., the NV center in Ref. [120] and the SiV center in Ref. [121] using HSE06).

Since defect formation energies are not directly measurable, their experimental values remain unknown. However, Table 3.5 illustrates significant variations in formation energies across functionals, with discrepancies up to 0.8 eV, much larger than the typical deviation of about 0.1 eV observed in atomization energies of small molecules [35]. This difference likely arises due to the substantial diversity in chemical environments represented in the total energy calculations involved in defect formation. For instance, the SnV center shows the largest variation, as its formation energy combines contributions from bulk diamond (a wide-bandgap insulator), the defect structure, and bulk Sn (a metallic system).

Our results align with a broader trend identified in Ref. [122], which indicates that calculated formation energies for neutral defects in covalent materials tend to increase with the material's band gap. This pattern is likely due to wider valence bands and stronger covalent bonds in materials with larger band gaps, resulting in higher energy costs for bond-breaking during defect formation. The group-IV vacancy centers follow this trend closely, whereas the NV center shows slight deviations.

The formation energies at a Fermi energy level of $E_{\mathrm{F}} = 0$ of $\mathrm{C_i}$, $\mathrm{O_i}$, and $\mathrm{C_iO_i}$ defects in silicon are presented in Table 3.6, with neutral charge states highlighted in bold. For $\mathrm{C_i}$ defect, the SCAN functional predicts a formation energy of 3.49 eV, slightly lower than the HSE06 result of 3.70 eV, indicating a modest discrepancy between functionals. In the case of the neutral $\mathrm{O_i}$ defect, the SCAN and HSE06 formation energies are 1.79 eV and 1.81 eV, respectively, closely matching the upper end of the experimental range, 1.65(15) eV [123]. For the neutral $\mathrm{C_iO_i}$ complex, SCAN yields a formation energy of 3.75 eV, while HSE06 provides a slightly higher value of 3.95 eV. These results agree well with previous

Table 3.6: Calculated formation energies (in eV) of $\mathrm{C_i}$, $\mathrm{O_i}$, and $\mathrm{C_iO_i}$ defects in silicon at $E_\mathrm{F} = 0$. Neutral charge states are highlighted.

	$\mathrm{C_i}$			$\mathrm{C_iO_i}$		$\mathrm{O_i}$
	+	0	−	+	0	0
SCAN	3.29	**3.49**	4.20		**3.75**	**1.79**
HSE06	3.38	**3.70**	4.69	3.56	**3.95**	**1.81**

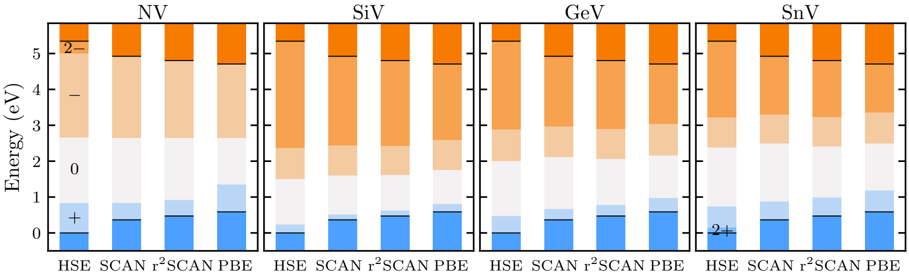

Figure 3.8: Charge-state transition levels of NV, SiV, GeV, and SnV centers in diamond, aligned to a common reference. Colored regions within the bandgap correspond to ranges of the stability of different charge states. Horizontal black bars correspond to the position of VBM and CBM for a given functional. Zero energy corresponds to the position of VBM in HSE06.

theoretical studies, which report formation energies in the range of 3.63–4.85 eV [124–126].

3.3.7. Charge-state transition levels

The computed charge transition levels for four diamond defects are presented in Fig. 3.8 and Table 3.7. Results from calculations at the HSE06 level align with previous findings in the literature [120, 127]. To facilitate comparison across functionals, the CTLs were aligned to a common reference, as described in Sec. 3.2.2. Notably, CTLs derived from the rSCAN and $\mathrm{r^2SCAN}$ functionals are very closely matched; therefore, rSCAN results are omitted from Fig. 3.8 for improved visual clarity.

In line with expectations, CTLs positioned well within the diamond band gap show strong alignment between different functionals, despite their variations in predicted band gaps [91–93]. However, for shallower defect levels, deviations become more pronounced. For instance, the (+/0) levels of group-IV vacancy centers in diamond, located near the

Table 3.7: Calculated charge-state transition levels of NV, SiV, GeV, and SnV defects in diamond (in eV).

	NV			SiV			GeV			SnV			
	+/0	0/−	−/2−	+/0	0/−	−/2−	+/0	0/−	−/2−	2 + /+	+/0	0/−	−/2−
PBE	0.76	2.06	4.11	0.22	1.17	2.02	0.39	1.57	2.46	0.04	0.60	1.91	2.78
SCAN	0.48	2.28	4.53	0.15	1.25	2.07	0.31	1.75	2.60	0.00	0.513	2.13	2.93
rSCAN	0.48	2.18	4.35	0.16	1.17	1.98	0.32	1.61	2.45	0.02	0.53	1.96	2.79
r^{2}SCAN	0.44	2.18	4.33	0.16	1.15	1.96	0.31	1.59	2.43	0.01	0.52	1.94	2.77
HSE06	0.83	2.67	5.00	0.23	1.51	2.37	0.47	2.01	2.88	0.15	0.74	2.39	3.22

valence band maximum (VBM), tend to shift alongside the VBM as band edges vary across functionals.

The NV and SnV centers exhibit the most significant differences among the functionals. For the NV center, the HSE06 functional predicts the (−/2−) level to be slightly below the conduction band minimum (CBM) [120], whereas other functionals place this level at or near the CBM. Since experimental evidence for the doubly negatively charged state remains inconclusive, it is unclear if this $q = -2$ state is genuine or an artifact of the HSE06 functional. Similarly, for the SnV center, HSE06 predicts the (+/2+) CTL to lie very close to the VBM, while other functionals position this level directly at the VBM. The experimental stability of the $q = +2$ charge state for SnV remains unconfirmed.

Given that the HSE06 functional's band gap closely matches experimental values, we use HSE06 results as a benchmark. Fig. 3.8 shows that CTLs calculated with the SCAN and r^{2}SCAN functionals align better with HSE06 predictions than those from the PBE functional. The calculated mean absolute error (MAE) for CTLs is 0.30 eV for PBE, 0.12 eV for SCAN, and 0.15 eV for r^{2}SCAN. Consequently, when using a common alignment reference, the SCAN family of functionals demonstrates at least a twofold reduction in CTL prediction errors compared to PBE. This improvement suggests that SCAN-based functionals provide enhanced accuracy for estimating experimental CTL positions within the diamond band gap, following the methodology outlined in Refs. [92,93].

3.3.8. Zero-phonon line energies

Calculated ZPL energies of optical transitions for negatively charged color centers in diamond are given in Table 3.8. Mean absolute errors (MAE) with respect to the experimental values of the ZPL energy are also provided. The calculated ZPL energies obtained with PBE and

Table 3.8: Calculated zero-phonon line energies for negatively-charged color centers in diamond, compared to experimental ones (in eV). MAE is the mean absolute error for each functional.

	NV^-	SiV^-	GeV^-	SnV^-	MAE
PBE	1.692	1.486	1.855	1.845	0.203
SCAN	1.867	1.567	2.001	1.974	0.070
rSCAN	1.812	1.543	1.948	1.932	0.114
r^2SCAN	1.806	1.533	1.943	1.929	0.120
HSE06	2.002	1.717	2.139	2.105	0.068
Expt.	1.945[a]	1.682[b]	2.059[c]	2.003[d]	

[a] Ref. [13] [b] Ref. [133] [c] Ref. [134] [d] Ref. [135]

HSE06 functionals align well with results from earlier theoretical studies [127–130]. We observe that HSE06 tends to slightly overestimate ZPL energies, yielding an average deviation of 0.068 eV. In contrast, other functionals, particularly PBE, generally underestimate ZPL energies, with PBE showing the largest mean absolute error (MAE) of 0.203 eV. Overall, the SCAN functional achieves accuracy close to that of HSE06. On the other hand, the rSCAN and r^2SCAN functionals reduce the accuracy of SCAN, resulting in average errors of 0.114 and 0.120 eV, respectively, though they still outperform PBE.

For the negatively charged nickel-vacancy (NiV^-) center, the r^2SCAN functional yields a ZPL value of 1.36 eV, which closely matches the experimental ZPL energy of 1.40 eV [131]. This result also aligns well with previous theoretical predictions using the HSE06 functional, which produced a ZPL value of 1.37 eV [132].

Table 3.9 provides a comparison between the calculated and experimental zero-phonon line energies for four configurations of neutral divacancies. The ZPL energies were determined using the SCAN and r^2SCAN functionals. For reference, previous theoretical ZPL estimates for divacancy configurations in 4H-SiC, computed with various density functionals, are also included in the table. In terms of accuracy, we observe that the SCAN functional yields ZPL energies very close to the experimental values, with a MAE of 0.021 eV, making it the most accurate among the tested functionals in this study. The r^2SCAN functional, while still achieving a reasonable level of accuracy, produces slightly higher discrepancies with an MAE of 0.035 eV. Results obtained using

Table 3.9: Calculated and experimental zero-phonon line energies (in eV) for neutral divacancy centers in 4H-SiC. Previous theoretical ZPL predictions are also included. MAE denotes the mean absolute error (in eV).

		hh	*kk*	*hk*	*kh*	MAE
This work	SCAN	1.129	1.123	1.141	1.103	0.021
	r^2SCAN	1.079	1.081	1.100	1.062	0.035
Previous theoretical work	PBE	0.925[a]	0.945[a]	0.975[a]	0.95[a]	0.170
		0.9375[b]	0.951[b]	0.979[b]	–	0.158
	HSE06	1.056[a]	1.044[a]	1.103[a]	1.081[a]	0.044
		1.221[b]	1.218[b]	1.269[b]	–	0.122
		1.13[c]	1.14[c]	1.21[c]	1.24[c]	0.065
	DDH	1.196[b]	1.201[b]	1.259[b]	–	0.105
	Expt.[d]	1.095	1.096	1.150	1.119	

[a] Ref. [98]: VASP calculations with PAW pseudopotentials.
[b] Ref. [102]: Quantum Espresso with ONCV pseudopotentials.
[c] Ref. [136]: VASP with PAW pseudopotentials. [d] Ref. [137]

the meta-GGA class functionals (SCAN and r^2SCAN) demonstrate a better match with experimental results than those obtained with the more computationally demanding hybrid HSE06 or DDH functionals. In our calculations, meta-GGA functionals demonstrated computational speeds approximately 26 to 38 times faster than hybrid HSE06 functional, while being about 20% slower than PBE.

3.3.9. Vertical excitation energies

The calculated $^3A_2 \leftrightarrow {}^3E$ vertical excitation energies for the NV^- center in diamond are presented in Table 3.10, while Table 3.11 provides the calculated $^2E_g \leftrightarrow {}^2E_u$ vertical excitation energies for negatively charged group-IV vacancy centers. For comparison, available experimental values and values computed with time-dependent density functional theory (TDDFT) are also included.

From Table 3.10, we observe that the SCAN functional yields the closest vertical excitation energy to the experimental value of 2.180 eV for the NV^- center, with a calculated value of 2.104 eV. SCAN's variants, rSCAN and r^2SCAN, also perform well, producing E_{VE} values within a range of 2.055–2.104 eV, which slightly underestimate the ex-

Table 3.10: Calculated zero-phonon line (ZPL), ionic relaxation energy (E_{rel}), and ${}^3A_2 \leftrightarrow {}^3E$ vertical excitation energies (E_{VE}) (in eV) for the NV$^-$ center in diamond. TDDFT value from the literature are given in parentheses.

	PBE	SCAN	rSCAN	r^{2}SCAN	HSE06	Expt.
E_{ZPL}	1.692	1.867	1.812	1.806	2.002	1.945[a]
E_{rel}	0.219	0.238	0.245	0.249	0.298	–
E_{VE}	1.911 (2.095[b])	2.104	2.056	2.055	2.300	2.180[a]

[a] Ref. [139] [b] Ref. [140]

Table 3.11: ${}^2E_g \leftrightarrow {}^2E_u$ vertical excitation energies (in eV) for negatively charged group-IV vacancy centers in diamond. TDDFT value from Ref. [138].

	PBE	SCAN	HSE06	TDDFT
SiV$^-$	1.506	1.588	1.744	1.59
GeV$^-$	1.878	2.041	2.191	–
SnV$^-$	1.925	2.043	2.190	–

perimental result. The HSE06 functional, while producing a higher E_{VE} of 2.300 eV, tends to slightly overestimate the excitation energy. As expected, the PBE functional yields a lower E_{VE} (1.911 eV), indicating that standard GGA functionals using ΔSCF methodology may lack the precision needed to accurately capture excitation energies in defect centers.

Table 3.11 summarizes the ${}^2E_g \leftrightarrow {}^2E_u$ vertical excitation energies for group-IV vacancy centers (SiV$^-$, GeV$^-$, and SnV$^-$). For the SiV$^-$ center, SCAN's excitation energy of 1.588 eV closely matches the TDDFT value of 1.59 eV which was calculated with CAM-B3LYP functional [138], demonstrating its reliability. The HSE06 functional produces higher excitation energies for SiV$^-$, GeV$^-$, and SnV$^-$ centers, indicating a trend of slight overestimation when compared to SCAN and experimental values. As with the NV$^-$ center, PBE functional results are generally lower across all group-IV vacancies, underscoring its tendency to underestimate excitation energies.

Table 3.12: Calculated and experimental zero-field splitting (ZFS) values (in GHz) for neutral divacancy centers in 4H-SiC. Previous theoretical ZFS predictions are also included. MAE denotes the mean absolute error (in GHz).

		hh	*kk*	*hk*	*kh*	MAE
This work	SCAN	1.336	1.271	1.320	1.279	0.026
	r^{2}SCAN	1.335	1.285	1.328	1.292	0.024
Previous theoretical work	PBE	1.358[a]	1.321[a]	1.320[a]	1.376[a]	0.052
		1.387[b]	1.349[b]	1.306[b]	1.356[b]	0.064
		(1.682)[b]	(1.635)[b]	(1.580)[b]	(1.641)[b]	(0.335)
	HSE06	1.329[c]	1.307[c]	1.363[c]	1.314[c]	0.033
	Expt.[d]	1.336	1.305	1.334	1.222	

[a] Ref. [141]: Calculations were carried out using VASP with PAW pseudopotentials.

[b] Ref. [142]: Calculations were performed using Quantum Espresso with ONCV pseudopotentials; values in parentheses were obtained using PAW pseudopotentials.

[c] Ref. [98]: Calculations used VASP with PAW pseudopotentials. [d] Ref. [137]

3.3.10. Zero-field splitting

Table 3.12 summarizes the calculated and experimental zero-field splitting values for four configurations of neutral divacancy centers in 4H-SiC. ZFS calculations were performed using the SCAN and r^{2}SCAN functionals, with previous theoretical predictions from different density functionals included for comparison.

Among the tested functionals, SCAN demonstrates excellent agreement with experimental values, achieving a MAE of 0.026 GHz. The r^{2}SCAN functional closely follows, with an MAE of 0.024 GHz, indicating that both functionals from the meta-GGA class deliver high accuracy in predicting ZFS values for 4H-SiC divacancies. In contrast, the PBE functional exhibits greater deviations from experimental results, with MAEs between 0.052 and 0.064 GHz. The PBE results calculated with PAW pseudopotentials using Quantum Espresso (shown in parentheses) display particularly large discrepancies with MAE of 0.335 GHz. The hybrid HSE06 functional achieves relatively good accuracy with an MAE of 0.033 GHz, though it remains slightly less accurate than SCAN and r^{2}SCAN.

3.4. Summary and conclusions

In this chapter, we have benchmarked the performance of the SCAN meta-GGA functional and its variants, rSCAN and r^{2}SCAN, in predicting bulk and point defect properties in diamond, silicon carbide, and silicon. The main achievements of this study are summarized as follows:

1. We demonstrated that the SCAN family of functionals improves the prediction of bulk properties:
    (a) SCAN, rSCAN, and r^{2}SCAN yield lattice constants and bulk moduli in excellent agreement with experimental values, offering nearly ideal descriptions of bulk lattice properties for diamond, silicon, and silicon carbide polytypes. In comparison, PBE predicts a ”softer” structure with a slightly larger equilibrium lattice constant and lower bulk modulus, whereas HSE06 predicts a ”harder” structure with a smaller lattice constant and higher bulk modulus.
    (b) The SCAN family reduces the discrepancy in band gap predictions compared to PBE functional. While SCAN and its variants improve the band gap estimate over PBE, they still fall short of the accuracy achieved by the hybrid functional HSE06, which incorporates a portion of exact exchange. Nevertheless, SCAN and its variants offer a valuable balance between computational efficiency and improved accuracy, particularly for high-throughput or large-scale simulations.
    (c) SCAN, particularly r^{2}SCAN, provides phonon frequencies best matching experimental data for bulk diamond.
2. For point defect properties, we found that:
    (a) Using the SCAN family of functionals, the calculated defect formation energies fall in between the formation energies calculated using PBE and HSE06.
    (b) When aligned to a common reference, the SCAN and r^{2}SCAN functionals yield charge-state transition levels that closely match those calculated with the HSE06 functional. These functionals demonstrate a twofold reduction in the mean absolute error of CTL predictions compared to PBE.

(c) The SCAN and r^{2}SCAN functionals provide highly accurate predictions of zero-phonon line energies for defects in diamond and 4H-SiC, achieving mean absolute errors that are comparable to or smaller than those of other hybrid functionals, while significantly outperforming the PBE functional.

(d) For zero-field splitting values of neutral divacancy centers in 4H-SiC, the SCAN and r^{2}SCAN functionals deliver exceptional accuracy, yielding lower mean absolute errors compared to those obtained with the HSE06 functional.

Thesis Statement (I)

The SCAN family of functionals provides accuracy comparable or better to the more computationally expensive hybrid HSE06 functional for optical excitation energies for defects in diamond and 4H silicon carbide.

Chapter 4

Electron–phonon coupling modelling

4.1. Introduction

This chapter presents our *ab initio* study of electron–phonon coupling and its impact on the optical lineshapes of the negatively charged nitrogen-vacancy (NV^-) center in diamond, neutral divacancy defects in 4H-SiC, and the C-center in silicon. The primary objective of this chapter is to evaluate the accuracy of the SCAN family of functionals in modeling electron–phonon interactions and the resulting optical lineshapes, comparing them with those obtained using the standard PBE and HSE06 functionals, as well as with available experimental data.

The content of this chapter is organized as follows. In Section 4.3.1, we focus on the NV^- center in diamond. We begin by benchmarking the spectral densities of electron–phonon coupling and discussing the contributions of vibrational modes to the optical spectra. We then proceed to calculate luminescence lineshapes using different functionals and compare the theoretical results with experimental data. The section concludes with an analysis of the effect of hydrostatic pressure on the luminescence lineshapes, revealing the changes in the zero-phonon line energy and phonon sideband structure under increasing pressure. Section 4.3.2 covers the electron–phonon coupling and subsequent optical lineshapes of neutral divacancy defects in 4H-SiC obtained using the r^2SCAN functional. We present the spectral densities of electron–phonon coupling and compare the luminescence lineshapes with available experimental spectra. Additionally, we present absorption lineshapes for all four divacancy configurations, computed using the standard adiabatic Huang–Rhys formalism. The influence of Jahn–Teller interactions will be explored in the following chapter. In Section 4.3.3, we investigate the electron–phonon coupling in the C-center defect in silicon and compute theoretical optical lineshapes using the SCAN functional, comparing them with available experimental data. Finally, in Section 4.4, we summarize our findings and emphasize the key statements that support the main conclusions of this chapter for the defense.

4.2. Methodology

4.2.1. Computational details

Calculations were performed using spin-polarized density functional theory with the Vienna Ab initio Simulation Package VASP [63]. The plane-wave energy cutoff was set to 600 eV for diamond and 4H-SiC, and 500 eV for silicon. The tested functionals included PBE, SCAN, rSCAN, r^{2}SCAN, and HSE06, with a screened Fock exchange fraction of $a = 0.25$. The Brillouin zone was sampled at the Γ-point using a single **k**-point. Defects were modeled using a supercell approach [143]. The convergence criterion for the electronic self-consistent loop was set to 10^{-6} eV for the HSE06 functional and 10^{-8} eV for all other functionals. Ionic relaxation was considered converged when the forces on atoms fell below 10^{-4} eV Å^{-1}.

Supercells containing 512 atomic sites ($4 \times 4 \times 4$ conventional cells) were used for the NV$^-$ center in diamond and the C-center in silicon. For neutral divacancy defects in 4H-SiC, a $6 \times 6 \times 2$ supercell with 576 atomic sites was employed.

4.2.2. Phonon calculations

Phonon calculations were performed using the SCAN functional for the C-center in silicon, and the r^{2}SCAN functional for the NV$^-$ center in diamond and neutral divacancies in 4H-SiC. All phonon modes were calculated using the finite displacement method, with atomic displacements generated by the `PHONOPY` software package [144]. Displacement amplitudes of ± 0.01 Å from the equilibrium geometries were used for the NV$^-$ center and divacancies, while a larger displacement of ± 0.02 Å was applied for the C-center in silicon.

Extrapolation of phonon modes to the dilute limit was carried out using the force constant embedding methodology described in Section 2.6. Vibrational structures and electron–phonon spectral functions were computed for each defect as follows:

- **NV$^-$ center in diamond:** For PBE and HSE06 functionals, phonon modes were calculated using a $20 \times 20 \times 20$ supercell containing 64 000 atomic sites. For meta-GGA functionals (SCAN, rSCAN, r^{2}SCAN), a 18 × 18 × 18 supercell with 46 656 atomic sites was used. For investigations under hydrostatic pressure, vibrational structures were obtained using a 16 × 16 × 16 supercell with 32 768 atomic sites. To achieve a smooth representation of the electron–phonon spectral function, delta functions were approximated with Gaussian functions of variable widths, σ, decreasing linearly from 3.5 meV at zero frequency to 1.5 meV at the highest phonon energy.

- **Neutral divacancies in 4H-SiC:** Vibrational structures were calculated using a 23×23×7 supercell with 29 622 atomic sites. The delta functions were smoothed with Gaussian functions of variable widths, decreasing from 3.5 meV at zero frequency to 1.5 meV at the maximum phonon energy.
- **C-center in silicon:** Phonon modes were computed using an 18 × 18 × 18 supercell containing 46 656 atomic sites. To ensure a continuous electron–phonon spectral function, delta functions were smoothed with Gaussian broadening ranging from 1 meV at zero frequency to 0.5 meV at the highest phonon energy.

4.2.3. Spacial localization of phonon modes

To distinguish among various types of vibrational modes (localized modes, vibrational resonances, and bulk-like modes) in the defect system, we analyzed the spatial localization of the vibrational mode amplitudes. This localization is quantified using the inverse participation ratio (IPR), which is defined for each phonon mode k as [145, 146]:

$$\mathrm{IPR}_k = \frac{1}{\sum_m \boldsymbol{\eta}_{k;m}^4}. \tag{4.1}$$

Here $\boldsymbol{\eta}_{k;m}$ denotes the three-dimensional mass-weighted displacement vector of atom m for phonon mode k, and $\boldsymbol{\eta}_{k;m}^4 \equiv \left(\sum_\alpha \eta_{k;m\alpha}^2\right)^2$, where $\eta_{k;m\alpha}$ represents the normalized mass-weighted displacement of atom m along the direction α. The inverse participation ratio, IPR$_k$, quantifies the number of atoms actively vibrating in a given vibrational mode $\boldsymbol{\eta}_k$.

For instance, IPR = 1 when only a single atom participates in the vibration for a particular mode. In contrast, IPR $= N$ if all N atoms in the supercell contribute equally to the vibration. In scenarios where only $P < N$ atoms exhibit significant vibrations, IPR $\approx P$. A localized mode is identified by an IPR value that remains constant regardless of the supercell size N, as such modes are spatially confined and lie outside the bulk phonon spectrum. The localized mode's frequency does not overlap with the bulk phonon bands, and its spatial characteristics remain unaffected by changes in the bulk phonon environment.

Although IPR effectively quantifies phonon mode localization, the localization ratio β_k of phonon mode k offers a more convenient parameter for practical analysis:

$$\beta_k = \frac{N}{\mathrm{IPR}_k}. \tag{4.2}$$

From this definition, it is evident that a higher value of the ratio β_k indicates greater localization of the phonon mode.

4.2.4. Optical lineshapes

Optical lineshapes in this chapter were computed using the adiabatic Huang–Rhys formalism, without accounting for the dynamical Jahn–Teller effect, which will be addressed in the following chapter. The methodology is outlined in detail in Section 2.5.1. Since homogeneous Lorentzian broadening of the ZPL is not inherently captured by the theoretical framework, a phenomenological correction term, $e^{-\gamma|t|}$, was incorporated into the optical spectral function. The parameter γ was adjusted to match the experimentally observed ZPL linewidth, where such data were available. For the luminescence of the NV^- center in diamond, the broadening parameter γ was set to 0.3 meV. For the luminescence lineshapes of neutral divacancies in 4H-SiC, γ was assigned a value of 0.15 meV for the *hh*, *kk*, and *hk* configurations, while for the *kh* configuration, it was set to 0.5 meV. For the absorption lineshapes of neutral divacancies in 4H-SiC, γ was consistently assigned a value of 0.15 meV. Finally, for the C-center in silicon, γ was set to 0.1 meV.

For the comparison between calculated and experimental lineshapes, the intensities of the experimental lineshapes were scaled to align with the peaks of the computed lineshapes. This adjustment was necessary because the experimental lineshapes are often truncated, both in terms of the total ZPL height and the full decay of the phonon sideband, making it impossible to properly normalize the experimental data.

When evaluating theoretical absorption lineshapes, it is essential to consider potential discrepancies between these predictions and the absorption lineshapes observed in experiments. These differences can arise due to the influence of the photoionization. In certain cases, the photoionization threshold, which represents the energy at which electrons are promoted into the conduction band minimum, may fall in the energy range of the absorption lineshape. As a result, absorption processes may include not only optical transitions from the ground state to the excited state but also photoionization from the excited state into the conduction band continuum. Consequently, the experimentally observed absorption spectrum is expected to reflect a convolution of both photoionization and bound-to-bound transition cross-sections. Despite this, some sharp features predicted by the theoretical lineshape are likely to remain discernible in experimental absorption spectra.

4.3. Results and discussion

4.3.1. NV$^-$ center in diamond

4.3.1.1 Electron–phonon coupling

The spectral densities of electron–phonon coupling for the NV$^-$ center in diamond, associated with the ${}^3E \rightarrow {}^3A_2$ transition, are illustrated in Figure 4.1. Panel **a** shows the spectral densities $S_{a_1}(\hbar\omega)$, which correspond to phonons of a_1 symmetry. These densities are defined as $S_{a_1}(\hbar\omega) = \sum_k S_{a_1,k}\delta(\hbar\omega - \hbar\omega_k)$, where $S_{a_1,k}$ represents the Huang-Rhys factor [34,81,82], indicating the average number of a_1-symmetry phonons emitted during an optical transition.

Panel **b** presents the spectral densities $K^2(\hbar\omega)$ that characterize electron-phonon coupling for e-symmetry phonons. These densities are given by $K^2(\hbar\omega) = \sum_k K_k^2\delta(\hbar\omega - \hbar\omega_k)$, where K_k denotes the dimensionless vibronic coupling constant [34, 74, 75]. This constant quantifies the interaction between e-symmetry vibrational modes and the degenerate electronic state ${}^3E$. Although the coupling constants K_k, were originally derived for linear Jahn–Teller interactions [see Eq. (2.71)], they share the same mathematical form as the Huang–Rhys factors [see

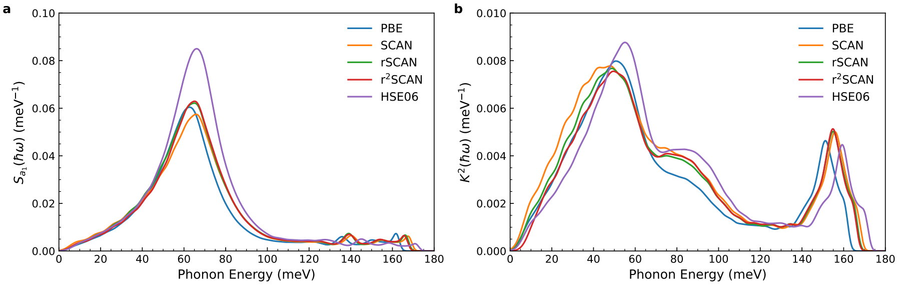

Figure 4.1: **a** Spectral densities $S_{a_1}(\hbar\omega)$ associated with a_1-symmetry phonons of the $^3E \rightarrow {}^3A_2$ transition in the case of the NV$^-$ center in diamond. **b** Spectral densities of JT linear coupling $K^2(\hbar\omega)$ associated with e-symmetry phonons of the $^3E \rightarrow {}^3A_2$ transition.

Eq. (2.92)]. Furthermore, for transitions between orbital singlet and doublet states, they are computed identically – since the geometric distortion along the e-symmetry direction between the adiabatic minima mirrors the symmetry breaking induced by the Jahn–Teller effect. For transitions where the final state is non-degenerate, the HR formalism to compute optical lineshape is a well-justified approximation, as demonstrated in Ref. [34]. However, for transitions involving a degenerate final state, the standard HR theory may not be strictly applicable. In the framework of this chapter, where we exclusively employ adiabatic theory, we will interpret the squared coupling constants, K_k^2, as effective HR factors.

A comparison of the calculated spectral densities for electron–phonon coupling in the NV$^-$ center in diamond, considering the total coupling to vibrational modes of a_1 and e symmetry, is presented in Figure 4.2. The calculations are performed using the PBE, SCAN, rSCAN, r^{2}SCAN, and HSE06 functionals. The spectral densities show a broad peak at 61.9 meV with the PBE functional, which shifts to 65.6 meV when using the HSE06 functional. For the SCAN, rSCAN, and r^{2}SCAN functionals, this quasi-local phonon mode is found at 65.8 meV, 64.4 meV, and 64.7 meV, respectively. At the tail-end of the spectral densities, small peaks are observed, corresponding to localized phonon modes, primarily associated with e-symmetry phonons (see Fig.4.1b).

The total electron–phonon interaction strength is represented by the cumulative Huang-Rhys factor, $S_{\text{tot}} = \sum_k S_k$, while the overall Jahn-Teller coupling is described by $K^2_{\text{tot}} = \sum_k K_k^2$. These spectral densities

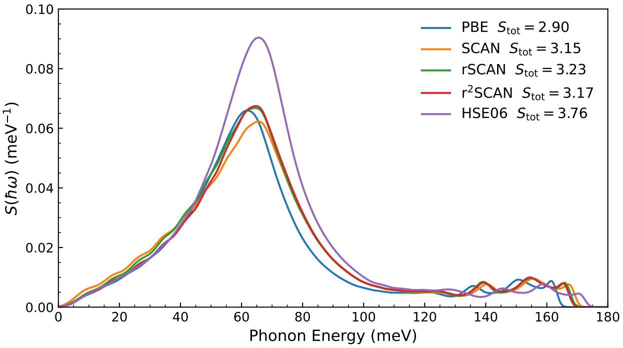

Figure 4.2: Cumulative spectral densities of electron–phonon coupling $S(\hbar\omega)$ for the $^3E \rightarrow {}^3A_2$ transition in the case of the NV$^-$ center in diamond.

provide insight into the differences in electron–phonon interactions predicted by various functionals and highlight the vibrational characteristics linked to the NV$^-$ center.

The values of $S_{a_1,\text{tot}}$ and K^2_{tot} are provided in Table 4.1, along with the total Huang–Rhys factor, $S_{\text{tot}} = S_{a_1,\text{tot}} + K^2_{tot}$, and the experimental result $S_{\text{tot}} \approx 3.49$ [147]. From the table, it is clear that the PBE functional yields $S_{\text{tot}} = 2.90$, which underestimates the experimental value. In contrast, the HSE06 functional predicts $S_{\text{tot}} = 3.76$, slightly overestimating the result. The SCAN, rSCAN and r^{2}SCAN functionals give 3.15, 3.23, and 3.17 total electron–phonon coupling respectively. These values are all closer to the experimental result compared to PBE, demonstrating that the SCAN-based functionals achieve a balance between underestimation and overestimation. These findings highlight the improved performance of the SCAN family in capturing electron–phonon coupling characteristics at a fraction of computational cost compared to hybrid functionals like HSE06.

4.3.1.2 Luminescence lineshapes

The calculated luminescence lineshapes for the PBE, SCAN, rSCAN, r^{2}SCAN, and HSE06 functionals are shown in Fig. 4.3 and compared against the experimental spectrum from Ref. [147]. Each lineshape features a sharp zero-phonon line accompanied by a phonon sideband (PSB). The quasi-local phonon mode identified in Fig. 4.2 generates three increasingly broad phonon replicas, which primarily define the

Table 4.1: Calculated Huang–Rhys factors for emission of NV$^-$ center in diamond.

	$S_{a_1,\text{tot}}$	K^2	S_{tot}
PBE	2.39	0.52	2.90
SCAN	2.55	0.60	3.15
rSCAN	2.67	0.56	3.23
r^{2}SCAN	2.62	0.54	3.17
HSE06	3.20	0.56	3.76
Expt.			3.49[a]

[a] Ref. [147]

overall lineshape. Additionally, localized *e*-symmetry phonon modes contribute small features between the second and third quasi-local phonon replicas.

For example, the luminescence lineshape obtained with the r^{2}SCAN functional exhibits three quasi-local phonon replicas (named R1, R2, and R3) at around 65.4, 126.7, and 192.1 meV, along with small features (named F1, F2, and F3) at 138.4, 153.7, and 165.1 meV below the ZPL energy. In comparison, the experimental lineshape from Ref. [147] shows these three quasi-local phonon replicas at around 63.5, 127, and 190.5 meV, with small features at 137, 152.2, and 163.6 meV. The detailed comparison between calculated and experimental phonon replica energies, including fine features, is summarized in Table 4.2.

The HSE06 functional underestimates the intensity of the first two phonon peaks in the PSB, whereas the PBE functional overestimates them. The lineshapes calculated using the SCAN family of functionals exhibit intermediate agreement with the experimental spectrum. Notably, the r^{2}SCAN functional provides the most accurate correspondence to the experimental data, achieving the smallest mean absolute error of 1.4 meV, as shown in Table 4.2.

The smooth spectral densities of electron–phonon coupling and luminescence were achieved using the force constant embedding methodology, as described in Section 2.6. To demonstrate the effectiveness of this approach, we present the calculated spectral densities of electron–phonon coupling (see Fig. 4.4a) and normalized luminescence lineshapes (see Fig. 4.4b) as a function of supercell size using the r^{2}SCAN functional. We considered supercell sizes of 4 × 4 × 4 (512 atomic sites),

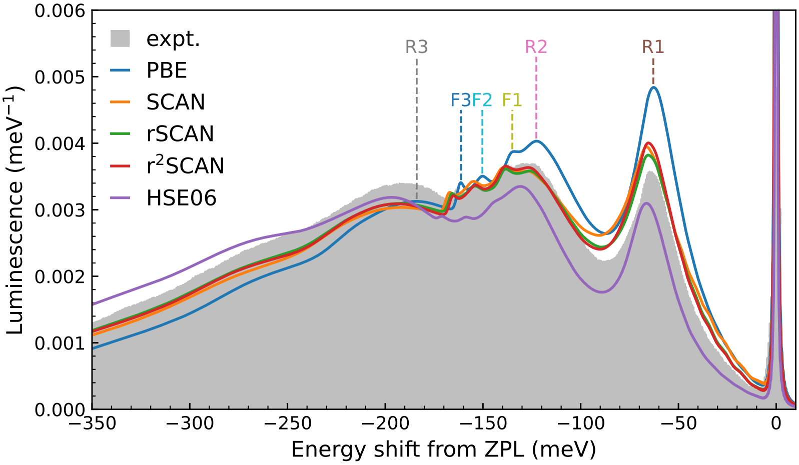

Figure 4.3: Theoretical normalized luminescence lineshapes of NV$^-$ center in diamond. Phonon replicas (R1, R2, R3) and fine features (F1, F2, F3) are marked for the theoretical lineshape calculated using the PBE functional. The gray area represents experimental spectra from Ref. [147].

Table 4.2: Comparison of calculated and experimental phonon replica energies (R1, R2, R3) and fine features (F1, F2, F3) below ZPL energy for the luminescence lineshape of the NV$^-$ center in diamond. The experimental values are taken from Ref. [147]. MAE is the mean absolute error that quantifies the deviation of each functional from the experimental values. All energies are reported in meV.

	R1	R2	R3	F1	F2	F3	MAE
PBE	62.9	122.7	183.9	135.0	150.3	161.3	3.0
SCAN	66.4	127.2	192.0	139.5	154.9	166.9	2.2
rSCAN	65.4	126.1	192.1	138.4	154.1	165.8	1.7
r^{2}SCAN	65.4	126.7	192.1	138.4	153.7	165.1	1.4
HSE06	66.2	129.8	196.7	145.2	158.6	169.9	5.4
Expt.	63.5	127.0	190.5	137.0	152.2	163.6	

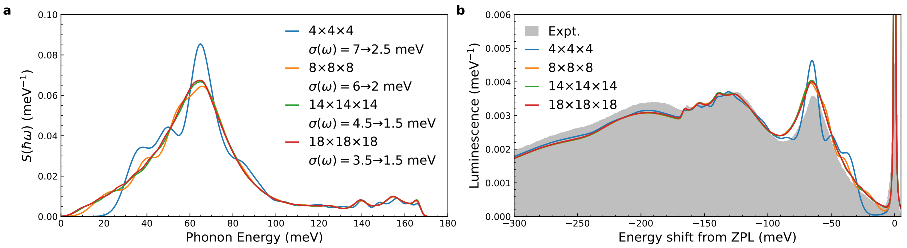

Figure 4.4: Convergence of **a** spectral densities of electron–phonon coupling and **b** theoretical luminescence lineshapes with respect to supercell size. Supercells range from $4 \times 4 \times 4$ (512 atomic sites) to $18 \times 18 \times 18$ (46 656 atomic sites). The gray area represents experimental spectra from Ref. [147].

$8 \times 8 \times 8$ (4 096 atomic sites), $14 \times 14 \times 14$ (21 952 atomic sites), and $18 \times 18 \times 18$ (46 656 atomic sites).

To achieve a smooth representation of the electron–phonon spectral function, delta functions were approximated using Gaussian functions with linearly decreasing widths, $\sigma(\omega)$, from 7, 6, 4.5, and 3.5 meV to 2.5, 2, 1.5, and 1.5 meV, respectively, for these supercell sizes. Convergence tests confirm that the $14 \times 14 \times 14$ supercell provides a well-converged and smooth spectral density, effectively capturing contributions from both low-energy acoustic and high-frequency phonon modes. However, larger supercells were used whenever computationally feasible to achieve higher accuracy.

4.3.1.3 Electron–phonon coupling under hydrostatic pressure

The NV^- center in diamond is a versatile quantum sensor capable of measuring magnetic and electric fields, temperature, stress, and mechanical vibrations [148–150]. Its high sensitivity and the stiffness of the diamond lattice make it ideal for probing materials under extreme pressures, where remarkable properties like metallic hydrogen [151] and high-temperature superconductivity in superhydrides [152–154] emerge.

The luminescence lineshape of the NV^- center serves as a sensitive probe of interactions between its electronic states and the surrounding environment. The fine structure of the spectrum provides valuable insights into shifts of phonon frequencies and emission characteristics under pressure. First-principles calculations using the SCAN functional family offer an efficient and accurate means to predict pressure-dependent behavior, bridging theory and experiment.

4.3.1.3.1 Zero-phonon line energy The ZPL energy of the NV$^-$ center in diamond under varying hydrostatic pressures is calculated using the ΔSCF method, as outlined in Section 3.2.3. At zero pressure, our computations with the r^{2}SCAN functional yield a ZPL energy of 1.806 eV, which slightly underestimates the experimentally measured value of 1.945 eV [13]. Despite this deviation, the r^{2}SCAN functional offers a reliable representation of the electronic structure while maintaining a significantly lower computational cost compared to hybrid functionals such as HSE06 (see Section 3.3.8). The calculations at various hydrostatic pressures were performed using lattice constants derived from the universal equation of state, as detailed in Section 3.3.1.

Figure 4.5 presents the calculated ZPL energies relative to the ambient pressure value as a function of hydrostatic pressure. The theoretical data points are shown as blue circles, with a solid blue line representing a spline fit to these values. Experimental data from Ref. [150] are depicted as orange diamonds, providing a direct comparison between theory and experiment. The experimental ZPL values at pressures of 10, 20, 40, and 75 GPa are 1.997, 2.054, 2.144, and 2.287 eV, respectively, while the corresponding calculated values yield relative shifts of 55, 106, 198, and 332 meV, compared to the experimental shifts of 52, 109, 200, and 342 meV.

The comparison reveals a consistent increase in ZPL energy with applied pressure, attributed to the compression of the diamond lattice and its influence on the defect's electronic structure. The r^{2}SCAN functional effectively captures this trend, demonstrating its capability to model pressure-induced changes in the NV$^-$ center with high accuracy. Although the absolute ZPL energies computed with r^{2}SCAN slightly underestimate experimental values, the relative pressure-dependent shifts exhibit excellent agreement with measurements. This consistency suggests that the computational model provides a reliable representation of the underlying physical mechanisms governing the NV$^-$ center's optical response under pressure.

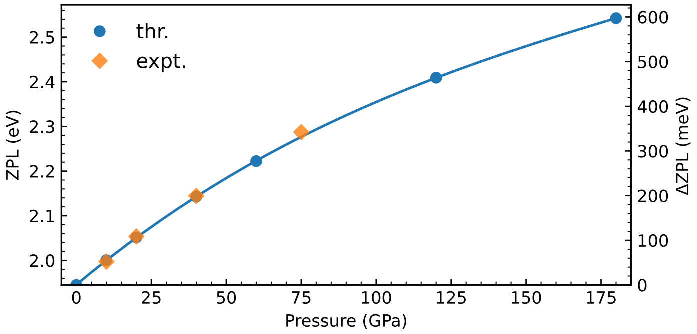

Figure 4.5: Experimental values of the ZPL (in units of eV) of the NV$^-$ center in diamond under increasing hydrostatic pressure from Ref. [150] (orange diamonds). The blue circles represent calculated ZPL values, shown relative to the ZPL energy at zero pressure (in units of meV). The solid blue line is a spline fit to the theoretical data.

4.3.1.3.2 Electron–phonon coupling The computed spectral densities of electron–phonon coupling for the luminescence of the NV$^-$ center in diamond under increasing hydrostatic pressure are presented in Figure 4.6. The total electron–phonon coupling (S_{tot}), total electron–phonon coupling associated with a_1-symmetry phonon modes ($S_{a_1,\text{tot}}$), and the total JT linear coupling (K^2_{tot}), corresponding to e-symmetry phonon modes (shown in the inset), are depicted in Fig. 4.7, along with their respective linear fits. The electron–phonon coupling exhibits a linear increase with hydrostatic pressure with the S_{tot} ranging from 3.164 at ambient pressure to 4.063 at 60 GPa, with corresponding slopes of 0.015, 0.012, and 0.003 GPa^{-1} for S_{tot}, $S_{a_1,\text{tot}}$, and K^2_{tot}, respectively. The increase in total electron–phonon coupling leads to a reduction of ZPL intensity and a decrease of emitter efficiency. The Debye–Waller factor (DWF), defined as the ratio of the ZPL intensity to the total luminescence lineshape, decreases with increasing hydrostatic pressure. At very low temperatures, the DWF can be approximated using the relation DWF $= e^{-S_{\text{tot}}}$. Employing this approach, the calculated DWF values are 4.23, 3.61, 3.09, 2.29, and 1.72 % for pressures of 0, 10, 20, 40, and 60 GPa, respectively.

The main electron–phonon coupling peak, initially at 65.4 meV under ambient pressure, exhibits a linear increase with pressure, following a slope of 0.061 meV/GPa. The high-energy phonon mode, which starts

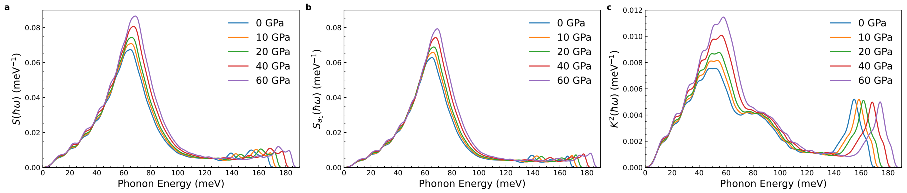

Figure 4.6: **a** Cumulative spectral densities of electron–phonon coupling, $S(\hbar\omega)$, for the NV$^-$ center in diamond under increasing hydrostatic pressure. **b** Spectral densities, $S_{a_1}(\hbar\omega)$, corresponding to phonons with a_1 symmetry. **c** Spectral densities of JT linear coupling, $K^2(\hbar\omega)$, associated with phonons of e symmetry.

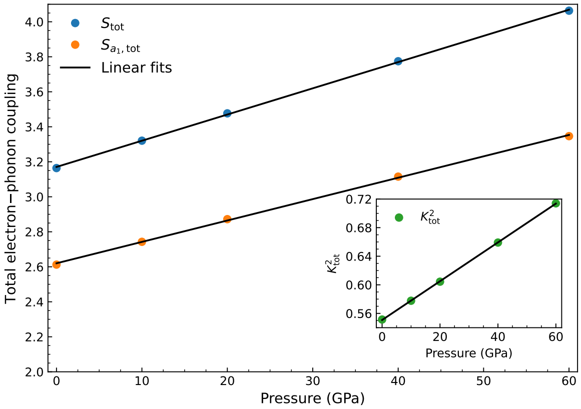

Figure 4.7: Total electron–phonon coupling S_{tot}, electron–phonon coupling for a_1-symmetry phonon modes, $S_{a_1,\text{tot}}$, and total JT linear coupling, K^2_{tot}, for e-symmetry phonon modes (shown in the inset) for the NV$^-$ center in diamond as a function of pressure.

at 154.4 meV at ambient pressure, demonstrates an increase in intensity alongside a linear energy shift of 0.337 meV/GPa. Likewise, the phonon mode initially at 165.4 meV under ambient pressure increases linearly with a slope of 0.282 meV/GPa.

4.3.1.3.3 Luminescence lineshapes under pressure The computed normalized luminescence lineshapes under increasing hydrostatic pressure are presented in Fig. 4.8, highlighting the identified quasi-local phonon replicas (R1, R2, R3), fine features coming from localized modes (F1, F2, F3), and the experimental luminescence lineshape at ambient pressure from Ref. [147]. The features exhibit a linear increase in energy relative to the ZPL, indicating that the corresponding phonon modes shift to higher energies with increasing pressure, as illustrated in Fig. 4.9.

For the phonon replica R1, the peak positions below the ZPL increase linearly with pressure, with slope of 0.061 meV/GPa. Trends for phonon replicas R2 and R3 are harder to distinguish due to overlap with other vibrational modes. Fine features F2 and F3 exhibit slopes of 0.363 and 0.292 meV/GPa, respectively. Fine feature F1 becomes indistinguishable from the overall luminescence spectrum as pressure increases. This can be correlated with the electron–phonon coupling strengths shown in Fig. 4.6a. At ambient pressure, the phonon mode at 139.4 meV exhibits an electron–phonon coupling strength comparable to that of the modes at 154.4 and 165.4 meV. However, at pressures of 40 GPa and higher, the coupling strength of the phonon mode diminishes, while the higher-energy phonon modes become more prominent, indicating their increased contribution to the luminescence process under elevated pressures.

The computed luminescence lineshapes are effectively modeled at 0 K temperature, where all fine features of the phonon sideband remain well-resolved. However, in experimental conditions at higher temperatures, thermal broadening can obscure these fine features, particularly those with the strongest pressure-dependent shifts. As a result, the first quasi-local phonon replica (R1) emerges as the most reliable feature for calibrating and evaluating pressure in NV$^-$ centers based on their luminescence lineshapes.

4.3.2. Neutral divacancies in 4H-SiC

4.3.2.1 Electron–phonon coupling

The calculated spectral densities of electron–phonon coupling for both emission ($^3E \to {}^3A_2$) and absorption ($^3A_2 \to {}^3E$) processes for the neutral axial hh-VV^0 and kk-VV^0 divacancies in 4H-SiC are shown in Fig. 4.10. Coupling to a_1-symmetry modes is represented by the spectral density $S_{a_1}(\hbar\omega) = \sum_k S_{a_1,k}\delta(\hbar\omega - \hbar\omega_k)$ (Figs. 4.10a and 4.10c), where $S_{a_1,k}$ quantifies the HR factor for vibrational mode k and represents the average number of a_1-symmetry phonons emitted during optical transitions. The linear JT coupling for e-symmetry modes is characterized by the spectral density $K^2(\hbar\omega) = \sum_k K_k^2\delta(\hbar\omega - \hbar\omega_k)$ (Figs. 4.10b and

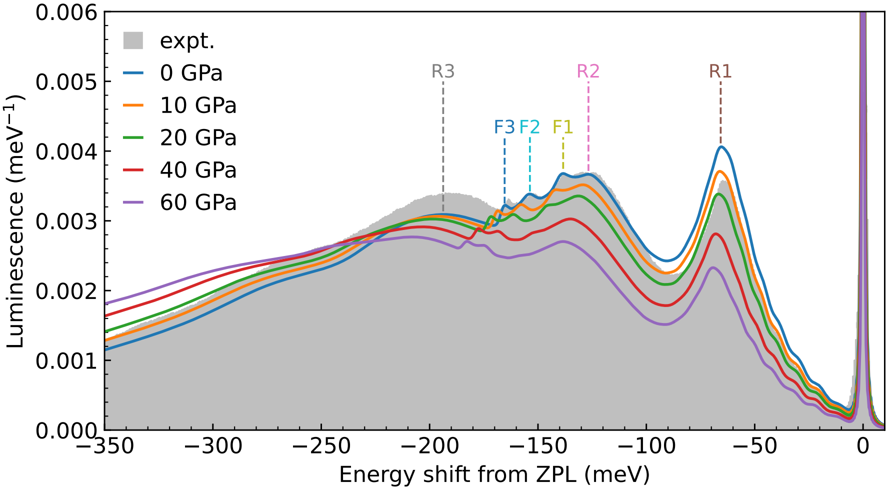

Figure 4.8: Theoretical normalized luminescence lineshapes of NV$^-$ center in diamond under increasing hydrostatic pressure. Phonon replicas (R1, R2, R3) and fine features (F1, F2, F3) are marked for the theoretical lineshape under ambient pressure. The gray area represents experimental spectra at no external pressure from Ref. [147].

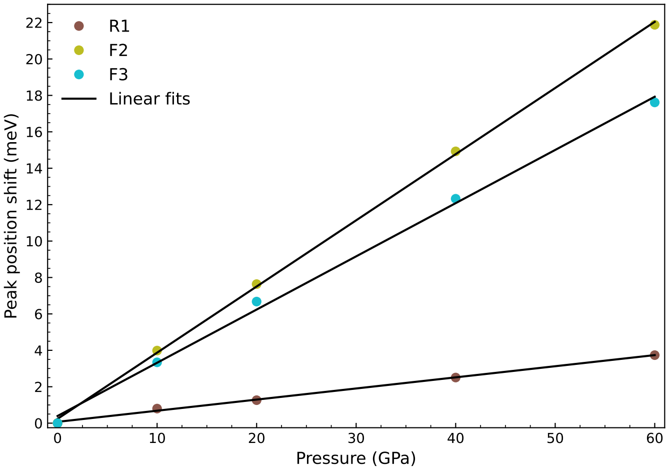

Figure 4.9: Calculated phonon replica (R1) and fine feature (F2, F3) energy shift under increasing hydrostatic pressure for the luminescence lineshape of the NV$^-$ center in diamond.

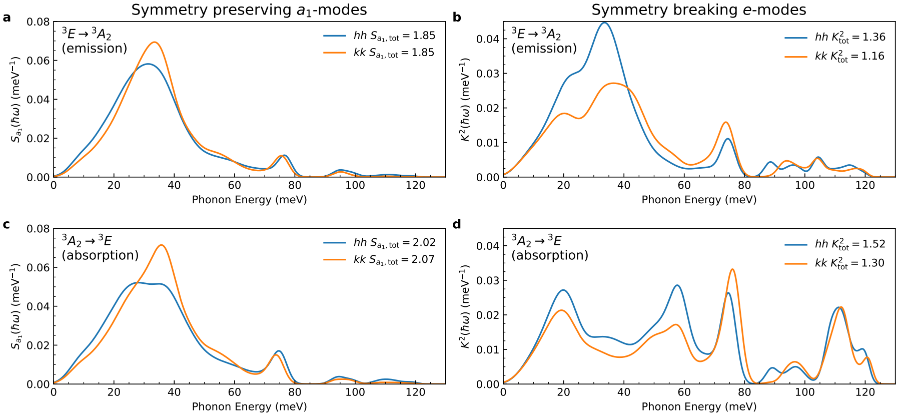

Figure 4.10: Spectral densities of electron–phonon coupling and JT linear coupling for neutral hh-VV^0 and kk-VV^0 divacancies in 4H-SiC. Panels **a** and **c** show the electron–phonon coupling spectral density $S_{a_1}(\hbar\omega)$ for the $^3E \rightarrow {}^3A_2$ and $^3A_2 \rightarrow {}^3E$ processes, respectively. Panels **b** and **d** present the JT linear coupling spectral density $K^2(\hbar\omega)$ for the same processes.

4.10d), where K_k is the dimensionless vibronic coupling constant. The total electron–phonon coupling ($S_{a_1,\mathrm{tot}} = \sum_k S_{a_1,k}$) and total JT coupling ($K^2_{\mathrm{tot}} = \sum_k K_k^2$) are also provided in the panels.

For the emission ($^3E \rightarrow {}^3A_2$) process, the total HR factor $S_{a_1,\mathrm{tot}}$ is 1.85 for both hh and kk divacancies, while the total JT coupling K^2_{tot} is higher for hh-VV^0 (1.36) compared to kk-VV^0 (1.16). During the absorption process ($^3A_2 \rightarrow {}^3E$), the total HR factor increases slightly to 2.02 for hh-VV^0 and 2.07 for kk-VV^0, with corresponding total JT couplings of 1.52 for hh and 1.30 for kk. These JT coupling values are significantly larger than those calculated for the absorption of NV$^-$ centers in diamond, which exhibit values of 0.51 (PBE) and 0.57 (HSE06) [34].

The combined spectral functions for the total coupling to a_1- and e-symmetry phonons during emission and absorption for hh and kk divacancies are presented in Fig. 4.11. The cumulative electron–phonon coupling factors (S_{tot}) for emission are 3.21 for hh-VV^0 and 3.00 for kk-VV^0, while for absorption, these values increase to 3.54 and 3.37, respectively. The stronger coupling during absorption results in more pronounced phonon sidebands and reduced ZPL intensity.

For the hh configuration, the electron–phonon coupling spectra for emission process exhibits prominent peaks at 33 meV and 75.7 meV, with

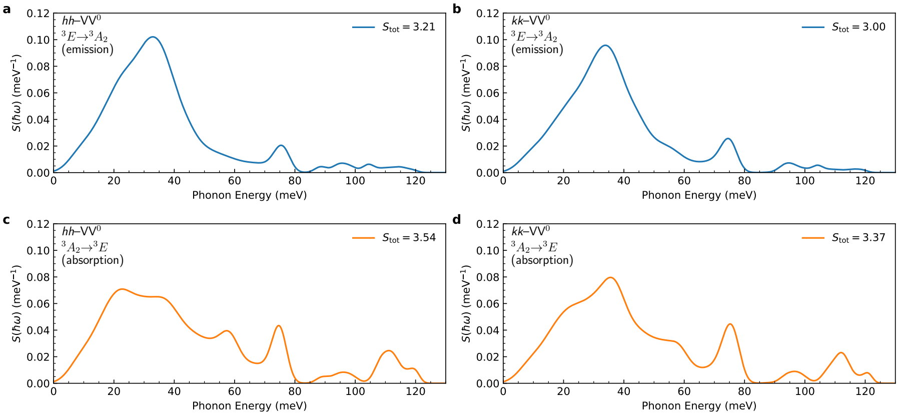

Figure 4.11: Cumulative spectral functions of electron–phonon coupling $S(\hbar\omega)$ for neutral *hh* and *kk* divacancies in 4H-SiC. Panels **a** and **b** show the coupling for emission in the *hh* and *kk* configurations, respectively, while panels **c** and **d** display the coupling for absorption in the same configurations.

weaker contributions at higher phonon energies of 88.6 meV, 95.4 meV, and 104.3 meV. In contrast, absorption exhibits weaker coupling at lower phonon energies, with peaks at 22.2 meV and 36.2 meV, but shows a more pronounced peak at 74.7 meV and an emerging peak at 58 meV. At higher phonon energies, absorption reveals distinct peaks at 111.7 meV and 119.6 meV, reflecting an increased contribution from high-energy *e*-symmetry phonons.

In the *kk* configuration, the emission spectrum is characterized by strong peaks at 34.1 meV and 74.6 meV, while contributions at higher phonon energies, such as 94.6 meV and 104.2 meV, are less pronounced. The absorption process, however, displays notable differences, with an enhanced peak at 22 meV and a subtler feature at 35.9 meV. In the mid-energy range, absorption exhibits an emerging peak at 57 meV and a more pronounced feature at 75.3 meV. High-energy phonons play a significant role during absorption, as evidenced by prominent peaks at 112 meV and 120.5 meV, indicating stronger coupling in this process compared to emission.

The calculated spectral densities of electron–phonon coupling for both emission and absorption processes for basal divacancies, *hk*-VV^0 and *kh*-VV^0, are shown in Fig. 4.12. The total HR factor, S_{tot}, indicates weaker coupling for *kh* divacancy ($S_{\text{tot}} = 2.47$ for emission and

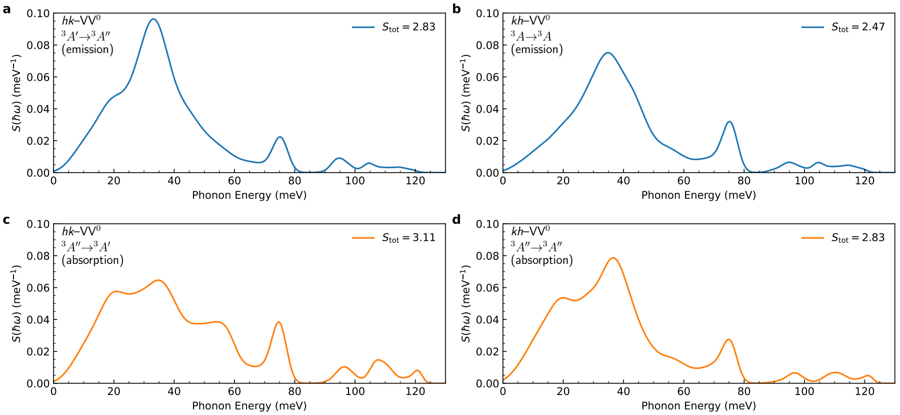

Figure 4.12: Spectral functions of electron–phonon coupling $S(\hbar\omega)$ for neutral hk and kh divacancies in 4H-SiC. Panels **a** and **b** show the coupling for emission in the hk and kh configurations, respectively, while panels **c** and **d** display the coupling for absorption in the same configurations.

2.83 for absorption) compared to hk divacancy ($S_{\mathrm{tot}} = 2.83$ and 3.11, respectively).

For the hk configuration, emission exhibits pronounced peaks at 33.2 meV and 75.1 meV, with a shoulder at 20.3 meV and weaker contributions at higher energies, such as 94.6 meV and 104.6 meV. Absorption, however, shows enhanced coupling at 20 meV, weaker coupling at 35 meV, an additional feature emerging at 54.2 meV and stronger feature at 74.8 meV. At higher phonon energies there is a similar peak at 96.4 meV and emergent peaks at 107.6 meV and 120.6 meV.

The kh configuration shows a slightly different behavior. Emission is characterized by prominent peaks at 34.8 meV and 75.3 meV, with weaker contributions at higher energies (94.9 meV and 104.6 meV). Absorption reveals subtle changes at higher energies, with small peaks at 96.7 meV, 110.3 meV, and 121 meV. A distinct feature of this configuration is the significant coupling peak at 19.4 meV during absorption, accompanied by a unique increase in coupling at 36.5 meV and a corresponding decrease at 75.1 meV, distinguishing it from other divacancy configurations.

The electron–phonon coupling was calculated using the equal mode approximation, which assumes identical vibrational structures for both the initial and final states. While this assumption is not entirely accurate, it serves as a reasonable approximation for low-temperature spectra by employing the vibrational structure of the final state in the transition [34]. Nonetheless, the variation in vibrational structure suggests the presence of quadratic electron–phonon coupling in addition to the Jahn–Teller effect, which is not included in the present analysis. This limitation could have significant implications for modeling temperature effects and ZPL broadening at finite temperatures in future studies.

4.3.2.2 Optical lineshapes

Luminescence lineshapes calculated using the HR theory are shown in Fig. 4.13 and compared with experimental data (gray shaded area) [102, 155]. The experimental spectrum for the *hk*-VV^0 contains a small peak (marked with an asterisk ”$*$” in Fig. 4.13c) that corresponds to the ZPL of the *hh*-VV^0 configuration. This peak should be disregarded when comparing theoretical and experimental data for the *hk* configuration.

Computed luminescence lineshapes closely match the experimental spectra, successfully reproducing all major spectral features of the phonon sideband. The DWF (ratio of the ZPL intensity to the total intensity of the lineshape) highlights notable differences among the four divacancy configurations. The computed DWFs using HR theory for the *hh*, *kk*, *hk*, and *kh* divacancies are 5.60%, 6.82%, 7.84%, and 11.22%, respectively. These values show good agreement with experimental measurements of 3.69% for *hh*, 6.11% for *kk*, 7.54% for *hk* [102], and 13% for *kh* divacancy [155]. Notably, when compared to other divacancy configurations, the *kh* configuration has a significantly higher DWF, indicating a more pronounced ZPL contribution relative to its phonon sideband.

The emission lineshapes for the *hh*, *kk*, and *hk* divacancies are similar in profile, whereas the *kh* divacancy exhibits distinct spectral characteristics. The calculated mass-weighted displacements ΔQ (in units of amu$^{0.5}$ Å), which quantify structural distortions during the optical transition, are 0.823 for *hh*, 0.802 for *kk*, 0.798 for *hk*, and 0.762 for *kh* divacancy. These values reflect the extent of structural rearrangement, with the *kh* divacancy showing the smallest displacement after the optical transition, consistent with its higher DWF and less extensive phonon sideband. The total electron–phonon coupling factor for *kh* divacancy is 2.47 which is significantly lower than for other divacancy configu-

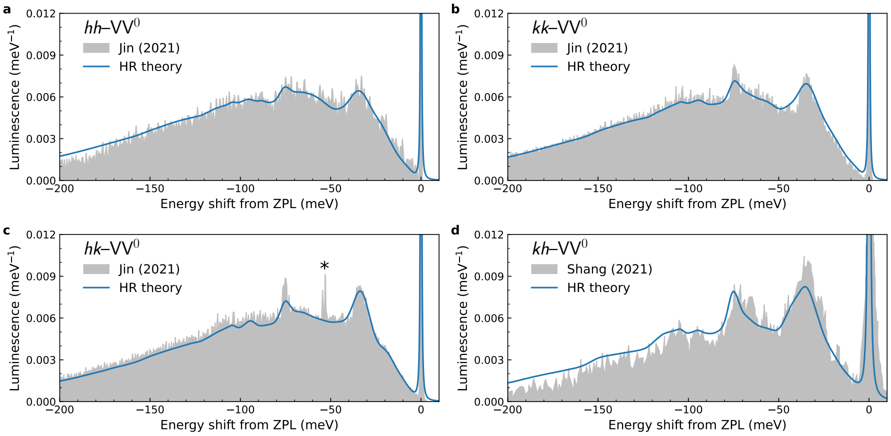

Figure 4.13: Optical spectra of emission for four neutral divacancy centers in 4H-SiC. Blue lines are theoretical normalized luminescence lineshapes calculated using HR theory. The gray area represents experimental data from Ref. [102,155]. The small peak marked with a star ”∗” in the experimental curve for *hk*-VV^0 is the ZPL of *hh*-VV^0 and should be disregarded in the comparison between theory and experiment.

rations. The lower mass-weighted displacement and electron–phonon coupling for the *kh* divacancy result in a more pronounced ZPL and unique vibrational properties, setting it apart from the other divacancy configurations in 4H-SiC.

Absorption lineshapes calculated using the HR theory are shown in Fig. 4.14. Calculation of absorption lineshapes for neutral axial divacancies using HR theory is not formally suitable due to the Jahn–Teller effect present in the excited state and will be tackled later in Sec. 5.3.3.

4.3.3. C-center in silicon

4.3.3.1 Vibrational structures

Figure 4.15a displays the calculated localization ratios β [see Eq. (4.2)] for a' symmetry vibrational modes in the ground state (blue) compared with experimental luminescence spectra (gray) [156]. The horizontal axis represents the energy shift relative to the ZPL. Localization ratios for the excited state are shown in Fig. 4.15b (orange). Higher β values indicate stronger localization of displacement amplitudes around the defect. The a'' vibrational modes are excluded, as their symmetry prevents

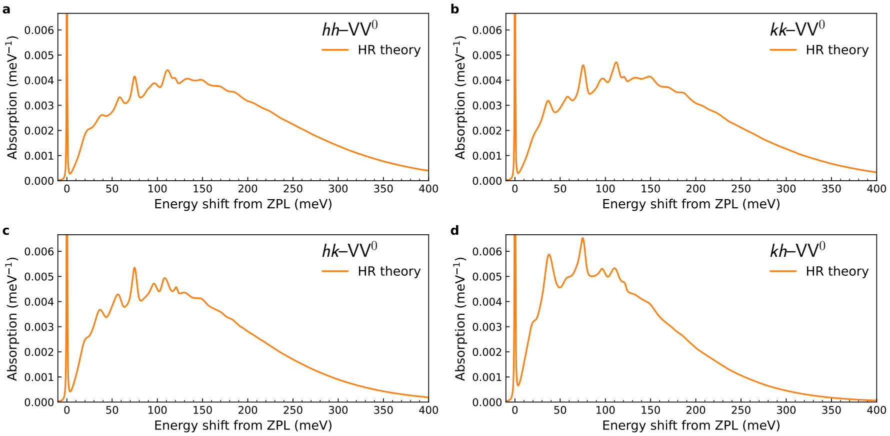

Figure 4.14: Optical spectra of absorption for four neutral divacancy centers in 4H-SiC. Orange lines are theoretical normalized absorption lineshapes calculated using HR theory.

contribution to linear electron–phonon interactions.

Localized modes with high β values ($\beta \geqslant 100$) are observed at 65.8 meV, 72.8 meV, 92.7 meV, 107.9 meV, and 139.7 meV. Among these, modes at 65.8 meV, 72.8 meV, and 92.7 meV strongly correspond to prominent peaks in the experimental sideband. In contrast, the absence of luminescence peaks at 107.9 meV and 139.7 meV indicates that a high β alone does not guarantee significant electron–phonon coupling. Effective contributions require alignment with the relaxation vector $\Delta\boldsymbol{R}$ after the optical transition, as defined in Eq. (2.93).

Quasi-localized modes (with $\beta > 10$) near 32 meV, 54 meV, and 62 meV are classified as vibrational resonances. These modes likely correspond to features in the experimental spectrum, suggesting their role in electronic transition coupling. In contrast, bulk-like modes with lower β values ($\beta \leqslant 5$) extend to 65 meV, consistent with the phonon band edge in pristine silicon. These modes represent collective lattice vibrations and appear in both pure and defected systems, corresponding to experimental luminescence peaks and highlighting their bulk-like nature.

Figure 4.15b illustrates the vibrational frequencies and localization factors for the positively charged defect, representing the excited state's structure. A comparison with Fig. 4.15a reveals a frequency reduction in localized modes, with the 65.8 meV mode in the ground state shifting below the bulk phonon band maximum in the excited state, becoming

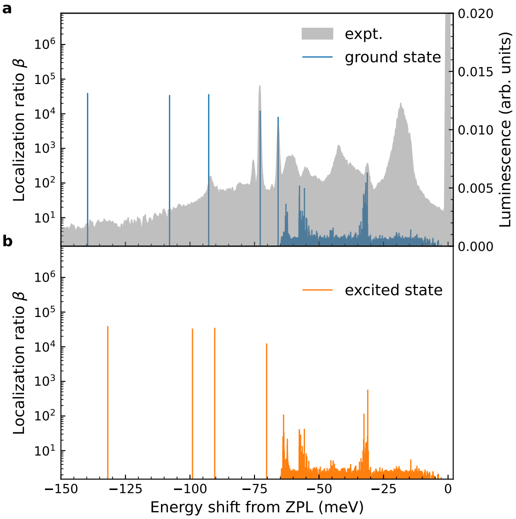

Figure 4.15: Vibrational structures of the **a** ground and **b** excited state of the C-center in silicon, compared with experimental luminescence data (gray). Blue and orange vertical lines correspond to localization ratios β of symmetric a' vibrational modes. Experimental data from Ref. [156].

a vibrational resonance. Quasi-localized modes at 32 meV, 54 meV, and 62 meV remain largely unchanged. This shift indicates significant quadratic electron–phonon interactions, which are beyond this study's scope.

The analysis shows that the C-center's optical sideband features can be characterized through vibrational modes. However, more detailed calculations of electron–phonon coupling during optical processes are needed to fully understand their effect on spectral lineshapes.

4.3.3.2 Electron–phonon coupling

Figure 4.16a presents the calculated spectral density of electron–phonon coupling for the emission process of the C-center in silicon, while Fig. 4.16b illustrates the spectral density for the absorption process.

The coupling to a' symmetry vibrational modes is represented by the spectral density $S(\hbar\omega) = \sum_k S_k \delta(\hbar\omega - \hbar\omega_k)$, where S_k denotes the HR factor for vibrational mode k. The total HR factor, $S_{\text{tot}} = \sum_k S_k$, is indicated in the respective panels. For luminescence, S_{tot} is 1.79, while for absorption, it is 1.82. This similarity suggests that the vibrational

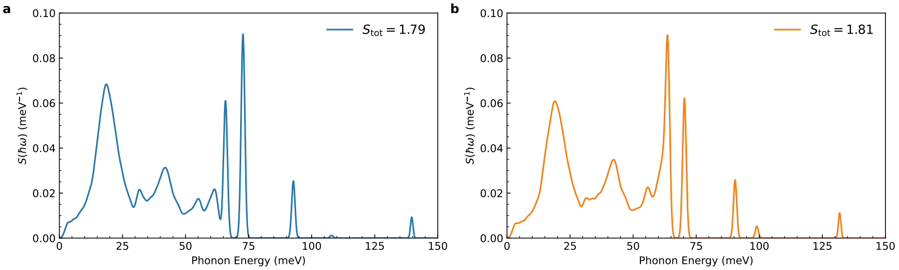

Figure 4.16: a Spectral function of electron–phonon coupling $S(\hbar\omega)$ during **a** luminescence and **b** absorption for C-center in silicon.

structures of the ground and excited states are closely matched in terms of phonon modes and energies.

In the luminescence process, significant contributions to emission arise from localized vibrational modes at 65.9 meV, 72.8 meV, and 92.7 meV. At higher energies, the coupling is negligible at 107.9 meV, with a more pronounced mode observed at 139.6 meV. The spectral function also reveals five distinct peaks below 65 meV. Peaks at 18.6 meV and 41.9 meV are attributed to the high density of bulk-like modes, while the remaining three peaks at 31.8 meV, 55.1 meV, and 61.5 meV originate from interactions with quasi-localized vibrational resonances.

For the absorption process, the electron–phonon coupling spectrum shows several differences. The localized mode near 70.3 meV becomes less pronounced, while a mode near 63.6 meV shifts downward in energy and transitions into a vibrational resonance overlapping with bulk-like modes. At higher energies, a localized mode appears at 90.4 meV and additional small peaks at 99.1 meV and 131.9 meV. Bulk-like modes at 19.0 meV and 42.2 meV remain largely unchanged, as do quasi-localized resonances at 31.5 meV and 55.9 meV. However, the quasi-localized resonance at 63.6 meV overlaps with the previously localized mode at 65.8 meV during luminescence, marking a notable distinction.

4.3.3.3 Optical lineshapes

The calculated emission lineshape (blue) in Fig. 4.17a shows excellent agreement with the experimental data reported in Ref. [156]. Key features in the theoretical spectrum, corresponding to different vibrational modes, align closely with the peaks observed in the experiment. The relative intensities of these features are also accurately captured. Localized modes at 65.9 meV, 72.8 meV, and 92.7 meV, along with resonances near 31.8 meV, 55.1 meV, and 61.5 meV below the ZPL, are well-reproduced in the theoretical lineshape, matching prominent experimental peaks. The contribution of bulk phonons is reflected in broad peaks around 19 meV and 42 meV from the ZPL. The total HR factor S_{tot} for emission is calculated as 1.79, with a DWF of approximately 20%.

Although the calculated emission spectrum exhibits excellent overall agreement with the experimental data, some discrepancies persist. The most notable is the absence of a sharp peak and its shoulder near 75.5 meV from the ZPL in the theoretical lineshape. The origin of this feature remains unclear and warrants further investigation.

Figure 4.17b displays the calculated absorption lineshape (in orange). A comparison of the absorption and emission lineshapes, reveals qualitative similarities within approximately 60 meV below the ZPL. Beyond this range, the peak energies in the absorption lineshape, influenced by localized modes, shift to lower values compared to their counterparts in the luminescence spectrum. Prominent localized modes at 70.3 meV, 90.4 meV, 99.1 meV, and 131.9 meV are clearly associated with the absorption process.

The difference in relative spectral weights between the luminescence and absorption lineshapes arises from the ω^{κ} prefactor in Eq. (2.88). For luminescence, with $\kappa = 3$, this prefactor amplifies the lineshape near the ZPL more significantly than in absorption, where $\kappa = 1$, creating a marked asymmetry between the spectra. In contrast, the asymmetry in the electron–phonon coupling functions $S(\hbar\omega)$ is less pronounced and stems solely from variations in vibrational modes between the ground and excited states.

4.4. Summary and conclusions

In this chapter, we explored electron–phonon coupling and its impact on the optical lineshapes of the NV^{-} center in diamond, neutral divacancies in 4H-SiC, and the C-center in silicon using *ab initio* methods. The primary objective was to evaluate the accuracy and efficiency of the SCAN family of functionals in modeling electron–phonon interactions and optical lineshapes, with comparisons against PBE, HSE06, and available

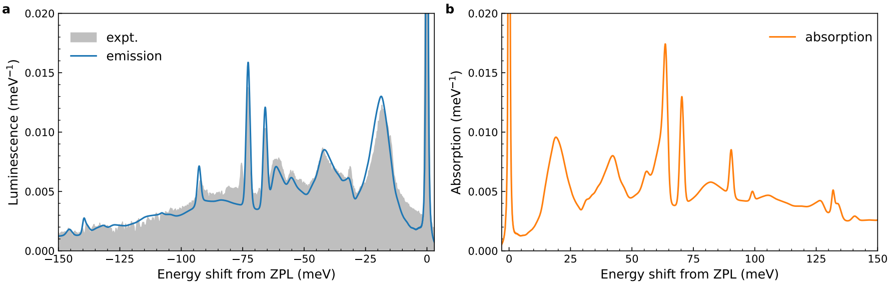

Figure 4.17: Optical spectra of **a** emission and **b** absorption for C-center in silicon. The gray area represents experimental data from Ref. [156].

experimental data. The key findings of this study are summarized as follows:

1. We benchmarked the SCAN, rSCAN, and r^{2}SCAN functionals for their performance in modeling electron–phonon coupling and luminescence lineshapes of the NV$^-$ center in diamond. Comparisons with PBE, HSE06, and experimental data demonstrate that the SCAN functionals achieve the best agreement with experimental spectra, accurately reproducing key features of the phonon sideband.

2. The SCAN family of functionals provides good accuracy while maintaining a computational cost comparable to the widely used PBE functional, making them a suitable choice for large-scale simulations and high-throughput defect screening.

3. The r^{2}SCAN functional was employed to investigate the ZPL energy, electron–phonon coupling, and luminescence lineshape of the NV$^-$ center in diamond under hydrostatic pressure. The observed pressure-dependent trends in electron–phonon coupling and the evolution of fine spectral features provide valuable insights that could facilitate the calibration of NV$^-$ centers under external perturbations.

4. The electron–phonon coupling and optical lineshapes of neutral divacancies in 4H-SiC were modeled using the r^{2}SCAN functional and compared with available experimental data. The computed

spectral densities accurately capture key phonon sideband features and reproduce the fine structure observed in the experimental luminescence spectra. The calculations reveal distinct differences in electron–phonon coupling strength and luminescence characteristics across the four divacancy configurations (*hh*, *kk*, *hk*, and *kh*), with the *kh* configuration exhibiting the highest Debye–Waller factor and the most pronounced ZPL contribution.

5. For the C-center in silicon, using SCAN functional we accurately reproduce the intricate luminescence lineshape with unprecedented accuracy, capturing the interplay of localized modes and bulk phonons and reinforcing the attribution of this optical line to the neutral $\mathrm{C_iO_i}$ complex.

Thesis Statement (II)

Regarding electron–phonon coupling during optical transitions, our findings show that SCAN family of functionals yields optical lineshapes that are in great agreement with the experiments while being computationally cost-effective.

Chapter 5

Optical lineshape modeling in Jahn–Teller systems: NiV^- center in diamond and divacancies in 4H-SiC

5.1. Introduction

This chapter presents our *ab initio* study of optical lineshapes influenced by the pronounced Jahn–Teller (JT) effect in the negatively charged nickel-vacancy (NiV^-) center in diamond and neutral axial divacancy defects in 4H-SiC. The primary objective of this study is to achieve accurate modeling of optical lineshapes through density functional theory (DFT) calculations that incorporate the dynamical Jahn–Teller (DJT) effect, which arises due to the electronic degeneracy present in these defects.

The content of this chapter is organized as follows. In Section 5.3.1, we present the results of the computed adiabatic potential energy surfaces (APES) for JT active ionic degrees of freedom and key parameters characterizing the JT coupling. Section 5.3.2 focuses on the NiV^- center in diamond. We begin by benchmarking the effective mode approximation and subsequent diagonalization of the JT Hamiltonian and then proceed to model the luminescence lineshape using a multimode DJT approach. The modeled lineshape is then compared with experimental data as well as with the lineshape obtained from the Huang–Rhys (HR) theory. Finally, Section 5.3.3 covers the optical properties of neutral axial divacancy defects in 4H-SiC. In this section, we similarly benchmark the diagonalization of the JT Hamiltonian and compare the computed luminescence and absorption lineshapes obtained using both DJT and HR approaches with available experimental spectra. The chapter concludes with a summary of the key findings, emphasizing the importance of accounting for JT effects in accurately modeling defect-related optical phenomena for systems with prominent JT coupling.

5.2. Methodology

5.2.1. Computational details

The calculations for the NiV^- center in diamond and neutral divacancy defects in 4H-SiC were conducted using spin-polarized density functional theory. The interaction between electrons and atomic cores was described using the PAW method with a plane-wave energy cutoff of 600 eV. All calculations were performed using the VASP code and the r^{2}SCAN functional [45, 63]. The Brillouin zone was sampled at the Γ-point using a single **k**-point. Defects were modeled using a supercell approach [143].

The NiV^- center in diamond was created by removing two neighboring carbon atoms and inserting a nickel atom midway between the two carbon vacancies in a $4 \times 4 \times 4$ supercell containing 512 atomic sites. Convergence criteria were set to 10^{-6} eV for the electronic self-consistent loop and 10^{-4} eV/Å for ionic relaxation.

Neutral divacancy defects in 4H-SiC were modeled by removing a silicon atom and a carbon atom from a $6 \times 6 \times 2$ supercell containing 576 atomic sites. The convergence criteria for these calculations were set to 10^{-8} eV for the electronic self-consistent loop and 10^{-4} eV/Å for ionic relaxation.

5.2.2. Calculation of adiabatic potential energy surfaces

To analyze JT distortions and their associated parameters, the APES was constructed through a series of first-principles calculations. The APES was modeled using a quadratic $E \otimes e$ vibronic coupling scheme, which captures the interaction between degenerate electronic states and vibrational modes of e-type symmetry. For the NiV^- center in diamond, we examined the lower branch of the ^2E_u state, while for the neutral axial divacancies in 4H-SiC, we focused on the APES of the lower branch of the excited triplet state ^3E, where electronic degeneracy is present.

The calculation of the APES involved two key steps: performing two separate geometry optimizations for both the NiV^- center in diamond and neutral axial divacancies in 4H-SiC. For the NiV^- center, the first optimization was carried out using the electronic configuration $a_{1g}^2 e_{ux}^{1.5} e_{uy}^{1.5}$, preserving the high-symmetry D_{3d} point group. In the second optimization, the system adopted the electronic configuration $a_{1g}^2 e_{ux}^2 e_{uy}^1$, resulting in relaxation along e symmetry degrees of freedom to a JT minimum with C_{2h} symmetry (as exemplified in Fig. 5.1). The displacements between the two relaxed geometries were used to determine the symmetry-breaking distortions for the NiV$^-$ center.

Similarly, for the neutral axial divacancies in 4H-SiC, the first optimization was conducted using the electronic configuration $a_1 e_x^{1.5} e_y^{1.5}$ while maintaining the high-symmetry C_{3v} point group. In the second optimization, the system was allowed to lower its symmetry by adopting the electronic configuration $a_1 e_x^2 e_y^1$, relaxing to a JT minimum with C_{1h} symmetry.

In both cases, the mass-weighted displacement ΔQ_{JT} between the two relaxed structures along the e-symmetry breaking mode was calculated to quantify the Jahn–Teller distortion.

To map the APES along the symmetry-breaking direction, new geometries were systematically generated by parametrizing the displacement path ΔQ_{JT} with a parameter q, where $q = 0$ corresponds to the high-symmetry configuration and $q = 1$ corresponds to the low-symmetry configuration. For the NiV$^-$ center, the displacements were applied along the e_{gx} component of the symmetry-breaking mode and projected using the irreducible representation matrices of the D_{3d} point group. Displacement factors q ranging from -1.4 to 1.4 in increments of 0.1 were used to cover a broad range of possible atomic configurations. These geometries were then used for single-point energy calculations with the electronic configuration $a_{1g}^2 e_{ux}^2 e_{uy}^1$.

Similarly, for the neutral axial divacancies in 4H-SiC, the displacements were applied along the e_x component of the symmetry-breaking mode and projected using the irreducible representation matrices of the C_{3v} point group. Displacement parameter q was varied from -1.5 to 1.5 in increments of 0.1. For the single-point calculations, the electronic configuration $a_1 e_x^2 e_y^1$ was employed.

For integral orbital occupations ($a_{1g}^2 e_{ux}^2 e_{uy}^1$ and $a_1 e_x^2 e_y^1$), the potential energy surface could not be directly evaluated at high-symmetry (D_{3d} or C_{3v}) geometries due to convergence issues arising from electronic degeneracy. However, the energy values obtained from the other configurations provided sufficient data to fit the APES using an effective Jahn–Teller potential that includes both linear and quadratic interaction terms [47]. The expression for the APES in mass-weighted polar coordinates is given by:

$$\epsilon(\rho, \phi) = \frac{1}{2}\kappa\rho^2 \pm \rho \left[F^2 + G^2\rho^2 + 2FG\rho\cos(3\phi)\right]^{1/2}, \qquad (5.1)$$

where $\rho = \sqrt{Q_x^2 + Q_y^2}$ represents the magnitude of the mass-weighted displacement, $\phi = \arctan(Q_y/Q_x)$ is the angular coordinate, κ is the elastic force constant, $F = \sqrt{2\omega^3}K$ is the linear vibronic coupling constant, and G is the quadratic vibronic coupling constant.

5.3. Results and discussion

5.3.1. Adiabatic potential energy surface

The ground doublet state ^2E_u of the NiV$^-$ center in diamond exhibits an orbital degeneracy between the configurations $a_{1g}^2 e_{ux}^1 e_{uy}^2$ and $a_{1g}^2 e_{ux}^2 e_{uy}^1$. This degeneracy induces a dynamical Jahn–Teller effect through interaction with vibrational modes of e_g symmetry. The coupling between electronic and vibrational states generates a complex set of vibronic states, which significantly influence the optical spectra. The corresponding adiabatic potential energy surface displays a characteristic “tricorn sombrero” shape, with three symmetry-breaking minima separated by low-energy barriers and barely visible saddle points (see Fig. 5.1), indicating that quadratic Jahn–Teller interactions are negligible.

Similarly, the excited triplet state ^3E of the neutral axial divacancies in 4H-SiC exhibits an orbital degeneracy described by the configurations $a_1 e_x^1 e_y^2$ and $a_1 e_x^2 e_y^1$. This degeneracy leads to a DJT effect through interaction with vibrational modes of e symmetry. The APES for these systems also shows the ”tricorn sombrero” shape but with three clearly distinct symmetry-breaking minima separated by saddle points (see Figures 5.2a and 5.3a).

The computed mass-weighted displacements ΔQ_{JT}, which quantify the Jahn–Teller distortion, were found to be 0.337 amu$^{0.5}$Å for the NiV$^-$ center, 0.519 amu$^{0.5}$Å for the *hh* divacancy, and 0.472 amu$^{0.5}$Å for the *kk* divacancy. The corresponding vibronic coupling parameters K, F, and G were extracted from the potential energy curves using Eq. (5.1). For the NiV$^-$ center, the values were determined to be $K = 1.078$ eV/Å^2, $F = 0.364$ eV/Å, and $G = 0.012$ eV/Å^2. In the case of the *hh* divacancy, the parameters were $K = 0.641$ eV/Å^2, $F = 0.266$ eV/Å, and $G = 0.064$ eV/Å^2, while for the *kk* divacancy, they were $K = 0.701$ eV/Å^2, $F = 0.272$ eV/Å, and $G = 0.061$ eV/Å^2. These results indicate that the neutral axial divacancies exhibit significantly larger quadratic vibronic coupling constants, suggesting a more pronounced quadratic JT effect compared to the NiV$^-$ center.

The stabilization energy, E_{JT}, was calculated as the energy difference between the high-symmetry and distorted configurations. For the NiV$^-$ center, E_{JT} was found to be 62.9 meV, whereas for the *hh* and *kk* divacancies, it was 69.2 meV and 63.7 meV, respectively. The corresponding JT barriers, δ_{JT}, were 2.9 meV for the NiV$^-$ center, and 23.1 meV and 18.9 meV for the *hh* and *kk* divacancies, respectively. These values align well with previous theoretical studies that employed the hybrid HSE06 functional, reporting a stabilization energy of 72.4 meV and a barrier height of 2.4 meV for the NiV$^-$ center [132], and a stabilization energy of 74 meV with a barrier height of 18 meV for the *hh* divacancy [157].

Contour plots of the APES for both defect systems are shown in Figures 5.1b, 5.2b, and 5.3b. These plots illustrate the potential energy landscapes and the paths used to compute the potential energy curves displayed in Figures 5.1c, 5.2c, and 5.3c, respectively. These paths were used to parametrize the Jahn–Teller relaxation and extract key vibronic coupling parameters.

The results confirm that both the NiV$^-$ center and the neutral axial divacancies undergo dynamic distortions along symmetry-breaking directions, resulting in the characteristic multi-minima APES. However, the divacancies exhibit substantially higher JT barriers and more pronounced quadratic coupling compared to the NiV$^-$ center.

For basal divacancies, the excited states are not degenerate but are separated by small energy gaps. For instance, the energy separation between the excited states of the *hk* divacancy is 62 meV, while for the *kh* divacancy, it is 100 meV. This suggests the presence of a pseudo-Jahn–Teller (PJT) effect, where symmetry-breaking vibrational modes couple with electronic states that are close in energy. In static calculations, this effect modifies the harmonic potential, altering the effective frequency of PJT-active modes or, in cases of strong coupling, producing double minima and breaking the symmetry.

Our calculations indicate that the *kh* divacancy undergoes a

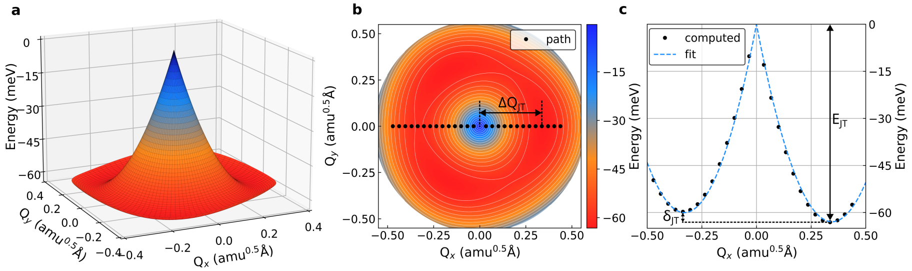

Figure 5.1: **a** APES of the lower branch of the ^2E_u state of NiV$^-$ center in diamond. Q_x, Q_y configuration coordinates represent the collective motion of effective e_g-symmetry modes. $E_{\rm JT}$ is the JT stabilization energy, which is the difference in energy between the high-symmetry and distorted configurations. The three minima are separated by three barriers with the energy of $\delta_{\rm JT}$. **b** Contour plot of the APES. **c** Computed potential energy curve along the path defined in **b**.

symmetry-breaking distortion, gaining a stabilization energy of 15 meV, while the *hk* divacancy does not exhibit such behavior, suggesting weaker PJT coupling. A detailed analysis of electron–phonon coupling parameters is necessary to fully understand the PJT effect in these systems. However, for the emission process, the non-adiabatic nature of the PJT effect can be approximated using the HR theory [81], which treats the final state as effectively adiabatic. Nonetheless, further investigation is required to rigorously address the absorption spectra, which is left for future work.

5.3.2. NiV$^-$ center in diamond

5.3.2.1 Electron–phonon coupling

To determine the vibrational structure of the ground state and relaxation profiles necessary for calculating electron–phonon coupling parameters associated with both HR and JT couplings, we applied the embedding methodology outlined in Section 2.6. This methodology facilitated the construction of a large $18 \times 18 \times 18$ supercell containing 46 655 atomic sites. Using this methodology, we computed spectral densities for two types of couplings: the HR coupling for modes with a_{1g} symmetry, denoted as $S_{a_{1g}}(\hbar\omega)$, and the linear JT coupling for modes with e_g sym-

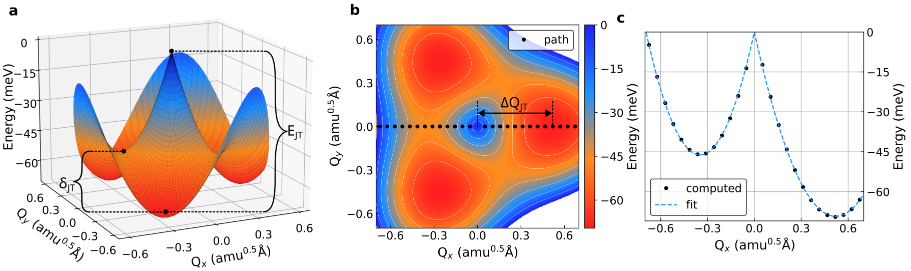

Figure 5.2: **a** APES of the lower branch of the ^3E state of *hh*-VV^0 defect in 4H-SiC. Q_x, Q_y configuration coordinates represent the collective motion of effective *e*-symmetry modes. E_{JT} is the JT stabilization energy, which is the difference in energy between the high-symmetry and distorted configurations. The three minima are separated by three barriers with the energy of δ_{JT}. **b** Contour plot of the APES. **c** Computed potential energy curve along the path defined in **b**.

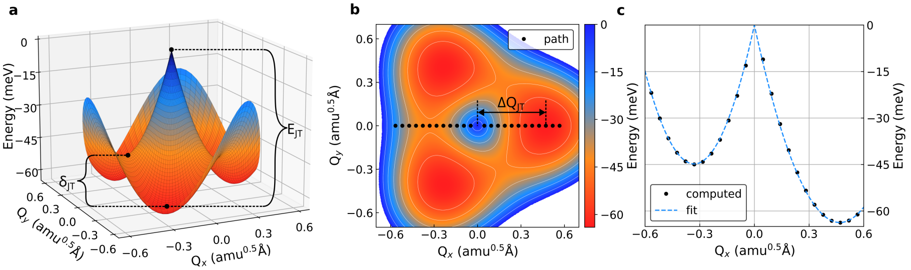

Figure 5.3: **a** APES of the lower branch of the ^3E state of *kk*-VV^0 defect in 4H-SiC. Q_x, Q_y configuration coordinates represent the collective motion of effective *e*-symmetry modes. E_{JT} is the JT stabilization energy, which is the difference in energy between the high-symmetry and distorted configurations. The three minima are separated by three barriers with the energy of δ_{JT}. **b** Contour plot of the APES. **c** Computed potential energy curve along the path defined in **b**.

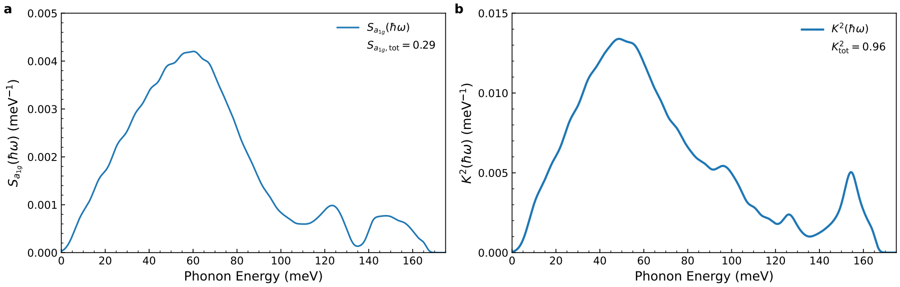

Figure 5.4: **a** Spectral densities $S_{a_{1g}}(\hbar\omega)$ associated with a_{1g}-symmetry phonons during luminescence in the case of the NiV$^-$ center in diamond. **b** Spectral densities of JT linear coupling $K^2(\hbar\omega)$ associated with e_g-symmetry phonons during luminescence.

metry, expressed as $K^2(\hbar\omega)$. To achieve a continuous representation of the electron–phonon interaction, we approximated the delta functions by Gaussian functions with a variable width σ, which decreases linearly from 3.6 meV at $\omega = 0$ to 1.5 meV at the maximum phonon energy. These results are visualized in Fig. 5.4, where panel **a** illustrates the HR spectral density $S_{a_{1g}}(\hbar\omega)$, and panel **b** shows the JT linear coupling spectral density $K^2(\hbar\omega)$. Both panels also include cumulative values: the total HR parameter, $S_{a_{1g},\mathrm{tot}} = \sum_k S_{a_{1g},k}$, and the total linear JT coupling, $K^2_{\mathrm{tot}} = \sum_k K^2_k$. The computed total HR coupling was $S_{a_{1g},\mathrm{tot}} = 0.29$, whereas the total linear JT coupling was significantly stronger, with $K^2_{\mathrm{tot}} = 0.96$.

The parameters $S_{a_{1g},k}$ and K^2_k represent contributions to changes in the adiabatic potential energy surface and are directly linked to relaxation energies. The relaxation energy in the symmetry-preserving direction following a vertical transition from the A to E state is given by $\Delta E_{a_{1g}} = \sum_k \hbar\omega_k S_{a_{1g},k}$. In contrast, the JT relaxation energy, $\Delta E_{\mathrm{JT}} = \sum_k \hbar\omega_k K^2_k$, describes the system's progression along the e_g symmetry coordinate from a high-symmetry structure to a distorted low-symmetry configuration with minimized energy. Our calculations yield $\Delta E_{a_{1g}} = 18.8$ meV and $\Delta E_{\mathrm{JT}} = 63.5$ meV, indicating a pronounced contribution of the JT effect to the overall electron–phonon interaction.

5.3.2.2 Benchmarking the diagonalization of the Jahn–Teller Hamiltonian

Diagonalizing the JT Hamiltonian, which accounts for multiple vibrational modes, poses significant computational challenges due to the large matrix sizes involved. To address this, we adopt an effective mode approximation strategy, as detailed in Section 2.5.2. This method approximates the spectral function of linear JT coupling, $K^2(\hbar\omega) = \sum_k K_k^2 \delta(\hbar\omega - \hbar\omega_k)$, by using an effective representation, $K_{\text{eff}}^2(\hbar\omega) = \sum_{n=1}^{N_{\text{eff}}} K_n^2 g_\sigma(\hbar\omega_n - \hbar\omega)$, where g_σ is a Gaussian function with a width σ.

This approximation introduces N_{eff} effective vibrational modes, each defined by a frequency ω_n and a vibronic coupling strength K_n^2. The parameters K_n^2, ω_n, and σ are optimized to ensure that $K_{\text{eff}}^2(\hbar\omega)$ closely reproduces $K^2(\hbar\omega)$, thereby capturing the key features of the full vibrational spectrum. This reduction to a limited number of effective modes, significantly reduces the computational cost of diagonalization while maintaining the accuracy of the spectral function.

The convergence of this approximation is demonstrated in Fig. 5.5, which shows the convergence of effective linear JT coupling $K_{\text{eff}}^2(\hbar\omega)$ towards $K^2(\hbar\omega)$ as N_{eff} increases for the luminescence of NiV$^-$ center in diamond.

We investigated the convergence of the computed emission lineshapes for the $^2A_{1g} \to {}^2E_u$ optical transition, with a focus on the parameters defining the JT Hamiltonian basis. The theoretical approach for modeling vibronic broadening in $A \to E$ transitions and the treatment of multi-mode $E \otimes (e \oplus e \oplus \cdots)$ JT systems is detailed in Section 2.5.2. To assess the impact of basis size on the resulting spectra, we analyzed the effects of varying the number of effective modes, N_{eff}, and the total number of excited phonons, n_{tot}.

Our findings indicate that a basis with $N_{\text{eff}} = 12$ sufficiently reproduces the experimental lineshape, as shown in Fig. 5.6a. However, to achieve higher precision, we opted for a more comprehensive basis by employing $N_{\text{eff}} = 18$ number of effective modes. The convergence behavior of the normalized luminescence lineshapes with respect to the total number of excited phonons is presented in Fig. 5.6b. These results demonstrate that including $n_{\text{tot}} = 5$ excited phonons is sufficient to achieve convergence for the NiV$^-$ center in diamond.

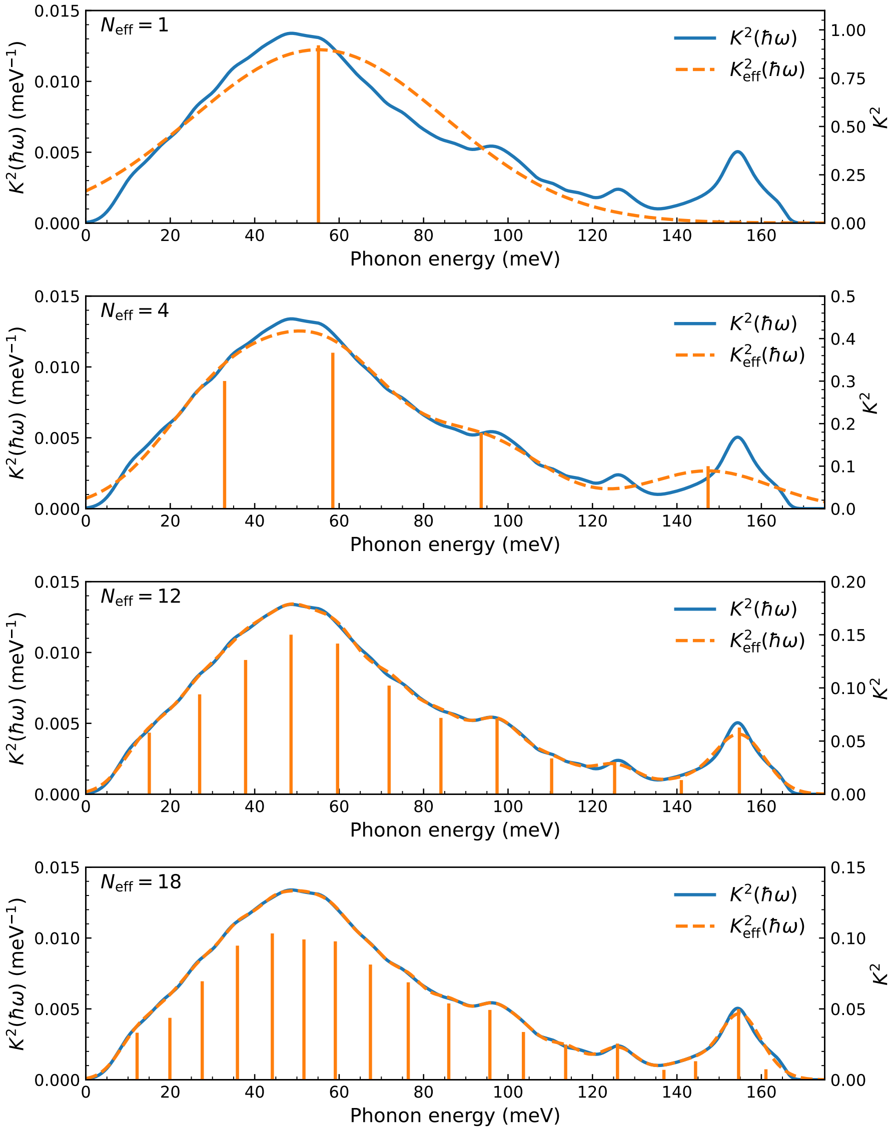

Figure 5.5: Convergence of effective linear JT coupling $K^2_{\text{eff}}(\hbar\omega)$ towards $K^2(\hbar\omega)$ with increasing number of effective modes N_{eff} for NiV$^-$ center in diamond during emission. Orange stems represent effective modes with their respective frequencies and coupling strengths K^2_n.

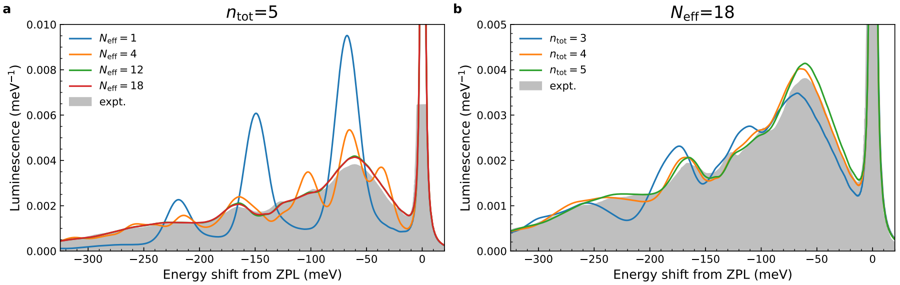

Figure 5.6: **a** Convergence of the theoretical normalized luminescence lineshapes for the NiV$^-$ center in diamond, calculated using DJT theory, as a function of the number of effective modes $N_{\rm eff}$. Each lineshape was computed with a fixed total number of excited phonons, $n_{\rm tot} = 5$. **b** Convergence of the theoretical normalized emission lineshapes for the NiV$^-$ center in diamond, calculated using DJT theory, as a function of the total number of excited phonons $n_{\rm tot}$. Each lineshape was computed with a fixed number of effective modes, $N_{\rm eff} = 18$. Experimental spectrum in gray from Ref. [131], recorded at 77 K.

5.3.2.3 Optical spectra of emission

The luminescence lineshapes calculated using both HR and DJT theories are presented in Fig. 5.7, along with the experimental spectrum from Ref. [131], measured at 77 K. While the HR-based lineshape (blue curve) aligns with previous theoretical predictions from Ref. [132], it fails to replicate the experimental trend, particularly missing key features influenced by strong JT interactions. This discrepancy highlights the limitations of the HR approach in capturing optical transitions dominated by JT effects. In contrast, the lineshape generated using the multimode DJT framework (red curve in Fig. 5.7) exhibits excellent agreement with the experimental data, accurately reproducing all major spectral features and capturing the redistribution of intensity.

The DWF, calculated by integrating the ZPL region and expressed as the ratio of ZPL intensity to the total emission lineshape, is estimated at 35% for the HR theory and 41% for the DJT model. The DJT method predicts a higher ZPL intensity with a more extended phonon sideband compared to HR theory, reflecting a more accurate description of electron–phonon coupling in systems with significant JT interactions.

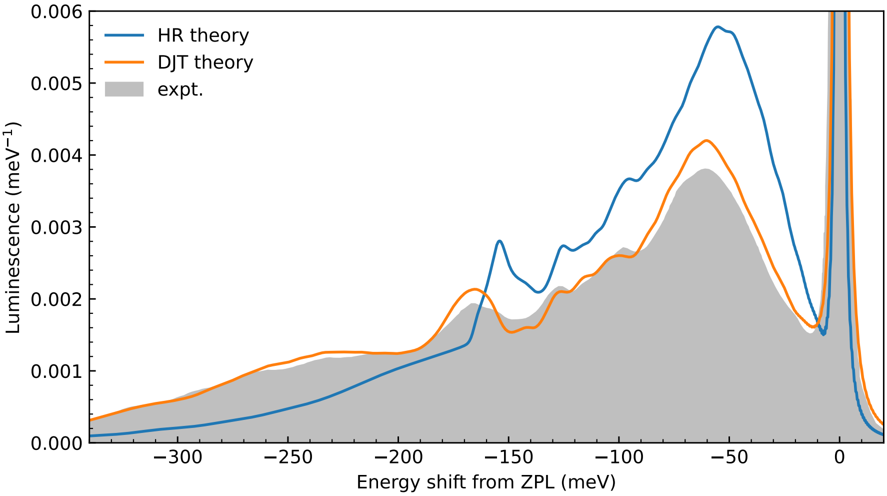

Figure 5.7: Theoretical normalized luminescence lineshapes for the NiV$^-$ center in diamond calculated using HR theory (blue line) and DJT theory (orange line). Results are for $18 \times 18 \times 18$ supercell. Experimental spectrum in gray from Ref. [131], recorded at 77 K.

5.3.3. Neutral axial divacancies in 4H-SiC

5.3.3.1 Electron–phonon coupling

Spectral densities of electron–phonon coupling, along with the corresponding computational details, were previously discussed in Section 4.3.2.1 and shown in Fig. 4.10. Panel **a** presents the HR spectral density $S_{a_1}(\hbar\omega)$, while panel **b** depicts the linear JT coupling spectral density $K^2(\hbar\omega)$ during the emission process. Panels **c** and **d** show the corresponding spectral densities for the absorption process.

During the absorption process, the relaxation energies are $\Delta E_{a_1} = 74.2$ meV for the *hh* divacancy and 76.5 meV for the *kk* divacancy. This indicates that the contribution from JT-active modes to the electron–phonon coupling, with stabilization energies of $\Delta E_{\mathrm{JT}} = 84.5$ meV for *hh* and 75.8 meV for *kk*, is comparable to that from symmetry-preserving modes.

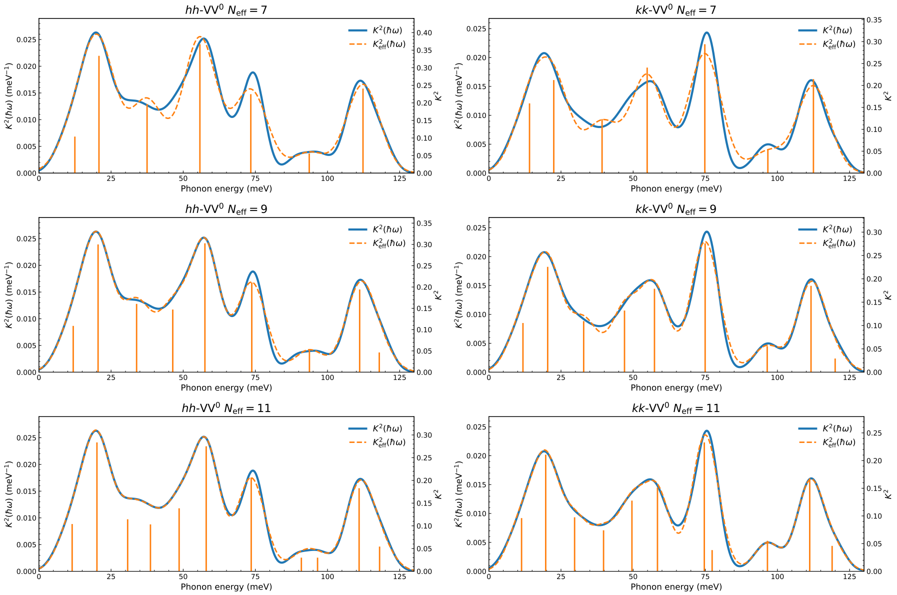

Figure 5.8: Convergence of linear JT coupling $K^2_{\text{eff}}(\hbar\omega)$ towards $K^2(\hbar\omega)$ with increasing number of effective modes N_{eff} for neutral axial vacancies (*hh*-VV^0 on the left and *kk*-VV^0 on the right) in 4H-SiC during absorption. Orange stems represent effective modes with their respective frequencies and coupling strengths K_n^2.

5.3.3.2 Benchmarking the diagonalization of the Jahn–Teller Hamiltonian

We benchmark the diagonalization of the Jahn–Teller Hamiltonian for axial divacancies *hh*-VV^0 and *kk*-VV^0 in 4H-SiC using the same methodology as described in detail in Section 2.5.2 and demonstrated for the NiV$^-$ center in diamond (see Section 5.3.2.2).

Figure 5.8 illustrates the convergence of $K^2_{\text{eff}}(\hbar\omega)$ toward the full vibrational spectrum, $K^2(\hbar\omega)$, for the *hh*-VV^0 and *kk*-VV^0 defects. The results demonstrate that $N_{\text{eff}} = 9$ is sufficient to capture the key features of the vibronic coupling spectrum for both axial divacancies.

Furthermore, Fig. 5.9 highlights the impact of increasing the number of effective modes on the absorption lineshapes, while Fig. 5.10 presents the convergence with respect to the total number of excited phonons included in the phonon basis. Our findings indicate that using $N_{\text{eff}} = 9$ and $n_{\text{tot}} = 6$ yields converged absorption lineshapes for both *hh*-VV^0 and *kk*-VV^0 in 4H-SiC.

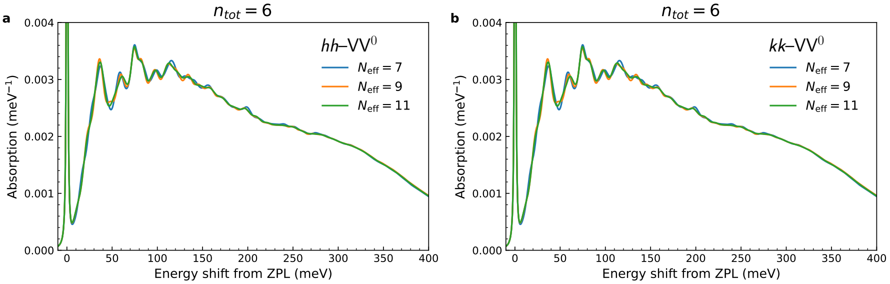

Figure 5.9: Convergence of the theoretical normalized absorption lineshapes for axial divacancies in 4H-SiC calculated using dynamical Jahn–Teller theory with respect to the number of effective modes N_{eff}. The total number of excited phonons used for each lineshape was $n_{\text{tot}} = 6$.

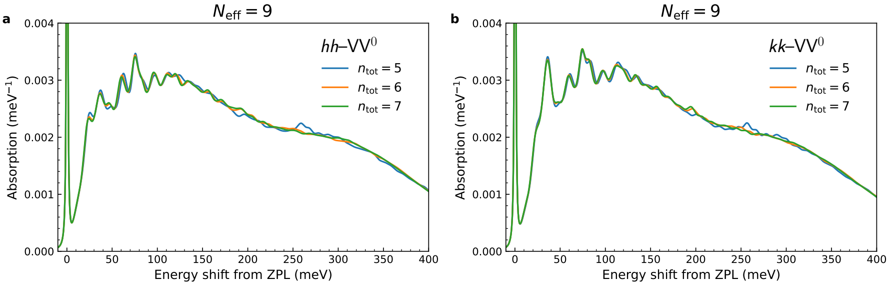

Figure 5.10: Convergence of the theoretical normalized absorption lineshapes for axial divacancies in 4H-SiC calculated using dynamical Jahn–Teller theory with respect to the number of excited phonons n_{tot}. The total number of effective modes used for each lineshape was $N_{\text{eff}} = 9$.

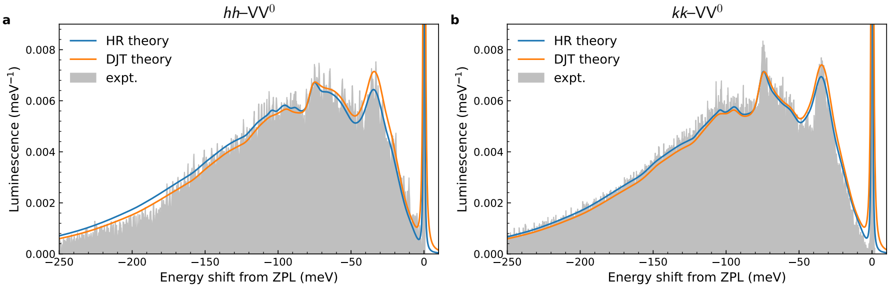

Figure 5.11: Optical spectra of emission for neutral axial divacancy centers in 4H-SiC. Blue lines are luminescence lineshapes calculated using HR theory, while the orange lines are lineshapes calculated using DJT theory. Results are for a 23 × 23 × 7 supercell. The gray area represents experimental data from Ref. [102].

5.3.3.3 Optical spectra of emission

The calculated optical emission lineshapes corresponding to the $^3E \rightarrow {}^3A_2$ transition, modeled using both HR theory and multimode DJT theory for axial divacancies, are presented in Fig. 5.11 alongside experimental spectra shown in gray [102]. The intensities of the experimental lineshapes have been scaled to match the peaks of the computed lineshapes. The theoretical results were extrapolated to the dilute limit using a $23 \times 23 \times 7$ supercell containing 29 622 atomic sites using force constant embedding methodology outlined in Section 2.6. Both approaches show excellent agreement with experimental data, successfully capturing all major spectral features.

The similarity between the emission lineshapes generated by the HR and DJT theories aligns with the findings of Ref. [34], which demonstrated that for an $^3E \rightarrow {}^3A_2$ optical transition with $K^2_{\mathrm{tot}} \approx 1$, the HR theory provides a description comparable to the more rigorous DJT theory. The main difference between the lineshapes lies in the intensity distribution. Specifically, the DJT theory predicts a more pronounced ZPL and, consequently, a higher DWF.

The DWFs obtained from the HR theory are 5.60% and 6.82% for the *hh*-VV^0 and *kk*-VV^0 defects in 4H-SiC, respectively. In comparison, the DWFs calculated using the multimode DJT approach are 7.04% and 7.03%, which deviate further from the experimental values of 3.69% and 6.11% [102].

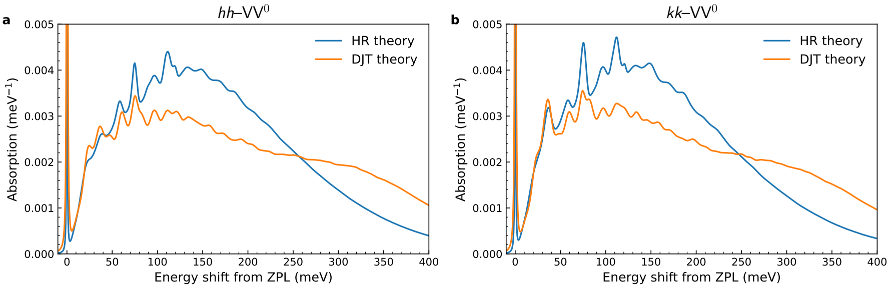

Figure 5.12: Optical spectra of absorption for neutral axial divacancy centers in 4H-SiC. Blue lines are absorption lineshapes calculated using HR theory, while the orange lines are absorption lineshapes calculated using DJT theory. Results are for a 23 × 23 × 7 supercell.

5.3.3.4 Optical spectra of absorption

The absorption lineshapes corresponding to the ${}^3A_2 \to {}^3E$ optical transition for axial divacancies, calculated using both HR and multimode DJT approaches, are shown in Fig. 5.12. When comparing the two theoretical approaches, the DJT theory predicts a more prominent ZPL intensity along with broader phonon sidebands compared to HR theory. This difference becomes especially noticeable beyond 250 meV above the ZPL. Across all absorption spectra, sharp features near 75 meV are attributed to quasi-localized phonon modes.

The DWFs calculated using HR theory are 2.53% for the hh configuration and 3.02% for the kk configuration. In comparison, the DWFs obtained from the DJT approach are slightly higher, with values of 3.42% and 3.72% for the hh and kk divacancies, respectively.

The comparison of absorption lineshapes and DWFs is not provided due to the absence of experimental PLE spectra. However, we expect a similar behavior to the luminescence lineshape of the NiV$^-$ center in diamond, which also exhibits a pronounced Jahn–Teller effect during an optical transition where the final state is degenerate.

5.4. Summary and conclusions

In this chapter, we investigated the optical lineshapes influenced by prominent Jahn–Teller effect for two defect systems: NiV$^-$ center in diamond and neutral axial divacancies in 4H-SiC. Using *ab initio* methods and the r^{2}SCAN functional, we modeled the optical emission and absorption spectra through both HR and DJT theories, focusing on the importance of vibronic interactions. The key achievements of this study are summarized as follows:

1. We computed the adiabatic potential energy surfaces and confirmed that the JT effect plays a key role in the ground state of the NiV$^-$ center in diamond and the excited state of axial divacancies in 4H-SiC. These defects exhibit strong vibronic coupling, necessitating the use of multimode DJT theory for accurate lineshape modeling.

2. We demonstrated that the effective mode approximation is a reliable method to reduce the computational cost of diagonalizing the JT Hamiltonian while preserving the accuracy of the spectral functions.

3. The DJT theory substantially improves the agreement between computed and experimental luminescence lineshapes of the NiV$^-$ center in diamond, capturing key spectral features that are missed by the HR approach. This validates the effectiveness of the multimode DJT methodology for systems with strong JT coupling and highlights its importance for accurate modeling of defect-related optical properties.

Thesis Statement (III)

Employing a novel multi-mode Jahn–Teller computational methodology together with the r^{2}SCAN functional, we accurately captured the optical features arising from Jahn–Teller interactions in the photoluminescence spectra of split nickel-vacancy center in diamond, thereby demonstrating the functional's performance in determining vibronic-coupling constants.

Bibliography

[T1] Maciaszek, M. *et al.* The application of the SCAN density functional to color centers in diamond. *J. Chem. Phys.* **159**, 084708 (2023).

[T2] Silkinis, R. *et al.* Optical lineshapes for orbital singlet to doublet transitions in a dynamical Jahn–Teller system: the NV^- center in diamond. *Phys. Rev. B* **110**, 075303 (2024).

[T3] Silkinis, R. *et al.* Optical lineshapes of the C center in silicon from *ab initio* calculations: Interplay of localized modes and bulk phonons. *Phys. Rev. B* **111**, 125136 (2025).

[T4] Žalandauskas, V. *et al.* Theory of the divacancy in 4H–SiC: Impact of Jahn–Teller effect on optical properties. *npj Computational Materials*, accepted (2025). URL https://arxiv.org/abs/2412.01390.

[1] Ladd, T. D. *et al.* Quantum computers. *Nat.* **464**, 45–53 (2010).

[2] Weber, J. R. *et al.* Quantum computing with defects. *Proc. Natl. Acad. Sci.* **107**, 8513–8518 (2010).

[3] Bradley, C. E. *et al.* A ten-qubit solid-state spin register with quantum memory up to one minute. *Physical Review X* **9**, 031045 (2019).

[4] Pezzagna, S. & Meijer, J. Quantum computer based on color centers in diamond. *Appl. Phys. Rev.* **8**, 011308 (2021).

[5] Gisin, N. & Thew, R. Quantum communication. *Nat. Photonics* **1**, 165–171 (2007).

[6] Al-Juboori, A. *et al.* Quantum key distribution using a quantum emitter in hexagonal boron nitride. *Adv. Quantum Tech.* **6**, 2300038 (2023).

[7] Le Sage, D. *et al.* Optical magnetic imaging of living cells. *Nat.* **496**, 486–489 (2013).

[8] Rondin, L. *et al.* Magnetometry with nitrogen-vacancy defects in diamond. *Rep. Prog. Phys.* **77**, 056503 (2014).

[9] Degen, C. L., Reinhard, F. & Cappellaro, P. Quantum sensing. *Rev. Mod. Phys.* **89**, 035002 (2017).

[10] Vindolet, B. *et al.* Optical properties of SiV and GeV color centers in nanodiamonds under hydrostatic pressures up to 180 GPa. *Phys. Rev. B* **106**, 214109 (2022).

[11] Aharonovich, I., Englund, D. & Toth, M. Solid-state single-photon emitters. *Nature Photonics* **10**, 631–641 (2016).

[12] Childress, L. & Hanson, R. Diamond NV centers for quantum computing and quantum networks. *MRS Bulletin* **38**, 134 (2013).

[13] Doherty, M. W. *et al.* The nitrogen-vacancy colour centre in diamond. *Physics Reports* **528**, 1–45 (2013).

[14] Bar-Gill, N., Pham, L. M., Jarmola, A., Budker, D. & Walsworth, R. L. Solid-state electronic spin coherence time approaching one second. *Nature communications* **4**, 1–6 (2013).

[15] Herbschleb, E. *et al.* Ultra-long coherence times amongst room-temperature solid-state spins. *Nature communications* **10**, 3766 (2019).

[16] Widmann, M. *et al.* Coherent control of single spins in silicon carbide at room temperature. *Nature Materials* **14**, 164–168 (2015).

[17] Castelletto, S. *et al.* A silicon carbide room-temperature single-photon source. *Nature Materials* **13**, 151–156 (2014).

[18] Christle, D. J. *et al.* Isolated electron spins in silicon carbide with millisecond coherence times. *Nature Materials* **14**, 160–163 (2015).

[19] Awschalom, D. D., Hanson, R., Wrachtrup, J. & Zhou, B. B. Quantum technologies with optically interfaced solid-state spins. *Nature Photonics* **12**, 516–527 (2018).

[20] Bathen, M. E. & Vines, L. Manipulating single-photon emission from point defects in diamond and silicon carbide. *Advanced Quantum Technologies* **4**, 2100003 (2021).

[21] Anderson, C. P. *et al.* Five-second coherence of a single spin with single-shot readout in silicon carbide. *Science advances* **8**, eabm5912 (2022).

[22] Hollenbach, M., Berencén, Y., Kentsch, U., Helm, M. & Astakhov, G. V. Engineering telecom single-photon emitters in silicon for scalable quantum photonics. *Opt. Express* **28**, 26111–26121 (2020).

[23] Redjem, W. *et al.* Single artificial atoms in silicon emitting at telecom wavelengths. *Nat. Electron.* **3**, 738–743 (2020).

[24] Durand, A. *et al.* Broad diversity of near-infrared single-photon emitters in silicon. *Phys. Rev. Lett.* **126**, 083602 (2021).

[25] Buckley, S. M. *et al.* Optimization of photoluminescence from W centers in silicon-on-insulator. *Opt. Express* **28**, 16057–16072 (2020).

[26] Baron, Y. *et al.* Detection of single W-centers in silicon. *ACS Photonics* **9**, 2337–2345 (2022).

[27] Dhaliah, D., Xiong, Y., Sipahigil, A., Griffin, S. M. & Hautier, G. First-principles study of the T center in silicon. *Phys. Rev. Materials* **6**, L053201 (2022).

[28] Martin, R. M. *Electronic structure. Basic theory and practical methods* (Cambridge University Press, 2004).

[29] Perdew, J. P., Burke, K. & Ernzerhof, M. Generalized gradient approximation made simple. *Physical Review Letters* **77**, 3865 (1996).

[30] Heyd, J., Scuseria, G. E. & Ernzerhof, M. Hybrid functionals based on a screened coulomb potential. *The Journal of Chemical Physics* **118**, 8207–8215 (2003).

[31] Perdew, J. P. & Levy, M. Physical content of the exact Kohn-Sham orbital energies: Band gaps and derivative discontinuities. *Physical Review Letters* **51**, 1884–1887 (1983).

[32] Garza, A. J. & Scuseria, G. E. Predicting band gaps with hybrid density functionals. *The Journal of Physical Chemistry Letters* **7**, 4165–4170 (2016).

[33] Davidsson, J., Ivády, V., Armiento, R. & Abrikosov, I. A. ADAQ: Automatic workflows for magneto-optical properties of point defects in semiconductors. *Computer Physics Communications* **269**, 108091 (2021).

[34] Razinkovas, L., Doherty, M. W., Manson, N. B., Van de Walle, C. G. & Alkauskas, A. Vibrational and vibronic structure of isolated point defects: The nitrogen-vacancy center in diamond. *Physical Review B* **104**, 045303 (2021).

[35] Sun, J., Ruzsinszky, A. & Perdew, J. P. Strongly constrained and appropriately normed semilocal density functional. *Physical Review Letters* **115**, 036402 (2015).

[36] Tran, F., Stelzl, J. & Blaha, P. Rungs 1 to 4 of DFT Jacob's ladder: Extensive test on the lattice constant, bulk modulus, and cohesive energy of solids. *The Journal of Chemical Pphysics* **144**, 204120 (2016).

[37] Isaacs, E. B. & Wolverton, C. Performance of the strongly constrained and appropriately normed density functional for solid-state materials. *Physical Review Materials* **2**, 063801 (2018).

[38] Payne, M. C., Teter, M. P., Allan, D. C., Arias, T. A. & Joannopoulos, J. D. Iterative minimization techniques for ab initio total-energy calculations: molecular dynamics and conjugate gradients. *Reviews of Modern Physics* **64**, 1045–1097 (1992).

[39] Yang, J. H., Kitchaev, D. A. & Ceder, G. Rationalizing accurate structure prediction in the meta-GGA SCAN functional. *Physical Review B* **100**, 035132 (2019).

[40] Rauch, T., Munoz, F., Marques, M. A. L. & Botti, S. Defect levels from SCAN and MBJ meta-GGA exchange-correlation potentials. *Physical Review B* **104**, 064105 (2021).

[41] Lafargue-Dit-Hauret, W., Allix, M., Viana, B., Jobic, S. & Latouche, C. Computational analysis on native and extrinsic point defects in yag using the metagga scan method. *Theoretical Chemistry Accounts* **141**, 58 (2022).

[42] Ivanov, A. I., Schmerwitz, Y. L. A., Levi, G. & Jónsson, H. Electronic excitations of the charged nitrogen-vacancy center in diamond obtained using time-independent variational density functional calculations. *arXiv preprint arXiv:2303.03838* (2023).

[43] Abbas, G., Bulancea-Lindvall, O., Davidsson, J., Armiento, R. & Abrikosov, I. A. Theoretical characterization of nv-like defects in 4h-sic using adaq with the scan and r2scan meta-gga functionals (2025). URL https://arxiv.org/abs/2501.07289. 2501.07289.

[44] Bartók, A. P. & Yates, J. R. Regularized SCAN functional. *The Journal of Chemical Physics* **150**, 161101 (2019).

[45] Furness, J. W., Kaplan, A. D., Ning, J., Perdew, J. P. & Sun, J. Accurate and numerically efficient r^{2}SCAN meta-generalized gra-

dient approximation. *The Journal of Physical Chemistry Letters* **11**, 8208–8215 (2020).

[46] Azumi, T. & Matsuzaki, K. What does the term “vibronic coupling” mean? *Photochemistry and Photobiology* **25**, 315–326 (1977).

[47] Bersuker, I. B. & Polinger, V. Z. *Vibronic Interactions in Molecules and Crystals* (Springer, Berlin, 2012).

[48] Hohenberg, P. & Kohn, W. Inhomogeneous electron gas. *Phys. Rev.* **136**, B864 (1964).

[49] Kohn, W. & Sham, L. J. Self-consistent equations including exchange and correlation effects. *Physical Review* **140**, A1133 (1965).

[50] Perdew, J. P. & Schmidt, K. Jacob’s ladder of density functional approximations for the exchange-correlation energy. In *AIP Conference Proceedings*, vol. 577, 1–20 (American Institute of Physics, 2001).

[51] Dirac, P. A. Note on exchange phenomena in the thomas atom. In *Mathematical proceedings of the Cambridge philosophical society*, vol. 26, 376–385 (Cambridge University Press, 1930).

[52] Ceperley, D. M. & Alder, B. J. Ground state of the electron gas by a stochastic method. *Physical review letters* **45**, 566 (1980).

[53] Jones, R. O. & Gunnarsson, O. The density functional formalism, its applications and prospects. *Reviews Modern Physics* **61**, 689 (1989).

[54] Langreth, D. C. & Mehl, M. Beyond the local-density approximation in calculations of ground-state electronic properties. *Physical Review B* **28**, 1809 (1983).

[55] Becke, A. D. Density-functional exchange-energy approximation with correct asymptotic behavior. *Physical review A* **38**, 3098 (1988).

[56] Perdew, J. P., Burke, K. & Ernzerhof, M. Generalized gradient approximation made simple. *Phys. Rev. Lett.* **77**, 3865 (1996).

[57] Mejía-Rodríguez, D. & Trickey, S. Comment on “Regularized SCAN functional”. *The Journal of Chemical Physics* **151**, 207101 (2019).

[58] Bartók, A. P. & Yates, J. R. Response to "Comment on 'Regularized SCAN functional'"[J. Chem. Phys. 151, 207101 (2019)]. *The Journal of Chemical Physics* **151**, 207102 (2019).

[59] Becke, A. D. A new mixing of hartree–fock and local density-functional theories. *The Journal of chemical physics* **98**, 1372–1377 (1993).

[60] Becke, A. D. Density-functional thermochemistry. i. the effect of the exchange-only gradient correction. *The Journal of chemical physics* **96**, 2155–2160 (1992).

[61] Heyd, J., Scuseria, G. E. & Ernzerhof, M. Hybrid functionals based on a screened Coulomb potential. *J. Chem. Phys.* **118**, 8207–8215 (2003).

[62] Cohen, A. J., Mori-Sánchez, P. & Yang, W. Fractional charge perspective on the band gap in density-functional theory. *Physical Review B* **77**, 115123 (2008).

[63] Kresse, G. & Furthmüller, J. Efficient iterative schemes for ab initio total-energy calculations using a plane-wave basis set. *Physical Review B* **54**, 11169 (1996).

[64] Kittel, C. *Introduction to Solid State Physics* (Wiley, 2004).

[65] Monkhorst, H. J. & Pack, J. D. Special points for Brillouin-zone integrations. *Phys. Rev. B* **13**, 5188 (1976).

[66] Blöchl, P. E. Projector augmented-wave method. *Phys. Rev. B* **50**, 17953–17979 (1994).

[67] Maradudin, A. Some effects of point defects on the vibrations of crystal lattices. *Reports on Progress in Physics* **28**, 331 (1965).

[68] Elliott, R. J. *Vibrations of Defects in Lattices*, vol. 7237 (Argonne National Laboratory, 1966).

[69] Jahn, H. A., Teller, E. & Donnan, F. G. Stability of polyatomic molecules in degenerate electronic states - I–Orbital degeneracy. *Proc. R. Soc. Lond. A* **161**, 220–235 (1937).

[70] Öpik, U. & Pryce, M. H. L. Studies of the Jahn–Teller effect. I. A survey of the static problem. *Proc. R. Soc. Lond. A* **238**, 425–447 (1957).

[71] Longuet-Higgins, H. C., Öpik, U., Pryce, M. H. L. & Sack, R. Studies of the jahn-teller effect. ii. the dynamical problem. *Proceedings of the Royal Society of London. Series A* **244**, 1–16 (1958).

[72] Ham, F. S. Dynamical Jahn–Teller effect in paramagnetic resonance spectra: Orbital reduction factors and partial quenching of spin-orbit interaction. *Phys. Rev.* **138**, A1727–A1740 (1965).

[73] Ham, F. S. Effect of linear Jahn-Teller coupling on paramagnetic resonance in a ^2E state. *Physical Review* **166**, 307–321 (1968).

[74] O'Brien, C. M., Mary & Evangelou, S. N. The calculation of absorption band shapes in dynamic Jahn–Teller systems by the use of the Lanczos algorithm. *J. Phys. C: Solid State Phys.* **13**, 611–623 (1980).

[75] Silkinis, R. *et al.* Optical lineshapes for orbital singlet to doublet transitions in a dynamical Jahn-Teller system: the NiV$^-$ center in diamond. *Physical Review B* **110**, 075303 (2024).

[76] Razinkovas, L. *Vibrational properties and photoionization of color centers in diamond: theory and ab initio calculations*. Ph.D. thesis (2021). URL https://talpykla.elaba.lt/elaba-fedora/objects/elaba:114210427/datastreams/MAIN/content.

[77] O'Brien, M. C. M. & Evangelou, S. N. The calculation of absorption band shapes in dynamic jahn-teller systems by the use of the lanczos algorithm. *Journal of Physics C: Solid State Physics* **13**, 611–623 (1980).

[78] Markham, J. J. Interaction of normal modes with electron traps. *Rev. Mod. Phys.* **31**, 956 (1959).

[79] Kubo, R. & Toyozawa, Y. Application of the method of generating function to radiative and non-radiative transitions of a trapped electron in a crystal. *Prog. Theor. Phys.* **13**, 160–182 (1955).

[80] Lax, M. The franck-condon principle and its application to crystals. *The Journal of Chemical Physics* **20**, 1752–1760 (1952).

[81] Huang, K. & Rhys, A. Theory of light absorption and non-radiative transitions in F-centres. *Proceedings of the Royal Society of London. Series A. Mathematical and Physical Sciences* **204**, 406–423 (1950).

[82] Alkauskas, A., Buckley, B. B., Awschalom, D. D. & Van de Walle, C. G. First-principles theory of the luminescence lineshape for the

triplet transition in diamond NV centres. *New Journal of Physics* **16**, 073026 (2014).

[83] Perdew, J. P., Ernzerhof, M. & Burke, K. Rationale for mixing exact exchange with density functional approximations. *The Journal of Chemical Physics* **105**, 9982–9985 (1996).

[84] Adamo, C. & Barone, V. Toward reliable density functional methods without adjustable parameters: The PBE0 model. *The Journal of Chemical Physics* **110**, 6158–6170 (1999).

[85] Krukau, A. V., Vydrov, O. A., Izmaylov, A. F. & Scuseria, G. E. Influence of the exchange screening parameter on the performance of screened hybrid functionals. *The Journal of Chemical Physics* **125** (2006). 224106.

[86] Bertoldo, F., Ali, S., Manti, S. & Thygesen, K. S. Quantum point defects in 2D materials-the QPOD database. *npj Computational Materials* **8**, 56 (2022).

[87] Jin, Y. *et al.* Photoluminescence spectra of point defects in semiconductors: Validation of first-principles calculations. *Phys. Rev. Mater.* **5**, 084603 (2021).

[88] Hashemi, A. *et al.* Photoluminescence line shapes for color centers in silicon carbide from density functional theory calculations. *Phys. Rev. B* **103**, 125203 (2021).

[89] Freysoldt, C. *et al.* First-principles calculations for point defects in solids. *Reviews of Modern Physics* **86**, 253 (2014).

[90] Freysoldt, C., Neugebauer, J. & Van de Walle, C. G. Fully ab initio finite-size corrections for charged-defect supercell calculations. *Physical Review Letters* **102**, 1–4 (2009).

[91] Alkauskas, A., Broqvist, P. & Pasquarello, A. Defect energy levels in density functional calculations: Alignment and band gap problem. *Physical Review Letters* **101**, 046405 (2008).

[92] Alkauskas, A., Broqvist, P. & Pasquarello, A. Defect levels through hybrid density functionals: Insights and applications. *Physica Status Solidi B* **248**, 775–789 (2011).

[93] Alkauskas, A. & Pasquarello, A. Band-edge problem in the theoretical determination of defect energy levels: The O vacancy in ZnO as a benchmark case. *Physical Review B* **84**, 125206 (2011).

[94] Jones, R. O. & Gunnarsson, O. The density functional formalism, its applications and prospects. *Reviews of Modern Physics* **61**, 689 (1989).

[95] Hellman, A., Razaznejad, B. & Lundqvist, B. I. Potential-energy surfaces for excited states in extended systems. *The Journal of chemical physics* **120**, 4593–4602 (2004).

[96] Kowalczyk, T., Yost, S. R. & Voorhis, T. V. Assessment of the δSCF density functional theory approach for electronic excitations in organic dyes. *The Journal of Chemical Physics* **134**, 054128 (2011).

[97] Gali, A., Janzén, E., Deák, P., Kresse, G. & Kaxiras, E. Theory of spin-conserving excitation of the N- V- center in diamond. *Physical review letters* **103**, 186404 (2009).

[98] Davidsson, J. *et al.* First principles predictions of magneto-optical data for semiconductor point defect identification: the case of divacancy defects in 4H–SiC. *New Journal of Physics* **20**, 023035 (2018).

[99] Thiering, G. & Gali, A. Ab initio magneto-optical spectrum of group-IV vacancy color centers in diamond. *Physical Review X* **8**, 021063 (2018).

[100] Mackoit-Sinkevičienė, M., Maciaszek, M., Van de Walle, C. G. & Alkauskas, A. Carbon dimer defect as a source of the 4.1 eV luminescence in hexagonal boron nitride. *Applied Physics Letters* **115**, 212101 (2019).

[101] Hashemi, A. *et al.* Photoluminescence line shapes for color centers in silicon carbide from density functional theory calculations. *Physical Review B* **103**, 125203 (2021).

[102] Jin, Y. *et al.* Photoluminescence spectra of point defects in semiconductors: Validation of first-principles calculations. *Physical Review Materials* **5**, 084603 (2021).

[103] Gunnarsson, O. & Lundqvist, B. I. Exchange and correlation in atoms, molecules, and solids by the spin-density-functional formalism. *Physical Review B* **13**, 4274–4298 (1976).

[104] Ivády, V., Abrikosov, I. A. & Gali, A. First principles calculation of spin-related quantities for point defect qubit research. *npj Computational Materials* **4**, 76 (2018).

[105] Ivády, V., Simon, T., Maze, J. R., Abrikosov, I. & Gali, A. Pressure and temperature dependence of the zero-field splitting in the ground state of NV centers in diamond: A first-principles study. *Physical Review B* **90**, 235205 (2014).

[106] Abtew, T. A. *et al.* Dynamic Jahn-Teller effect in the NV- center in diamond. *Physical Review Letters* **107**, 146403 (2011).

[107] Hao, P. *et al.* Lattice constants from semilocal density functionals with zero-point phonon correction. *Physical Review B* **85**, 014111 (2012).

[108] Vinet, P., Smith, J. R., Ferrante, J. & Rose, J. H. Temperature effects on the universal equation of state of solids. *Physical Review B* **35**, 1945–1953 (1987).

[109] Madelung, O. *Semiconductors: group IV elements and III-V compounds* (Springer, 2012).

[110] Zouboulis, E. S., Grimsditch, M., Ramdas, A. K. & Rodriguez, S. Temperature dependence of the elastic moduli of diamond: A Brillouin-scattering study. *Physical Review B* **57**, 2889–2896 (1998).

[111] Levinshtein, M. E., Rumyantsev, S. L. & Shur, M. S. *Properties of Advanced Semiconductor Materials: GaN, AIN, InN, BN, SiC, SiGe* (John Wiley & Sons, 2001).

[112] Choyke, W. & Pensl, G. Physical properties of sic. *Mrs Bulletin* **22**, 25–29 (1997).

[113] Batchelder, D. N. & Simmons, R. O. Lattice constants and thermal expansivities of silicon and of calcium fluoride between 6° and 322°K. *J. Chem. Phys.* **41**, 2324–2329 (1964).

[114] Bludau, W., Onton, A. & Heinke, W. Temperature dependence of the band gap of silicon. *J. Appl. Phys.* **45**, 1846–1848 (1974).

[115] Hinuma, Y., Grüneis, A., Kresse, G. & Oba, F. Band alignment of semiconductors from density-functional theory and many-body perturbation theory. *Phys. Rev. B* **90**, 155405 (2014).

[116] Chen, W. & Pasquarello, A. Band-edge levels in semiconductors and insulators: Hybrid density functional theory versus many-body perturbation theory. *Phys. Rev. B* **86**, 035134 (2012).

[117] Togo, A. & Tanaka, I. First principles phonon calculations in materials science. *Scripta Materialia* **108**, 1–5 (2015).

[118] Kulda, J. *et al.* Overbending of the longitudinal optical phonon branch in diamond as evidenced by inelastic neutron and X-ray scattering. *Phys. Rev. B* **66**, 241202 (2002).

[119] Hummer, K., Harl, J. & Kresse, G. Heyd-Scuseria-Ernzerhof hybrid functional for calculating the lattice dynamics of semiconductors. *Physical Review B* **80**, 115205 (2009).

[120] Deák, P., Aradi, B., Kaviani, M., Frauenheim, T. & Gali, A. Formation of NV centers in diamond: A theoretical study based on calculated transitions and migration of nitrogen and vacancy related defects. *Physical Review B* **89**, 075203 (2014).

[121] Zemła, M. R., Czelej, K., Kamińska, P., Van de Walle, C. G. & Majewski, J. A. Electronic structure and magneto-optical properties of silicon-nitrogen-vacancy complexes in diamond. *Physical Review B* **102**, 115102 (2020).

[122] Ramprasad, R., Zhu, H., Rinke, P. & Scheffler, M. New perspective on formation energies and energy levels of point defects in nonmetals. *Physical Review Letters* **108**, 066404 (2012).

[123] Bean, A. R. & Newman, R. C. The solubility of carbon in pulled silicon crystals. *J. Phys. Chem. Solids* **32**, 1211–1219 (1971).

[124] Coutinho, J. *et al.* Interstitial carbon-oxygen center and hydrogen related shallow thermal donors in Si. *Phys. Rev. B* **65**, 014109 (2001).

[125] Wang, H., Chroneos, A., Londos, C. A., Sgourou, E. N. & Schwingenschlögl, U. Carbon related defects in irradiated silicon revisited. *Sci. Rep.* **4**, 4909 (2014).

[126] Hao, S., Kantorovich, L. & Davies, G. The interstitial $\mathrm{C_iO_i}$ defect in bulk Si and $\mathrm{Si}_{1-x}\mathrm{Ge}_x$. *J. Phys.: Condens. Matter* **16**, 8545–8555 (2004).

[127] Thiering, G. & Gali, A. Ab initio magneto-optical spectrum of group-IV vacancy color centers in diamond. *Physical Review X* **8**, 021063 (2018).

[128] Gali, A., Janzén, E., Deák, P., Kresse, G. & Kaxiras, E. Theory of spin-conserving excitation of the N-V- center in diamond. *Physical Review Letters* **103**, 186404 (2009).

[129] Gali, A. & Maze, J. R. Ab initio study of the split silicon-vacancy defect in diamond: Electronic structure and related properties. *Physical Review B* **88**, 235205 (2013).

[130] Alkauskas, A., Buckley, B. B., Awschalom, D. D. & Van de Walle, C. G. First-principles theory of the luminescence lineshape for the triplet transition in diamond NV centres. *New Journal of Physics* **16**, 073026 (2014).

[131] Collins, A. T. & Spear, P. M. The 1.40 eV and 2.56 eV centres in synthetic diamond. *J. Phys. C: Solid State Phys.* **16**, 963–973 (1983).

[132] Thiering, G. & Gali, A. Magneto-optical spectra of the split nickel-vacancy defect in diamond. *Phys. Rev. Res.* **3**, 043052 (2021).

[133] Clark, C. D., Kanda, H., Kiflawi, I. & Sittas, G. Silicon defects in diamond. *Physical Review B* **51**, 16681 (1995).

[134] Palyanov, Y. N., Kupriyanov, I. N., Borzdov, Y. M. & Surovtsev, N. V. Germanium: a new catalyst for diamond synthesis and a new optically active impurity in diamond. *Scientific Reports* **5**, 14789 (2015).

[135] Iwasaki, T. *et al.* Tin-vacancy quantum emitters in diamond. *Physical Review Letters* **119**, 253601 (2017).

[136] Gordon, L., Janotti, A. & Van de Walle, C. G. Defects as qubits in $3c-$ and $4h-$SiC. *Physical Review B* **92**, 045208 (2015).

[137] Falk, A. L. *et al.* Polytype control of spin qubits in silicon carbide. *Nature communications* **4**, 1819 (2013).

[138] Petrone, A. *et al.* Electronic structures and spectroscopic signatures of silicon-vacancy containing nanodiamonds. *Physical Review B* **98**, 205405 (2018).

[139] Davies, G. & Hamer, M. Optical studies of the 1.945 ev vibronic band in diamond. *Proceedings of the Royal Society of London. Series A* **348**, 285–298 (1976).

[140] Jin, Y., Govoni, M. & Galli, G. Vibrationally resolved optical excitations of the nitrogen-vacancy center in diamond. *npj Computational Materials* **8**, 238 (2022).

[141] Falk, A. L. *et al.* Electrically and mechanically tunable electron spins in silicon carbide color centers. *Physical Review Letters* **112**, 187601 (2014).

[142] Seo, H., Ma, H., Govoni, M. & Galli, G. Designing defect-based qubit candidates in wide-gap binary semiconductors for solid-state quantum technologies. *Physical Review Materials* **1**, 075002 (2017).

[143] Freysoldt, C. *et al.* First-principles calculations for point defects in solids. *Reviews of modern physics* **86**, 253 (2014).

[144] Togo, A. & Tanaka, I. First principles phonon calculations in materials science. *Scripta Materialia* **108**, 1–5 (2015).

[145] Bell, R. J., Dean, P. & Hibbins-Butler, D. C. Localization of normal modes in vitreous silica, germania and beryllium fluoride. *J. Phys. C: Solid State Phys.* **3**, 2111–2118 (1970).

[146] Alkauskas, A., Buckley, B. B., Awschalom, D. D. & Van de Walle, C. G. First-principles theory of the luminescence lineshape for the triplet transition in diamond NV centres. *New J. Phys.* **16**, 073026 (2014).

[147] Kehayias, P. *et al.* Infrared absorption band and vibronic structure of the nitrogen-vacancy center in diamond. *Physical Review B* **88**, 165202 (2013).

[148] Rondin, L. *et al.* Magnetometry with nitrogen-vacancy defects in diamond. *Reports on progress in physics* **77**, 056503 (2014).

[149] Vindolet, B. *et al.* Optical properties of siv and gev color centers in nanodiamonds under hydrostatic pressures up to 180 gpa. *Physical Review B* **106**, 214109 (2022).

[150] Hilberer, A. *et al.* Enabling quantum sensing under extreme pressure: Nitrogen-vacancy magnetometry up to 130 gpa. *Physical Review B* **107**, L220102 (2023).

[151] Loubeyre, P., Occelli, F. & Dumas, P. Synchrotron infrared spectroscopic evidence of the probable transition to metal hydrogen. *Nature* **577**, 631–635 (2020).

[152] Flores-Livas, J. A. *et al.* A perspective on conventional high-temperature superconductors at high pressure: Methods and materials. *Physics Reports* **856**, 1–78 (2020).

[153] Drozdov, A. *et al.* Superconductivity at 250 k in lanthanum hydride under high pressures. *Nature* **569**, 528–531 (2019).

[154] Somayazulu, M. *et al.* Evidence for superconductivity above 260 k in lanthanum superhydride at megabar pressures. *Physical review letters* **122**, 027001 (2019).

[155] Shang, Z. *et al.* Microwave-assisted spectroscopy of vacancy-related spin centers in hexagonal SiC. *Physical Review Applied* **15**, 034059 (2021).

[156] Tajima, M., Asahara, S., Satake, Y. & Ogura, A. Free-to-bound emission from interstitial carbon and oxygen defects ($\mathrm{C_iO_i}$) in electron-irradiated Si. *Appl. Phys. Express* **14**, 011006 (2021).

[157] Bian, G., Thiering, G. & Gali, A. Theory of optical spinpolarization of axial divacancy and nitrogen-vacancy defects in 4H-SiC (2024). 2409.10233.

Santrauka

1. Įžanga

Kvantinių technologijų plėtra atvėrė naujas galimybes kvantiniams kompiuteriams, kvantinei komunikacijai ir kvantiniams jutikliams [1–10]. Vienas pagrindinių šių technologijų reikalavimų yra gebėjimas patikimai kurti, valdyti ir detektuoti kvantines būsenas. Kietakūnės platformos, ypač puslaidininkiai, suteikia gerai išvystytą aplinką realiztuoti kvantinėms sistemoms, o taškiniai defektai gali būti perspektyvūs kandidatai tapti kvantiniais bitais (kubitais) ir pavieniais fotonų emiteriais [11].

Taškiniai defektai yra atominio mastelio netobulumai kristalinėje gardelėje, kurie į puslaidininkio draustinę juostą įveda lokalizuotas elektronines būsenas. Nors istoriniu požiūriu šie defektai buvo laikomi nepageidaujamais puslaidininkinių prietaisų veikimui, tam tikri gilieji defektai (taip pat vadinami spalviniais centrais) pasižymi stabiliomis optinėmis ir sukinio savybėmis, tinkamomis kvantinėms technologijoms [11]. Pavyzdžiui, neigiamai įkrautas azoto-vakansijos (NV^-) centras deimante demonstruoja milisekundžių eilės koherencijos laikus net kambario temperatūroje ir tampa pagrindiniu kandidatu kvantiniams jutikliams ir kvantinei komunikacijai [12–15]. Taip pat tokie defektai silicio karbide ir silicyje veikia infraraudonosios spinduliuotės ruože, suteikdami galimybę būti suderinamais su šviesolaidine infrastruktūra [16–27].

Kvantinių technologijų taikymui tinkamų defektų identifikavimas ir optimizavimas reikalauja teorinio pagrindo, kuris leistų tiksliai ir efektyviai prognozuoti jų elektronines ir optines savybes. *Ab initio* (pirminių principų) skaičiavimai, ypač tie, kurie remiasi tankio funkcionalo teorija (angl. *density functional theory*, DFT), tapo nepakeičiamu įrankiu spręsti įvairiems uždaviniams. Tankio funkcionalo teorija tapo dominuojančiu skaitiniu metodu tirti puslaidininkių ir jų defektų elektroninei bei optinei struktūrai. Nors ši teorija pagal Kohn–Sham formalizmą yra iš principo tiksli [28], praktinis jos įgyvendinimas priklauso nuo pakaitos–koreliacijos funkcionalo aproksimacijos. Dažniausiai naudojami funkcionalai puslaidininkių sistemoms yra apibendrinto gradiento aproksimacijos (angl. *general gradient approximation*, GGA) funkcionalai, tokie kaip PBE funkcionalas [29], ar hibridiniai funkcionalai, kaip HSE [30]. Kiekviena funkcionalų klasė turi savo privalumų ir trūkumų. GGA funkcionalai skaitiniu požiūriu yra labai efektyvūs, tačiau jie sistemingai nuvertina puslaidininkių draustinį juostų tarpą [31]. Hibridiniai funkcionalai pagerina draustinio juostų tarpo vertes, bet yra skaitiškai žymiai brangesni [32]. Didelės apimties defektų paieška ir elektron–fononinės sąveikos modeliavimas reikalauja pusiausvyros tarp tikslumo ir skaičiavimų efektyvumo [33, 34].

SCAN tankio funkcionalas [35], priklausantis meta-GGA klasei, įskaito papildomą informaciją apie kinetinės energijos tankį, taip pagerindamas pakaitos–koreliacijos efektų aprašymą. Įrodyta, kad SCAN tiksliau prognozuoja gardelės parametrus ir draustinės juostos tarpus, palyginti su GGA funkcionalais [36,37]. SCAN funkcionalas turi didelių privalumų modeliuojant taškinius defektus, nes tokios sistemos dažniausiai tiriamos naudojant supergardelės metodiką, kuris reikalauja efektyvių skaičiavimo metodų dėl didelio atomų skaičiaus [38]. SCAN pagerina elektronų lokalizacijos ir defektų lygių aprašymą draustinėje juostoje, išvengiant didelių skaičiavimo kaštų, būdingų hibridiniams funkcionalams. Nors SCAN plačiai taikomas idealiems kristalams [39], jo taikymas defektų tyrimuose vis dar yra ribotas [40–43]. Siekiant sistemiškai įvertinti SCAN tankio funkcionalo tikslumą modeliuojant sužadintas būsenas ir elektron–fononinę sąveiką, reikalingi išsamesni tyrimai.

Šio darbo tikslas yra įvertinti SCAN funkcionalo ir jo variantų, rSCAN [44] ir r^{2}SCAN [45], tikslumą ir skaičiavimo efektyvumą modeliuojant taškinių defektų elektronines ir virpesines savybes puslaidininkiuose. Konkretus siekis – parodyti, kad SCAN šeimos funkcionalai gali tiksliai prognozuoti optines sužadinimo energijas, modeliuoti liuminescencijos ir sugerties optines linijas defektams deimante, silicyje ir silicio karbide. Tikslus elektron–fononinės sąveikos modeliavimas suteiks gilesnių įžvalgų apie defektų dinamiką ir jų tinkamumą kvantinėms technologijoms. Atlikdami išsamią skaičiavimų analizę, siekiame įrodyti, kad SCAN tankio funkcionalas yra patikimas ir praktiškas įrankis defektų modeliavimui, leidžiantis atlikti tikslius ir skaitiškai efektyvius tyrimus, kurie leistų plačiai ištirti potencialius kvantinius defektus.

1.1. Tyrimo tikslas

Pagrindinis šio darbo tikslas yra įvertinti SCAN tankio funkcionalo ir jo variantų (rSCAN ir r^{2}SCAN) tinkamumą modeliuojant taškinių defektų puslaidininkiuose elektronines ir virpesines savybes.

1.2. Tyrimo uždaviniai

Norint pasiekti šio darbo tikslą, buvo iškelti šie uždaviniai:

1. Naudojant SCAN, rSCAN ir r^{2}SCAN tankio funkcionalus apskaičiuoti optines sužadinimo energijas įvairiems taškiniams defektams deimante, silicyje ir 4H silicio karbide.

2. Naudojant šiuos meta-GGA klasės funkcionalus sumodeliuoti teorines liuminescencijos ir sugerties spektrines linijas pasirinktoms defektų sistemoms.

3. Palyginti gautus rezultatus su GGA klasės bei hibridiniais funkcionalais ir eksperimentiniais duomenimis.

1.3. Ginamieji teiginiai

1. Skaičiuojant optinių sužadinimų energijas taškiniams defektams deimante ir 4H silicio karbide, SCAN tankio funkcionalas ir jo variantai (rSCAN ir r^{2}SCAN) tikslumu prilygsta arba pranoksta skaičiavimams daug kartų reiklesnį hibridinį HSE06 funkcionalą.

2. Šie SCAN tipo funkcionalai tiksliai modeliuoja elektron–fononinę sąveiką ir su palyginti mažais kompiuteriniais resursais gaunamos optinės linijos, kurios labai gerai sutampa su eksperimentiniais duomenimis.

3. Naudojant naujovišką daugelio modų Jahn–Teller sistemų skaičiavimo metodologiją kartu su r^{2}SCAN funkcionalu, mes tiksliai sumodeliavome neigiamai įkrautos nikelio-vakansijos centro deimante fotoliuminescencijos spektrą ir nustatėme optines savybes, kurios atsiranda dėl Jahn–Teller sąveikų, taip parodydami funkcionalo efektyvumą nustatant vibroninių sąveikų konstantas.

1.4. Autoriaus indėlis ir rezultatų pristatymas mokslinei visuomenei

Doktorantūros laikotarpiu autorius prisidėjo prie penkių mokslinių straipsnių:

(T1) Marek Maciaszek, Vytautas Žalandauskas, Rokas Silkinis, Audrius Alkauskas, and Lukas Razinkovas, *The application of the SCAN density functional to color centers in diamond*, J. Chem. Phys. **159**, 084708 (2023).

(T2) Rokas Silkinis, Vytautas Žalandauskas, Gergő Thiering, Adam Gali, Chris G. Van de Walle , Audrius Alkauskas, Lukas Razinkovas, *Optical lineshapes for orbital singlet to doublet transitions in a dynamical Jahn-Teller system: the NiV$^-$ center in diamond*, Phys. Rev. B **110**, 075303 (2024).

(T3) Rokas Silkinis, Marek Maciaszek, Vytautas Žalandauskas, Marianne Etzelmüller Bathen, Audrius Alkauskas, Lukas Razinkovas, *Optical lineshapes of the C center in silicon from ab initio calculations:*

Interplay of localized modes and bulk phonons, Phys. Rev. B **111**, 125136 (2025).

(T4) Vytautas Žalandauskas, Rokas Silkinis, Lasse Vines, Lukas Razinkovas, and Marianne Etzelmüller Bathen, *Theory of the divacancy in 4H-SiC: Impact of Jahn–Teller effect on optical properties*, npj Computational Materials, priimtas (2025).

(T5) Meysam Mohseni, Lukas Razinkovas, Vytautas Žalandauskas, Gergő Thiering, Adam Gali, *Magneto-optical properties of Group-IV–vacancy centers in diamond upon hydrostatic pressure*, https://arxiv.org/abs/2408.10407 (2024).

Tyrimo rezultatai buvo pristatyti šiose mokslinėse konferencijose:

I. V. Žalandauskas, M. Maciaszek, L. Razinkovas, A. Alkauskas, *The application of the SCAN density functional to colour centres in diamond*, Open Readings 2022, 2022-03-15, Vilnius, Lietuva. Žodinis pranešimas.

II. V. Žalandauskas, M. Maciaszek, L. Razinkovas, R. Silkinis, A. Alkauskas, *The application of the SCAN density functional to colour centres in diamond*, DSQT2022, 2022-06-15, Stokholmas, Švedija. Stendinis pranešimas.

III. V. Žalandauskas, M. Maciaszek, L. Razinkovas, R. Silkinis, A. Alkauskas, *The application of the SCAN density functional to colour centres in diamond*, 24-th International Conference–School ADVANCED MATERIALS AND TECHNOLOGIES, 2022-08-24, Palanga, Lietuva. Stendinis pranešimas.

IV. V. Žalandauskas, M. E. Bathen, L. Razinkovas, *Ab Initio Investigation of Vibrational Properties of Divacancy Defects in Silicon Carbide*, Humboldt Kolleg on Synthetic Quantum Matter, 2023-07-03, Vilnius, Lietuva. Stendinis pranešimas.

V. V. Žalandauskas, L. Razinkovas, M. E. Bathen, *Ab initio study of vibrational properties of divacancy defects in 4H-SiC*, The 32nd International Conference on Defects in Semiconductors, 2023-09-12, Rehoboth Beach, Delavero valstija, JAV. Stendinis pranešimas.

VI. V. Žalandauskas, R. Silkinis, L. Vines, L. Razinkovas, M. E. Bathen, *Ab initio study of vibrational properties of divacancy defects in 4H-SiC*, Open Readings 2024, 2024-04-23, Vilnius, Lietuva. Stendinis pranešimas.

VII. V. Žalandauskas, R. Silkinis, L. Vines, L. Razinkovas, M. E. Bathen, *Impact of the Jahn-Teller effect on optical properties of divacancies in 4H-SiC*, DSQT2024, 2024-06-11, Budapeštas, Vengrija. Stendinis pranešimas.

2. Disertacijos sandara

Šią disertaciją sudaro penki pagrindiniai skyriai:

- Pirmame skyriuje trumpai aptariami taškiniai kristalų defektai ir jų svarba kvantinėse technologijose. Čia suformuluojamas tiriamojo darbo tikslas ir pagrindiniai uždaviniai.
- Antrame skyriuje pristatoma teorija ir metodologija skirta skaičiuoti defektų eletroninei ir virpesinei struktūrai bei vibroninei struktūrai, kuri atsiranda dėl Jahn–Teller efekto, kur neįmanoma adiabatiškai atskirti elektroninių ir virpesinių laivės laispsnių.
- Trečiame skyriuje pristatomi idealių deimanto, silicio ir silicio karbido kristalų parametrai, kurie buvo suskaičiuoti naudojant PBE, SCAN, rSCAN, r^{2}SCAN ir HSE06 tankio funkctionalus ir palyginti su eksperimentiniais rezultatais. Taip pat šiame skyriuje palygintos taškinių defektų deimante, silicyje ir 4H silicio karbide formavimosi energijos, krūvio būsenos perėjimo lygiai, befononės linijos energijos ir belaukio suskilimo vertės, kurios suskaičiuotos su šiais tankio funkcionalais ir palygintos su eksperimentiniais rezultatais.
- Ketvirtame skyriuje pristatyti neigiamai įkrauto azoto-vakansijos centro deimante, neutralių divakansijų 4H-SiC bei C-centro silicyje *ab initio* elektron–fononinės sąveikos ir optinių linijų skaičiavimai. Šio skyriaus pagrindinis tikslas buvo įvertinti SCAN, rSCAN ir r^{2}SCAN tankio funkcionalų tikslumą modeliuojant elektron–fononinę sąveiką ir optines linijas, palyginant gautus rezultatus su standartiniais PBE ir HSE06 funkcionalais bei eksperimentiniais duomenimis.
- Penktas skyrius nagrinėja suskaičuotas optines linijas, kurios yra veikiamos ryškaus Jahn–Teller efekto neigiamai įkrauto nikelio-vakansijos centro deimante bei neutralių *hh* ir *kk* divakansijų defektų 4H silicio karbide. Pagrindinis šio tyrimo tikslas buvo tiksliai sumodeliuoti optinių linijų formas, taikant tankio funkcionalo teorijos skaičiavimus, panaudojant daugelio modų dinaminio Jahn–Teller efekto (kuris kyla dėl elektroninio išsigimimo esančio šiuose taškiniuose defektuose) skaičiavimo metodologiją.

Toliau trumpai pristatomas disertacijos turinys ir pagrindinės išvados.

2.1. Teorijos ir metodologijos apžvalga

Schrödinger lygtis ir adiabatinė aproksimacija

Tiesioginis Schrödinger lygties sprendimas realioms taškinių defektų puslaidininkiuose sistemoms šiuolaikiniais skaitmeniniais metodais yra nepraktiškas ar net neįmanomas dėl eksponentiškai augančio reikalingų skaičiavimų išteklių didėjant dalelių skaičiui. Todėl siekiant išspręsti šią problemą taikomos įvairios aproksimacijos.

Kvantinės chemijos skaičiavimuose dažniausiai naudojama adiabatinė aproksimacija, kuri efektyviai atskiria branduolių ir elektronų sistemas dėl didelio banrduolių ir elektronų masių skirtumo. Šioje disertacijoje naudojama statinė adiabatinė aproksimacija [46] , kuri yra grubiausias adiabatinis artinys, tačiau šis artinys yra patogus norint nagrinėti neadiabatinius reiškinius kaip Jahn–Teller efektą [47]. Naudojant statinę adiabatinę aproksimaciją, Schrödinger lygtis sprendžiama laikant, kad branduoliai yra klasikinės nejudančios dalelės, o tada suradus elektroninės lygties sprendinius yra suskaičiuojamas gardelės dinamiką nusakantis adiabatinis potencinės energijos paviršius (angl. *adiabatic potential energy surface*, APES) branduoliams. Formaliai, adiabatinių bendrosios sistemos sprendinių išraiška yra tokia:

$$\Psi_i(\mathbf{r}, \mathbf{R}) = \psi_i(\mathbf{r})\chi_i(\mathbf{R}), \tag{2}$$

kur $\psi_i(\mathbf{r})$ yra elektroninė banginė funkcija, o $\chi_i(\mathbf{R})$ yra branduolių banginė funkcija, kai elektronai yra i būsenoje. Ši aproksimacija yra gana tiksli tik tada, kai energijos skirtumai tarp elektroninių lygmenų yra didesni nei charakteringa virpesinės sistemos sužadinimo energija.

Dėl galimo defekto elektroninių būsenų išsigimimo nebegalima atskirai nagrinėti elektronų ir branduolių dinamikos. Šiose išsigimusiose būsenose yra maišomos elektroninės ir branduolinės būsenos, kurios yra vadinamos Jahn–Teller (JT) sistemomis, o jų bendra banginė funkcija yra:

$$\Psi(\mathbf{r}, \mathbf{R}) = \sum_i \psi_i(\mathbf{r})\chi_i(\mathbf{R}), \tag{3}$$

kur i sumuojamas per išsigimusius elektroninius lygmenis $\psi_i(\mathbf{r})$.

Tankio funkcionalo teorija

Šioje disertacijoje naudojama tankio funkcionalo teorija (DFT), kurią suformulavo Hohenberg ir Kohn [48, 49]. DFT tapo plačiausiai naudojamu *ab initio* metodu kietojo kūno elektroninės struktūros skaičiavimams dėl savo efektyvumo modeliuojant sistemas, turinčias iki kelių tūkstančių atomų. Vietoj daugiaelektroninės banginės funkcijos, DFT naudoja elektronų tankį $n(\mathbf{r})$, priklausantį tik nuo trijų erdvinių koordinačių (žr. 2.2 skyrelį).

$$n(\mathbf{r}) = \langle\psi|\hat{n}(\mathbf{r})|\psi\rangle = \langle\psi|\sum_{i}^{N_\mathrm{e}}\delta(\mathbf{r}-\mathbf{r}_i)|\psi\rangle. \qquad (4)$$

DFT teorinis pagrindas remiasi dviem Hohenberg–Kohn teoremomis. Pirmoji teorema teigia, kad pagrindinės būsenos elektronų tankis $n_0(\mathbf{r})$ vienareikšmiškai apibrėžia sistemos išorinį potencialą $\hat{v}_\mathrm{ext}(\mathbf{r})$ ir visas elektronines sistemos savybes. Antroji teorema nusako, kad bendra elektronų energija yra minimali tada, kai naudojamas tikrasis pagrindinės būsenos elektronų tankis. Tai reiškia, kad galima variaciniu principu rasti pagrindinės būsenos energiją ir elektronų tankį minimizuojant bendros energijos funkcionalą $E_0 = \min_n E[n]$.

Tankio funkcionalo teorija yra griežtai apibrėžta pagrindinei elektroninei būsenai, tačiau tikslus pakaitos–koreliacijos funkcionalo (angl. *exchange-correlation functional*) analitinis pavidalas nėra žinomas. DFT remiasi apytikriais funkcionalais, kurie skirtingai aprašo aprašo pakaitos–koreliacijos efektus. Keli pagrindiniai funkcionalų tipai yra:

- **Lokalaus tankio aproksimacija** (angl. *local density approximation*, LDA) – vienas paprasčiausių funkcionalų, kuriame pakaitos energija yra tokia pati kaip homogeniškose elektronų dujose ir daro prielaidą, kad pakaitos–koreliacijos energija bet kuriame taške priklauso tik nuo vietinio elektronų tankio. Šis funkcionalas dažnai per stipriai suriša elektronus, o tai nulemia per mažus tarpus tarp lygmenų kietuose kūnuose.

- **Apibendrinto gradiento aproksimacija** – įtraukia elektronų tankio gradientą, leidžiantį geriau aprašyti nehomogeniškas sistemas. Vienas populiariausių GGA funkcionalų yra PBE [29], kuris plačiai naudojamas kietųjų kūnų sistemų modeliavimui.

- **Meta-GGA funkcionalai** – patobulinta GGA versija, kurioje prie elektronų tankio ir jo gradiento taip pat įtraukiama kinetinės energijos tankio priklausomybė. SCAN (angl. *Strongly Constrained and Appropriately Normed*) ir r^{2}SCAN funkcionalai priklauso šiai klasei ir geriau aprašo kristalų savybes nei GGA funkcionalai [35, 45].

- **Hibridiniai funkcionalai** – į pakaitos–koreliacijos funkcionalą įtraukiama dalis tikslios Hartree–Fock pakaitos. Šie funkcionalai puslaidininkiuose ir izoliatoriuose pagerina atstumus tarp lygmenų. Vienas iš dažniausiai naudojamų hibridinių funkcionalų yra HSE [30], kuris tiksliau prognuozuoja draustinės juostos tarpus ir defektų lygmenis.

Idealiame kristale, kuris yra begalinė periodinė struktūra, vienas elementarusis gardelės narvelis apibūdina visą kristalą. Tačiau defekto įvedimas į gardelę suardo jos periodiškumą, todėl reikia alternatyvių teorinių metodų defektų modeliavimui. Vienas plačiausiai naudojamų metodų yra supergardelės metodas [38], kur didelė gardelė su defektu yra periodiškai atkartojama (žr. 2.2 pav.). Nors supergardelės yra baigtinio dydžio, kruopštus supergardelių dydžio konvergavimas leidžia sumodeliuoti giliųjų defektų elektroninę struktūrą.

Virpesinė struktūra ir įterpimo metodologija

Nustačius elektroninės sistemos būsenas, defekto gardelės virpesiai yra apskaičiuojami naudojant harmoninę aproksimaciją, pagal kurią virpesiai atitinka mažos amplitudės judėjimą aplink pusiausvyros padėtis (žr. 2.3.1 skyrių). Tokie virpesiai dažniausiai vadinami fononais. Defekto buvimas pakeičia idealios gardelės virpesinę struktūrą. Įterpus defektą, gali atsirasti lokalizuotos arba rezonansinės modos, kurių amplitudė defekto aplinkoje yra didesnė nei erdviškai išplitusių kristalo virpesių. Dėl šios priežasties tokie virpesiai stipriau sąveikauja su elektronine sistema ir yra reikšmingi elektron–fononinės sąveikos defektuose aprašymui. Lokalizuotos modos pasirodo energijos srityje, kurioje idealus kristalas neturi virpesių. Šios modos yra stipriai lokalizuotos erdvėje aplink defektą, o rezonansinės modos susidaro kaip perturbuoti kristalo virpesiai tam tikrame energijos intervale.

Šiuolaikiniai DFT skaičiavimai gali modeliuoti supergardeles, kuriose yra daugiau nei keli tūkstančiai atomų ir yra pakankama energijos konvergavimui, tačiau tokie sistemos dydžiai nėra pakankami pilnai pagauti mažos energijos akustinių fononų įtakai. Šis apribojimas kyla dėl periodinių kraštinių sąlygų ir riboto virpesinių laisvės laipsnių skaičiaus tokiose supergardelėse. Norint apeiti riboto supergardėlių dydžio keliamus apribojimus, taikome jėgos konstantų įterpimo metodologiją [34,82]. Šis metodas išnaudoja puslaidininkiams būdingą trumpasiekę tarpatominių sąveikų pobūdį. Kai atomas yra pajudinamas iš savo pusiausvyros padėties, jėga, kuria jis veikia aplinkinius atomus, greitai silpsta didėjant atstumui nuo pajudinto atomo. Šis spartus sąveikos slopimas leidžia efektyviai sukonstruoti dinaminę jėgos konstantų matricą didelėms supergardelėms. Dinaminės matricos konstravimas atliekamas pagal šias taisykles (žr. pav. 2.4):

- Jei du atomai yra ne didesniu nuotoliu nei r_b, tada naudojami atitinkami elementai iš idealios supergardelės dinaminės matricos.

- Jei atomų poros yra nutolusios ne daugiau kaip r_d atstumu nuo defekto, naudojami matricos elementai iš defektą turinčios supergardelės.

- Visais kitais atvejais matricos elementai prilyginami nuliui.

Naudojant jėgų konstantų įterpimo metodologiją stebimas optinės linijos konvergavimas didinant supergardelės dydį. Esant pakankamai dideliai supergardelei, gauname mažos energijos virpesines modas ir taip pat galimus defekto virpesius, kurie rezonuoja su šiomis išplitusiomis kristalo modomis. Dažniausiai konvergencija pasiekiama supergardelėse, kurios turi daugiau nei 10 000 atomų.

2.2. Idealaus kristalo savybių skaičiavimai

Norint tirti taškinių defektų elektroninę ir virpesinę struktūrą, pirmiausia svarbu tiksliai aprašyti medžiagą, kurioje yra šie defektai. Lentelėje 1 pateiktos su PBE, SCAN, rSCAN, r^{2}SCAN ir HSE06 funkcionalais apskaičiuotos deimanto, 4H silicio karbido ir silicio gardelių konstantos bei draustinio juostos tarpo vertės, kurios palygintos su eksperimentiniais duomenimis.

Deimanto atveju SCAN ir rSCAN duoda artimiausias gardelės konstantos vertes eksperimentui, kurios skiriasi tik per 0.001 Å. r^{2}SCAN ir PBE funkcionalai atitinkamai pervertina gardelės konstantą 0.006 ir 0.017 Å, o HSE06 nuvertina per 0.009 Å. Draustinio juostos tarpo skaičiavimuose PBE funkcionalu apskaičiuotas draustinio juostos tarpas 4.12 eV, yra gerokai mažesnis už eksperimentinę vertę, kuri siekia 5.48 eV [109]. SCAN funkcionalas pagerina PBE rezultatą, padidindamas draustinio juostos tarpą 0.44 eV. Tuo tarpu rSCAN ir r^{2}SCAN duoda mažesnius padidėjimus (0.26 eV ir 0.21 eV atitinkamai). Su hibridiniu HSE06 funkcionalu gauta 5.34 eV vertė geriausiai atitinka eksperimentinį rezultatą.

4H silicio karbido atveju SCAN šeimos funkcionalai tiksliai atkartoja tiek a, tiek c gardelės konstantas. SCAN ir r^{2}SCAN nuokrypiai nuo eksperimentinių verčių neviršija 0.006 Å (a) ir 0.017 Å (c), o PBE rodo didesnį nuokrypį, pervertindamas abu parametrus (0.013 ir 0.044 Å atitinkamai). HSE06 gerai prognozuoja a, tačiau nuvertina c per 0.034 Å. Draustinio juostos tarpo E_g vertės rodo tą pačią tendenciją kaip ir deimante: PBE stipriai nuvertina, SCAN, rSCAN ir r^{2}SCAN duoda artimesnes vertes, tačiau tik su HSE06 gaunama eksperimentui artima reikšmė [112].

Silicio gardelės konstanta a taip pat geriausiai prognozuojama naudojant SCAN šeimos funkcionalus. Kaip ir deimante ar 4H-SiC, PBE pervertina, o HSE06 nuvertina gardelės konstantos vertes palyginus su eksperimentu [113]. Draustinio juostos tarpo skaičiavimai rodo ryškesnius skirtumus: PBE prognozuojama vertė yra beveik perpus mažesnė už eksperimentinę, tuo tarpu SCAN tipo funkcionalai duoda geresnius

1 lentelė: Deimanto, 4H silicio karbido ir silicio gardelės konstantos a ir c (Å) bei draustinio juostos tarpo E_g (eV) vertės.

	deimantas		4H-SiC			silicis	
	a	E_g	a	c	E_g	a	E_g
PBE	3.572	4.120	3.093	10.126	2.223	5.469	0.611
SCAN	3.554	4.558	3.074	10.065	2.596	5.428	0.825
rSCAN	3.556	4.375	3.072	10.056	2.632	5.435	0.776
r^{2}SCAN	3.561	4.331	3.076	10.071	2.611	5.440	0.782
HSE06	3.546	5.343	3.070	10.048	3.172	5.433	1.153
Ekspt.	3.555[a]	5.48[b]	3.080[c]	10.082[c]	3.265[d]	5.419[e]	1.170[f]

[a] [107] [b] [109] [c] [111] [d] [112] [e] [113] [f] [114]

2 lentelė: Deimanto LO fononų energija (meV) pirmos Brillouin zonos taškuose. Eksperimentiniai duomenys iš [118].

	Γ	X	L
PBE	160.7	148.1	154.6
SCAN	167.0	153.2	160.4
rSCAN	165.0	152.5	159.6
r^{2}SCAN	164.7	152.0	159.0
HSE06	171.0	154.7	160.8
Ekspt.	164.0	151.3	157.0

rezultatus. Kaip ir kitose medžiagose, su hibridiniu HSE06 funkcionalu gauta E_g vertė yra artimiausia eksperimentinui [114].

Deimanto fononų dispersijos kreivės buvo apskaičiuotos naudojant `PHONOPY` programinį paketą [117]. Lentelėje 2 pateiktos su skirtingais funkcionalais apskaičiuotos išilginių optinių (angl. *longitudinal-optical*, LO) fononų energijos aukštos simetrijos pirmos Brillouin zonos Γ, X ir L taškuose. Šios suskaičiuotos vertės palygintos su eksperimentinėmis netampriosios neutronų sklaidos (angl. *inelastic neutron scattering*, INS) vertėmis [118]. SCAN tipo funkcionalai duoda geriausią atitikimą su eksperimentinėmis vertėmis, ypač r^{2}SCAN funkcionalas (žr. 3.2 pav.). PBE funkcionalas nuvertina, o HSE06 pervertina LO fononų dažnius. Tačiau r^{2}SCAN funkcionalas pateikia vertes, kurios yra tarp PBE ir HSE06 rezultatų ir geriausiai sutampa su eksperimentiniais rezultatais [118].

Apibendrinant, SCAN ir r^{2}SCAN funkcionalai tiksliausiai atkuria gardelės konstantas ir fononų dažnius, o taip pat pagerina draustinio juostos tarpo vertes, palyginti su PBE funkcionalu. Vis dėlto, hibridinis HSE06 funkcionalas išlieka tiksliausias prognozuojant draustinį juostos tarpą.

2.3. Defektų elektroninių sužadinimų skaičiavimai

Optiniai sužadinimai spalviniuose centruose yra glaudžiai susiję su defektų elektronine struktūra. Trečiame skyriuje aptariami spalvinių centrų deimante ir neutralių divakansijų defektų 4H silicio karbide skaičiavimų rezultatai, lyginant teorines befononės linijos (angl. *zero-phonon line*, ZPL) energijas su eksperimentiniais duomenimis.

3 lentelėje pateikiamos NV^-, SiV^-, GeV^- ir SnV^- spalvinių centrų deimante apskaičiuotos ir eksperimentinės befononės linijos energijos, gautos naudojant skirtingus funkcionalus. SCAN funkcionalu apskaičiuotos ZPL energijos yra artimos eksperimentinėms vertėms, su 0.070 eV vidutine absoliučiąja paklaida (angl. *mean absolute error*, MAE). Ši paklaida yra beveik identiška hibridinio HSE06 funkcionalo rezultatui (MAE = 0.068 eV). Nors tiek SCAN, tiek PBE funkcionalai sistemingai nuvertina draustinį juostos tarpą, su SCAN funkcionalu gautos ZPL energijos yra ženkliai tikslesnės ir beveik prilygsta keliasdešimt kartų daugiau skaičiavimo išteklių reikalaujančiam HSE06 funkcionalui.

4 lentelėje pateikiamos skirtingų 4H-SiC neutralių divakancijų konfigūracijų (*hh*, *kk*, *hk* ir *kh*) suskaičiuotos ir eksperimentinės befononės linijos energijos. SCAN funkcionalas pasižymi geriausiu tikslumu, su 0.021 eV vidutine absoliučiąja paklaida, o r^{2}SCAN duoda šiek tiek didesnę paklaidą (0.035 eV). Lyginant su anksčiau publikuotais rezultatais, SCAN funkcionalu gautos vertės yra artimesnės eksperimentiniams duomenims nei PBE ar net hibridinių funkcionalų (HSE06 ir DDH) rezultatai.

Šie rezultatai rodo, kad SCAN ir r^{2}SCAN funkcionalai gali tiksliai ir skaitmeniškai efektyviai prognozuoti spalvinių centrų optines savybes puslaidininkiuose, sudarydamas pagrindą tolimesniems teoriniams tyrimams.

2.4. Elektron–fononinės sąveikos modeliavimas

Šios disertacijos ketvirtame skyriuje nagrinėjama elektronų ir fononų sąveikos įtaka giliųjų defektų optinėms linijoms, taikant tankio funkcionalo teorijos skaičiavimus. Tirti defektai buvo neigiamai įkrautas NV^- centras deimante, neutralios divakansijos 4H silicio karbide ir C-centras silicyje. Darbo tikslas buvo įvertinti SCAN, rSCAN ir r^{2}SCAN funkcionalų tikslumą modeliuojant elektron–fononinę sąveiką ir optines linijas,

3 lentelė: Suskaičiuotos ir eksperimentinės spalvinių centrų deimante befononės linijos energijos vertės (eV). MAE yra vidutinė absoliučioji paklaida (eV) kiekvienam funkctionalui.

	NV^-	SiV^-	GeV^-	SnV^-	MAE
PBE	1.692	1.486	1.855	1.845	0.203
SCAN	1.867	1.567	2.001	1.974	0.070
rSCAN	1.812	1.543	1.948	1.932	0.114
r^2SCAN	1.806	1.533	1.943	1.929	0.120
HSE06	2.002	1.717	2.139	2.105	0.068
Ekspt.	1.945[a]	1.682[b]	2.059[c]	2.003[d]	

[a] [13] [b] [133] [c] [134] [d] [135]

4 lentelė: Suskaičiuotos ir eksperimentinės neutralių divakansijos defektų 4H silicio karbide befononės linijos energijos vertės (eV). MAE yra vidutinė absoliučioji paklaida (eV) kiekvienam funkctionalui.

		hh	*kk*	*hk*	*kh*	MAE
Šis darbas	SCAN	1.129	1.123	1.141	1.103	0.021
	r^2SCAN	1.079	1.081	1.100	1.062	0.035
Kiti darbai	PBE	0.925[a]	0.945[a]	0.975[a]	0.95[a]	0.170
		0.9375[b]	0.951[b]	0.979[b]	–	0.158
	HSE06	1.056[a]	1.044[a]	1.103[a]	1.081[a]	0.044
		1.221[b]	1.218[b]	1.269[b]	–	0.122
		1.13[c]	1.14[c]	1.21[c]	1.24[c]	0.065
	DDH	1.196[b]	1.201[b]	1.259[b]	–	0.105
	Ekspt.[d]	1.095	1.096	1.150	1.119	

[a] [98] [b] [102] [c] [136] [d] [137]

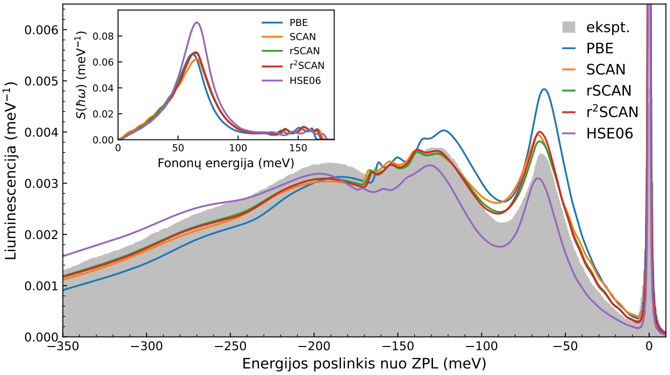

1 pav.: Deimanto NV$^-$ centro teorinės normalizuotos liuminescencijos linijos suskaičiuotos naudojant skirtingus funkcionalus ir palygintos su eksperimentiniu spektru [147]. Intarpe pavaizduota spektrinė elektron–fononinės sąveikos funkcija kiekvienam funkcionalui.

lyginant jas su PBE, HSE06 funkcionalais bei eksperimentiniais duomenimis.

Vienas pagrindinių šio darbo rezultatų yra elektron–fononinės sąveikos modeliavimas NV$^-$ centre deimante. Skaičiavimai parodė, kad liuminescencijos linijos, suskaičiuotos naudojant SCAN, rSCAN, r^{2}SCAN geriau sutampa su eksperimentiniu liuminescencijos spektru, nei su PBE ar HSE06 funkcionalais. Kaip matyti iš 1 pav., fononų pajuostės forma geriausiai sutampa su eksperimentu naudojant SCAN šeimos funkcionalus. Šie rezultatai rodo, kad SCAN tipo funkcionalai sugeba tiksliai modeliuoti elektron–fononinę sąveiką, su daug didesniu skaitmeniniu efektyvumu lyginant su hibridiniais funkcionalais.

Neutralios divakansijos 4H-SiC kristale buvo tirtos naudojant r^{2}SCAN funkcionalą. 2 pav. parodytos teorinės normalizuotos liuminescencijos linijos, kurios sėkmingai sutampa su eksperimentiniais spektrais [102, 155]. Skaičiavimai atskleidė, kad skirtingos neutralių divakansijų konfigūracijos (*hh*, *kk*, *hk*, *kh*) pasižymi nevienodu elektron–fononinės sąveikos stiprumu. *kh* divakansija turi mažiausią elektron–fononinės sąveikos stiprumą ir didžiausią Debye–Waller faktorių (kuris nusako befononės linijos santykį su visos liuminescencijos linijos intensyvumu).

Galiausiai, su SCAN funkcionalu apskaičiuotos C-centro silicyje optinės linijos puikiai sutampa su eksperimentiniais duomenimis (žr. 3 pav.). Skaičiavimai leido tiksliai identifikuoti pagrindines virpesines modas, įskaitant tiek lokalizuotas, tiek rezonansines defekto ir kristalo virpesines modas. Palyginimas su eksperimentiniu spektru rodo, kad SCAN funkcionalas tiksliai atkuria liuminescencijos linijos struktūrą, ir

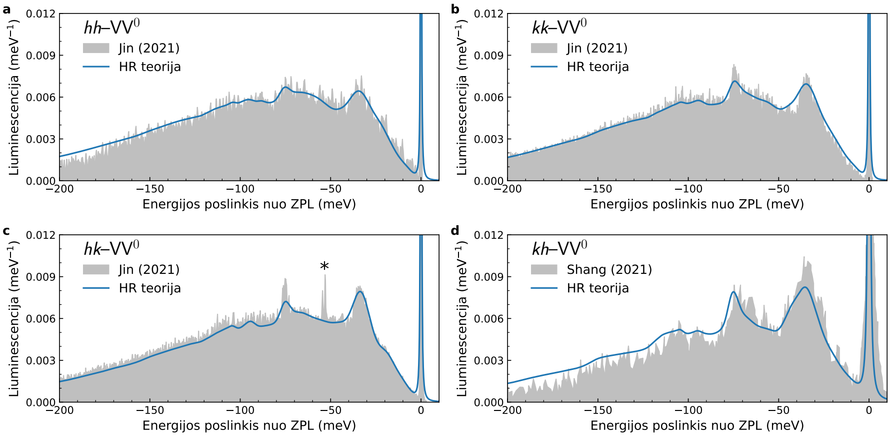

2 pav.: 4H silicio karbido neutralių divakansijų liuminescencijos linijos. Mėlynos linijos yra su HR teorija suskaičiuotos normalizuotos liuminescencijos naudojant r^{2}SCAN funkcionalą. Pilka spalva yra pažymėti eksperimentiniai spektrai iš [102, 155].

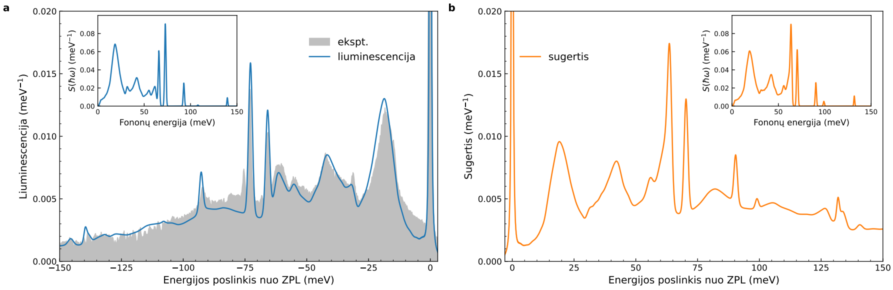

3 pav.: Silicio C-centro teorinės normalizuotos **a** liuminescencijos ir **b** sugerties linijos suskaičiuotos naudojant SCAN funkcionalą. Intarpe pavaizduota spektrinė elektron–fononinės sąveikos funkcija. Eksperimentinis spektras iš [156].

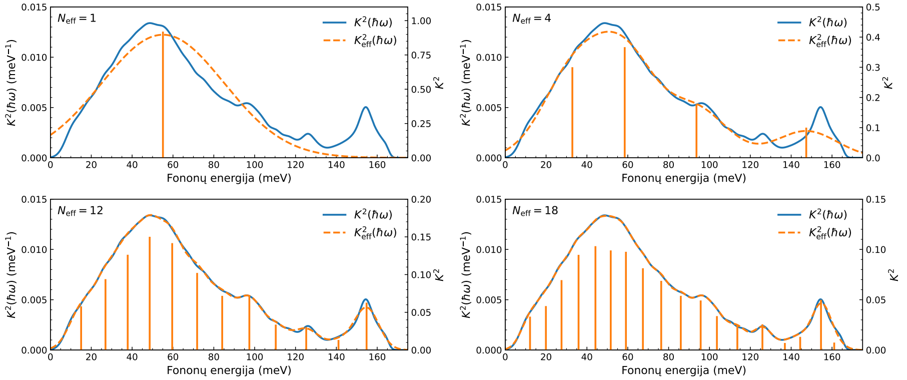

4 pav.: Efektyvios tiesinės JT sąveikos spektrinės funkcijos $K^2_{\mathrm{eff}}(\hbar\omega)$ konvergencija į $K^2(\hbar\omega)$ didėjant efektyvių modų skaičiui N_{eff} NiV$^-$ centrui deimante liuminescencijos metu. Oranžiniai stulpeliai atvaizduoja efektyvias modas su atitinkamais dažniais ir sąveikos vertėmis K^2_n.

sustiprina šio defekto priskyrimą kaip šios optinės linijos šaltinį.

Apibendrinant, šiame darbe atliktas sisteminis elektron–fononinės sąveikos modeliavimas šešiuose skirtinguose defektuose. Pritaikant modernius SCAN šeimos funkcionalus, pavyko pasiekti geresnį sutapimą su eksperimentiniais duomenimis, nei naudojant įprastus PBE ir HSE06 funkcionalus.

2.5. Jahn–Teller efekto tyrimas

Penktame skyriuje buvo atliktas *ab initio* optinių linijų modeliavimas, atsižvelgiant į dinaminį Jahn–Teller (DJT) efektą. Pagrindinė NiV$^-$ centro deimante būsena ir 4H-SiC *hh* ir *kk* divakansijų sužadintos optinės būsenos yra elektroniškai dvigubai išsigimusios. Būtent šis išsigimimas nulemia dinaminį Jahn–Teller efektą, kur reikia ištirti vibroninę struktūrą, kur neįmanoma adiabatiškai atskirti elektroninių ir virpesinių laisvės laipsnių.

Šiame skyriuje buvo pritaikyta daugelio efektyvių modų Jahn–Teller sistemų analizės metodologija [34, 75]. 4 pav. iliustruoja efektyvios tiesinės JT sąveikos spektrinės funkcijos $K^2_{\mathrm{eff}}(\hbar\omega)$ konvergenciją į JT sąveikos spektrinę funkciją $K^2(\hbar\omega)$ didėjant efektyvių modų skaičiui N_{eff}. Čia oranžiniai stulpeliai atvaizduoja parinktas efektyvias modas su atitinkamais dažniais ir sąveikos stiprumo vertėmis K^2_n. Didinant N_{eff}, $K^2_{\mathrm{eff}}(\hbar\omega)$ vis tiksliau atitinka visų fononų modų įnašą į JT sąveiką. Tai parodo, kad jau santykinai mažas N_{eff} modų skaičius leidžia tinkamai atkurti vibroninę sąveiką, o tai ženkliai sumažina reikalingų skaičiavimų sudėtingumą.

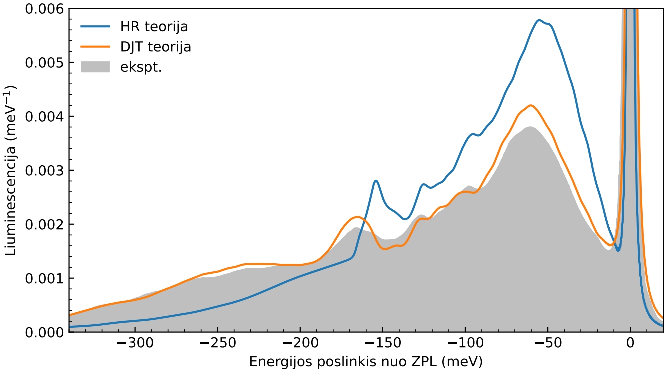

5 pav.: Deimanto NiV^{-} centro teorinės normalizuotos liuminescencijos linijos suskaičiuotos naudojant HR teoriją (mėlyna linija) ir DJT teoriją (oranžinė linija). Linijos suskaičiuotos naudojant r^2SCAN funkcionalą. Eksperimetinis spektras iš [131].

5 pav. pavaizduota su HR ir DJT teorijomis suskaičiuotos normalizuotos liuminescencijos linijos. Naudojant r^2SCAN funkcionalą ir naujovišką daugelio modų Jahn–Teller sistemų skaičiavimo metodologiją, buvo tiksliai sumodeliuotas NiV^{-} centro deimante liuminescencijos spektras ir nustatytos optinės savybės, kurios ateina būtent dėl Jahn–Teller sąveikų, taip įrodant šio funkcionalo efektyvumą modeliuoti vibronines sąveikas.

Analogiškas optinių linijų modeliavimas buvo atliktas neutralioms 4H-SiC *hh* ir *kk* divakansijoms. Šių sistemų optinės sugerties linijos, apskaičiuotos naudojant DJT teoriją, buvo palygintos su HR teorija (žr. 5.12 pav.).

CURRICULUM VITAE

Name: Vytautas

Surname: Žalandauskas

Place of birth: Šiauliai, Lithuania

E-mail: vytautas.zalandauskas@ftmc.lt

Education:

2020 – 2025	Center for Physical Sciences and Technology *PhD studies*
2018 – 2020	Vilnius University, Faculty of Physics *Master's degree in Technological Sciences*
2014 – 2018	Vilnius University, Faculty of Physics *Bachelor's degree in Physics. Cum Laude*
2010 – 2014	Kuršėnai Laurynas Ivinskis Gymnasium

Work experience:

2023 – 2025	Center for Physical Sciences and Technology Department of Fundamental Research *Junior research fellow*
2018 – 2022	Center for Physical Sciences and Technology Department of Fundamental Research *Engineer*
2016 – 2018	Center for Physical Sciences and Technology Department of Fundamental Research *Technician*

NOTES

NOTES

NOTES

Vilnius University Press
9 Saulėtekio Ave., Building III, LT-10222 Vilnius
e-mail: info@leidykla.vu.lt, www.leidykla.vu.lt
bookshop.vu.lt, journals.vu.lt
Print run copies 15